

**Probing Non-collinear Spin Textures using Variable
Temperature Magnetic Force Microscopy**

Dissertation

zur Erlangung des
Doktorgrades der Naturwissenschaften
(Dr. rer. nat.)

der Naturwissenschaftlichen Fakultät II
Chemie, Physik und Mathematik

der Martin-Luther-Universität
Halle-Wittenberg

vorgelegt von Herrn

Ankit Kumar Sharma

Geboren am 28.02.1991 in Sawai Madhopur, India

Gutachter:

Prof. Dr. Stuart S. P. Parkin

Prof. Dr. Ingrid Mertig

Prof. Dr. Hans J. Hug

Tag der öffentlichen Verteidigung:

24.01.2022

Dedicated to My Parents

Kaushalya Devi and Chheetar Lal Sharma

Abstract

The emergence of magnetic skyrmions, which are topological spin textures, has aroused tremendous research interest from both a fundamental physics perspective as well as from their potential application in next-generation energy-efficient and high-density spintronic devices.

In this thesis, various kinds of non-collinear spin textures are investigated in bulk crystals and thin films of three non-centrosymmetric compounds. Variable temperature magnetic force microscopy is the main research tool that was used to probe these novel spin textures.

First, the properties of antiskyrmions are studied in single-crystalline lamellae of the inverse tetragonal Heusler compound $\text{Mn}_{1.4}\text{PtSn}$ that has a crystal structure with D_{2d} crystalline symmetry. This compound is a ferrimagnet with an ordering temperature of ~ 400 K. However, as the temperature and applied magnetic field is varied the ground state can evolve from a single domain state with a uniform magnetization to a complex magnetic texture. Typically, as the magnetic field is increased along the easy magnetic axis of the compound, the magnetic state evolves first into a helical magnetic state in which the magnetization varies spatially in a sinusoidal manner along with two orthogonal crystal axes ($[100]$ and $[010]$), and secondly into a hexagonal array of antiskyrmions. The antiskyrmion is typically a round nano-object in which the magnetization outside rotates to the opposite direction spatially along the radius. Depending on the crystal direction the magnetization rotates along the radius to form a Neel wall-like boundary or perpendicular to the radius (along the tangent) to form a Bloch-like wall.

Abstract

A major discovery of my work was the extreme tunability of the size of the antiskyrmion and the period of the helical state as the thickness of the lamella in which the spin textures are observed is increased. This thickness dependence tunability is attributed to the significant influence of magnetic dipolar interactions as compared to the thickness-independent Dzyaloshinskii-Moriya interaction.

Secondly, spin textures are explored in epitaxially grown thin films of another Heusler compound, Mn_2RhSn , that also has D_{2d} symmetry. These nano-objects exhibit a wide range of stability with respect to magnetic field and temperature that is similar to single-crystalline lamellae. Elliptically distorted nano-objects along perpendicular crystallographic directions within the epitaxial films are found that is consistent with elliptical Bloch skyrmions observed in single-crystalline lamellae of Mn_2RhSn . A small increase in the size of nano-objects is observed with increasing film thickness, which is a much smaller variation than the D_{2d} bulk $\text{Mn}_{1.4}\text{PtSn}$ crystal due to the comparatively lower magnetization of Mn_2RhSn . The creation and annihilation of nano-objects using a local magnetic field from a magnetic tip are shown in these thin films.

Thirdly, Néel skyrmions were discovered in the single crystalline lamella of the compound PtMnGa which we showed has a non-centrosymmetric crystal structure: prior to this work, this compound was believed to have a centrosymmetric structure for more than 30 years. The thickness dependence of the size of the Neel skyrmion size is studied. A significant dependence of size on thickness is found: this is only the second materials system in which such a phenomenon has been found. Moreover, this compound is the first metallic system in which Néel skyrmions have ever been observed. Prior work showed the existence of Néel skyrmions in two insulating compounds but only at very low temperatures: here we observe Néel skyrmions at temperatures as high as 220 K.

Contents

Abstract	v
Contents	vii
1. Introduction	1
2. Scientific background	9
2.1 Non-collinear spin textures	9
2.2 Magnetic skyrmions and antiskyrmions.....	13
2.3 Magnetic interactions	15
2.3.1 DMI interaction.....	15
2.3.2 Magnetic dipolar interaction	18
2.4 Detection of skyrmions	18
2.4.1 Magnetic imaging techniques	18
2.4.2 Electrical detection.....	19
2.5 Experimental realization of skyrmions	21
2.5.1 Experimental observation of Bloch skyrmions.....	21
2.5.2 Experimental observation of Néel skyrmions.....	24
2.5.3 Experimental observation of antiskyrmions.....	25
3. Experimental methods	27
3.1 Magnetic force microscopy (MFM).....	27
3.1.1 Introduction to magnetic force microscopy	27

3.1.2	General principle.....	28
3.1.3	MFM experimental technique.....	31
3.2	Sample preparation	34
3.2.1	Bulk crystal preparation.....	34
3.2.2	Focused ion beam milling (FIB).....	35
3.2.3	Thin film preparation	38
3.3	Additional measurement techniques	39
3.3.1	Lorentz transmission electron microscopy (LTEM).....	39
3.3.2	X-ray diffraction (XRD)	39
3.3.3	Magnetometer quantum interference device (SQUID).....	41
4.	Tunable magnetic antiskyrmion size and helical period from nanometers to microns in a D_{2d} Heusler compound	43
5.	Nanoscale non-collinear spin textures in thin films of a D_{2d} Heusler compound....	73
6.	Observation of Néel skyrmions in metallic PtMnGa	97
7.	Conclusion and outlook	123
7.1	Conclusion	123
7.2	Outlook	125
	List of publications.....	127
	References.....	133
	List of figures.....	141
	Abbreviations	143
	Acknowledgments	145
	Curriculum Vitae	147

1. Introduction

In today's world of information technology, the amount of data is growing faster than ever. Due to increasing volumes of digital data, the demand for increasing data storage capacity has been rapidly enhanced. Conventional magnetic memory devices, such as magnetic hard disk drives (HDD) [1], have been the primary repository of digital data for more than a decade. Spintronics has played an important role in the development of data storage technology. The discovery of Co/Cu and related multilayers that show giant magnetoresistance (GMR) at room temperature [2], the discovery of oscillations in the magnitude of GMR with increasing thickness of the Cu spacer layer in Co/Ru and Fe/Cr [3], and the discovery of the interfacial origin of GMR [4] led to the invention of the spin-valve by Parkin as a highly sensitive detector of tiny magnetic fields at room temperature. This invention, commercialized by IBM in 1997 [5], has dramatically increased the storage capacity of hard disk drives. Since then, the field of data storage has evolved and several spintronic-based memory storage devices such as magnetic random-access memory (MRAM) based on magnetic tunnel junctions (MTJ) [6-8] have been proposed. These discoveries changed the landscape of magnetic data storage by shrinking the magnetic bit size by many orders of magnitude. However, this technology is gradually reaching its limits over the past years where the bit size cannot be further reduced due to its instability against thermal fluctuations, also known as superparamagnetic limit [9]. Also, at the same time, HDD being a mechanical device leads to large energy consumption and thus limits the writing/reading speed. Therefore, an alternative technique towards achieving energy-efficient and high data density is required.

A promising proposal for a follow-up memory-storage technique is the Racetrack Memory (RM), which was first proposed by Parkin *et.al.* [10, 11]. Racetrack memory is innately a three-dimensional device, in contrast to the two-dimensional structure of conventional HDDs, and based on the controllable motion of magnetic domain walls in magnetic nanowires by the spin-polarized current. This memory does not contain mechanically moving parts, thereby allowing racetrack nano-wires to be stacked in three dimensions. In this way, multiple domain walls can be stored in these racetrack nano-wires which would drastically increase the storage capacity by many orders of magnitude compared to conventional two-dimensional HDDs and solid-state drives. A schematic of racetrack memory is shown in Fig. 1.1a.

To achieve the ultra-high density of information storage, the concept of racetrack memory could be further extended by replacing the domain walls with nano-scale magnetic objects, known as magnetic skyrmions [12, 13]. A magnetic skyrmion is a topological object with a non-collinear chiral spin structure, which was first discovered in a non-centrosymmetric B20 bulk material, a so-called chiral magnet, MnSi [14]. Skyrmions are seen as potential carriers of information owing to their small size down to a few nanometers, topological protection from their annihilation, and ability to manipulate them with smaller current density than domain walls in racetracks [15, 16]. A schematic of skyrmion-based racetrack memory is shown in Fig. 1.1b.

Although magnetic skyrmion-based racetrack memory has the advantage of a reduced critical current density for their motion, and therefore a corresponding reduced power consumption as compared with domain-wall based racetrack memory [12, 13], the skyrmions, do not move parallel to the applied current but rather towards the edge of the racetrack. This phenomenon leads to an angle between the direction of the current flow and

the skyrmion motion, known as the skyrmion Hall effect (SHE) [17, 18]. This skyrmion dynamical motion puts a limitation on their utilization in racetrack devices. Therefore, it is desired to replace magnetic skyrmions with alternative spin textures which possess similar stability and suppress THE to accelerate the current-driven motion of non-collinear spin textures in racetrack memory.

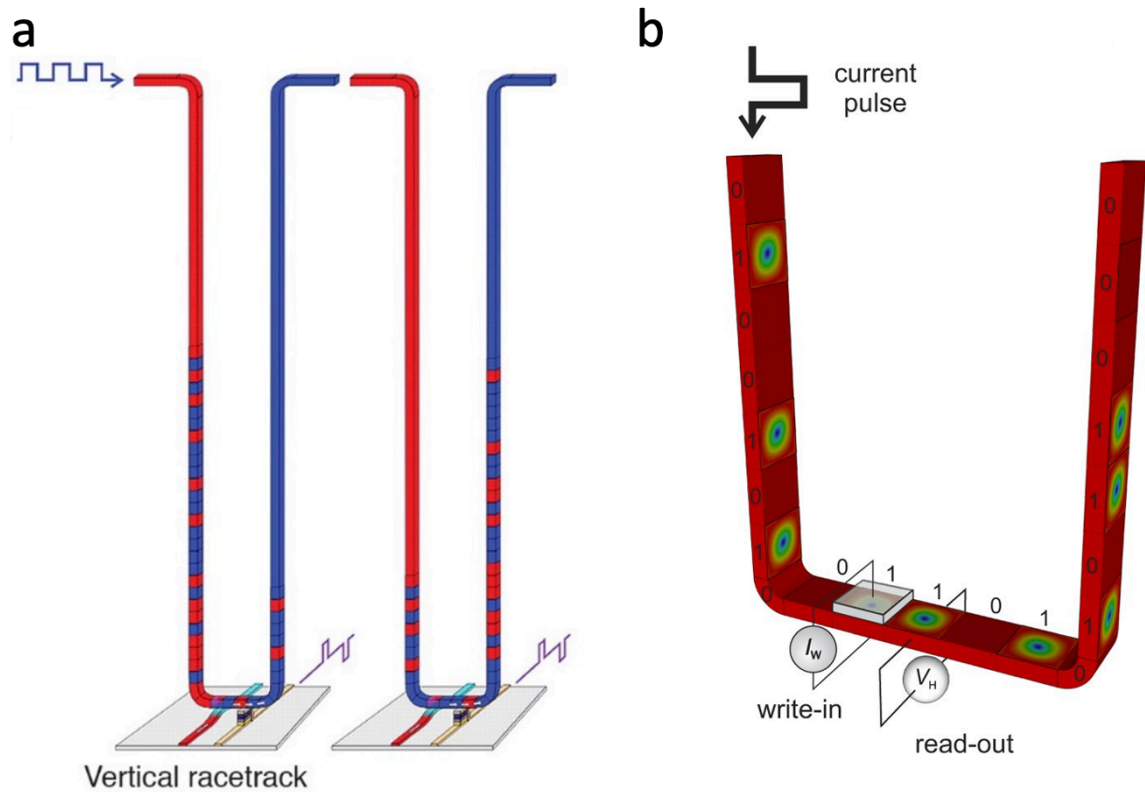


Fig. 1.1: Magnetic domain-wall and skyrmion racetrack memory (a) Racetrack memory designed in the form of vertical U-shaped magnetic nanowires normal to the plane of the substrate. Data reading is realized by sensing the tunnel magnetoresistance of an MTJ element and writing is carried out by the fringing fields produced in an adjacent nanowire from the motion of a domain wall. (From [10]. Reprinted with permission from AAAS). (b) A schematic of skyrmion-based racetrack memory. Current pulses are applied to move skyrmions in the racetrack nano-wire. The magnetic bits are encoded by the presence and absence of magnetic skyrmions corresponding to ‘1’ and ‘0’ bits, respectively. The writing is achieved by the local creation or deletion of a skyrmion by electrical means, while reading is performed by measuring the topological Hall effect.

(Reprinted from [19]. Link to the Creative Commons license: <https://creativecommons.org/licenses/by/4.0/>)

A promising proposal could be to use another class of skyrmion, referred to as an antiskyrmion, in racetrack devices. Antiskyrmions are non-collinear spin textures that were first discovered in the tetragonal Heusler compound $\text{Mn}_{1.4}\text{Pt}_{0.9}\text{Pd}_{0.1}\text{Sn}$ with D_{2d} crystal symmetry [20]. The advantage of antiskyrmions is that their size can be tuned significantly from the nanometer to the micrometer range [21] and that they can be stabilized over a wide range of magnetic fields and temperatures (even at elevated temperatures). In addition, they are predicted to move in straight paths when the current is applied along with specific directions relative to the internal anisotropic spin structure of the antiskyrmion [22]. To date, all of the observations of antiskyrmions in D_{2d} systems have been made in single crystals or thin lamella cut from bulk crystals. Thus, from the application perspective, their observation in thin films is desired. It is, however, challenging to make thin films of tetragonal Heusler compounds.

This thesis aims to explore the exotic properties of various non-collinear spin textures in bulk crystals and thin films of magnetic systems with non-centrosymmetric crystal structures. The Mn_2 -based Heusler family with the D_{2d} symmetry offers a wide range of tunability of magnetic properties and hosts antiskyrmions in co-existence with elliptical Bloch skyrmions [23-25]. The recent probe of the static and dynamic properties of these nano-scale complex spin textures has been possible due to recent developments in microscopy-based techniques. Of these, we have used magnetic force microscopy (MFM) to study magnetic antiskyrmions and skyrmions in thin films and single crystals of Heusler compounds. Three different non-centrosymmetric systems comprising thin films and single-crystalline lamella were investigated to explore spin textures using MFM. The focus here lies on the observation of antiskyrmions and skyrmions in single crystals and exploring the

thickness-dependent behaviors of their size and associated helical period. These magnetic structures are further investigated in thin films considering their compatibility with technological developments of spintronics devices.

Structure of the thesis

In chapter 2, a brief overview of non-collinear magnetism is given. The basic concept of the magnetic antiskyrmion and skyrmion is given. Different kinds of skyrmions and their formation mechanisms are described. Later in the chapter, detection techniques are discussed. The last section of the chapter describes previous work on magnetic skyrmions that have been observed in various magnetic systems.

Chapter 3 introduces the various experimental techniques which are used in this thesis. It begins with the introduction of magnetic force microscopy (MFM) which is used for the detection of magnetic antiskyrmions and skyrmions. The MFM technique is the basis of the results presented in this thesis. Then, focused ion beam (FIB) milling is described, which is used to prepare lamellae of varying thicknesses for MFM and LTEM (Lorentz transmission electron microscopy) measurements. Bulk crystals and thin film growth techniques are discussed. The last section describes the techniques used for structural and magnetic characterization of the samples.

In Chapter 4, the size tunability of antiskyrmions is discussed in single-crystal lamellae of $\text{Mn}_{1.4}\text{PtSn}$ with the D_{2d} crystal structure. The wide range tunability of the antiskyrmion size and associated helical period with increasing lamella thickness is shown. This thickness dependence tunability is attributed to the significant influence of magnetic dipolar interactions and Dzyaloshinskii-Moriya interactions coming from the D_{2d} symmetry of the system.

In chapter 5, the observation of magnetic nano-objects in thin films of a D_{2d} Heusler compound is discussed. Magnetic nano-objects in epitaxial thin films of Mn_2RhSn are investigated. These nano-objects exhibit a wide range of sizes with stability with respect to magnetic field and temperature that is similar to single-crystalline lamellae. Elliptically distorted nano-objects along perpendicular crystallographic directions within the epitaxial films are found that is consistent with elliptical Bloch skyrmions observed in single-crystalline lamellae of Mn_2RhSn . The manipulation of nano-objects using a local magnetic field from a magnetic tip is also shown in the thin films.

In chapter 6, observation of Neel skyrmions in single-crystalline lamellae of $PtMnGa$ which has a non-centrosymmetric crystal structure is discussed. The thickness dependence of the size of Neel skyrmions is studied. It is also shown that they are highly robust against large in-plane fields up to 1T. Finally, Chapter 7 gives a summary of the findings in this thesis and an outlook of possible future work.

1. Introduction

The outline of the experimental results presented in this thesis (chapters 4, 5, and 6) is summarized in Fig. 1.2.

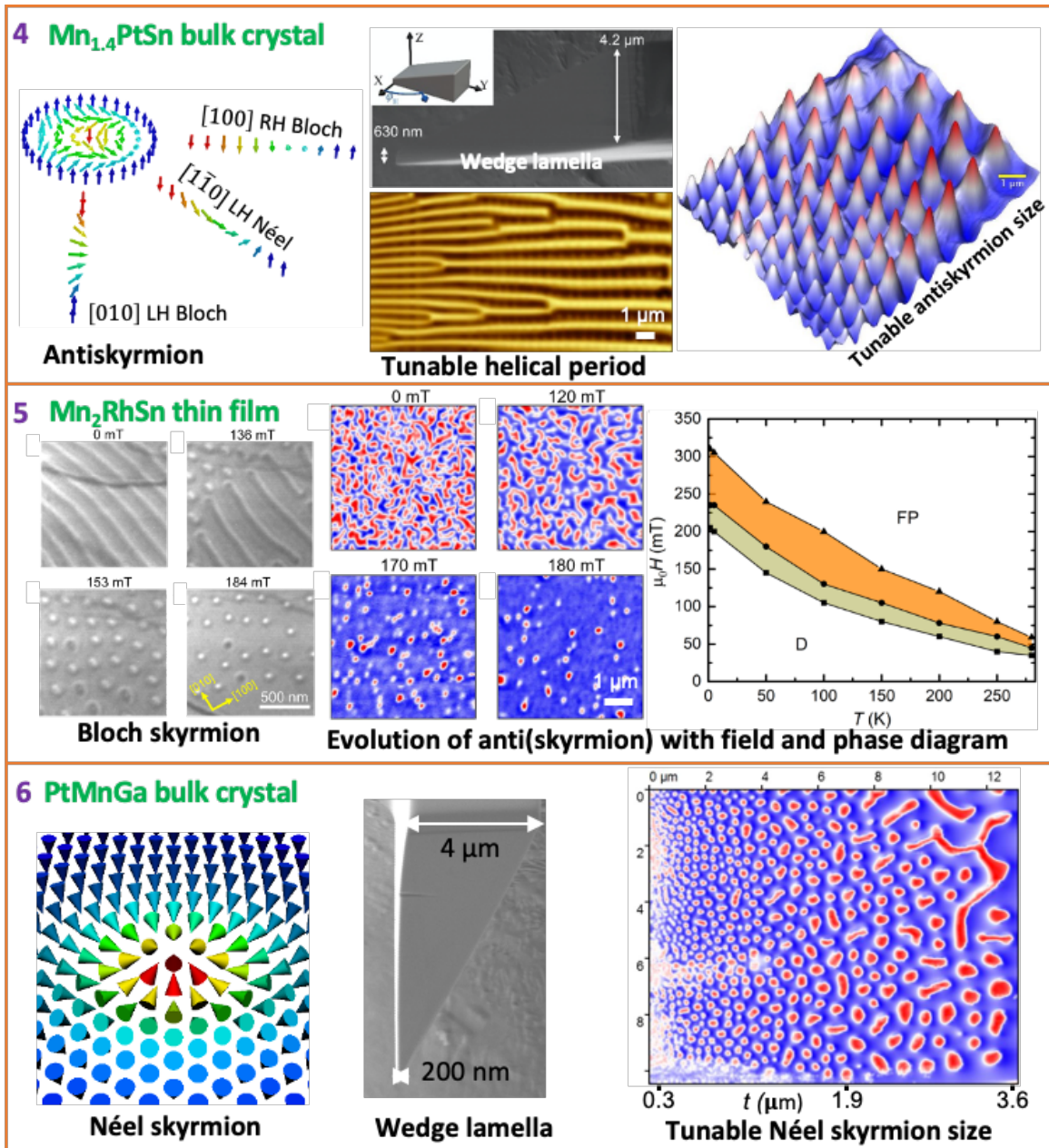


Fig. 1.2: Outline figure of the experimental results. (Reprinted from [21, 26, 27]. Link to the Creative Commons license: <https://creativecommons.org/licenses/by/4.0/>)

2. Scientific background

This chapter gives a scientific background of non-collinear spin textures. Different kind of skyrmions and their formation mechanism are described. Later in the chapter, their detection techniques are discussed. The last section of the chapter describes a background of magnetic skyrmion observed in various magnetic systems.

2.1 Non-collinear spin textures

In the past, tremendous progress has been made in the physics of magnetism at the nanoscale leading to numerous discoveries of magnetic structures. A variety of long- and short-range interactions in the magnetic solid lead to a variety of magnetic structures with all possible spin arrangements from simple collinear (parallel or antiparallel) to complex non-collinear spin textures.

In magnetic materials with inversion symmetry, the Heisenberg exchange interaction ensures the collinear alignment of neighboring spins. This interaction decreases as a function of the distance between two atoms and thus has short-range nature. The isotropic Heisenberg interaction energy can be expressed as:

$$E_H = -\sum_{ij} J_{ij} S_i \cdot S_j \quad (2.1)$$

Where J_{ij} is the exchange integral between sites i and j , and S_i and S_j are two spins at sites i and j . The exchange interaction favors parallel spins, i.e., referred to as ferromagnet for $J_{ij} > 0$, or antiparallel spins, known as anti-ferromagnet for $J_{ij} < 0$. Fig. 2.1a-b shows the spin configurations of ferromagnet and anti-ferromagnet.

When inversion symmetry is broken in low-symmetry magnetic crystals, an antisymmetric and anisotropic exchange interaction, known as Dzyaloshinskii-Moriya interaction (DMI), arises due to strong spin-orbit coupling which links the neighboring spins via a vector product. The DMI energy can be expressed as:

$$E_{\text{DMI}} = -\sum_{ij} D_{ij} \cdot (S_i \times S_j) \quad (2.2)$$

Where D_{ij} is the Dzyaloshinskii vector. The DMI favors the adjacent spins to align perpendicularly to each other thereby leading to the formation of spin spiral structures.

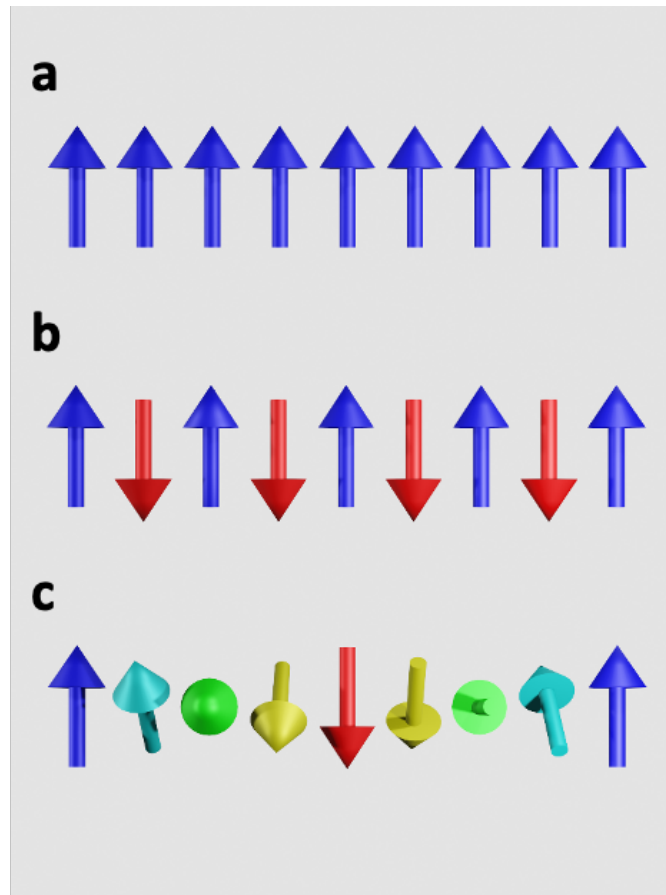


Fig. 2.1: Heisenberg interaction that favors (a) parallel (ferromagnet) or (b) antiparallel spins (antiferromagnet) depending on the sign of J . (c) Combination of Heisenberg interaction and DMI leads to the formation of the spin spiral state with left-hand or right-hand chirality.

The competition between Heisenberg exchange and DMI leads to complex non-collinear spin structures such as the spin spiral state where spin rotates in a unique rotation sense with a small canting between the neighboring spins, as shown in Fig. 2.1c. This rotational sense is determined by the sign of D_{ij} . The direction and magnitude of D_{ij} are governed by the symmetry of the system and the underlying physics mechanism [28, 29].

The simplest demonstration of one-dimensional non-collinear spin texture is a domain wall (DW) [30, 31], where magnetization rotates from one direction to another between two neighboring domains aligned in opposite directions. In ferromagnetic materials, the formation of domain walls is energetically favored to minimize magnetostatic energy. The width (d) of the DW in uniaxial bulk magnets is determined by $d = \pi\sqrt{A/K}$, where A is anisotropy energy and K is exchange energy. DW can be as narrow as a few nanometers in materials having large perpendicular magnetic anisotropy (PMA). The stray field originates from the regions of the domain wall as opposed to domains, in which the spins are aligned in one direction. This stray field can be detected in magnetic force microscopy (MFM), which is discussed later in Chapter 3.

The domain walls can form many configurations depending on the anisotropy and geometry of the sample. In thin films, the DWs can adopt two configurations: *Bloch walls* and *Neel walls*. A Bloch wall is characterized by a rotation of magnetization out of the plane of the DW, whereas for Neel walls, the magnetization rotates within the plane of the DW (as shown in Fig. 2.2). In the absence of DMI, the magnetization rotation within DW has no preferred handedness i.e., DW is achiral. However, when DMI is present, the chiral degeneracy is lifted due to symmetry breaking, and as a consequence DW exhibit a fixed chirality. Such DWs are also known as chiral domain walls. For example, in thin film heterostructures [32-34], interfacial DMI can stabilize DWs of a fixed chirality either left-

handed chiral Neel DW ($\uparrow\leftarrow\downarrow$ or $\downarrow\rightarrow\uparrow$, for $D<0$) or right-handed chiral Neel DW ($\uparrow\rightarrow\downarrow$ or $\downarrow\leftarrow\uparrow$, from $D>0$).

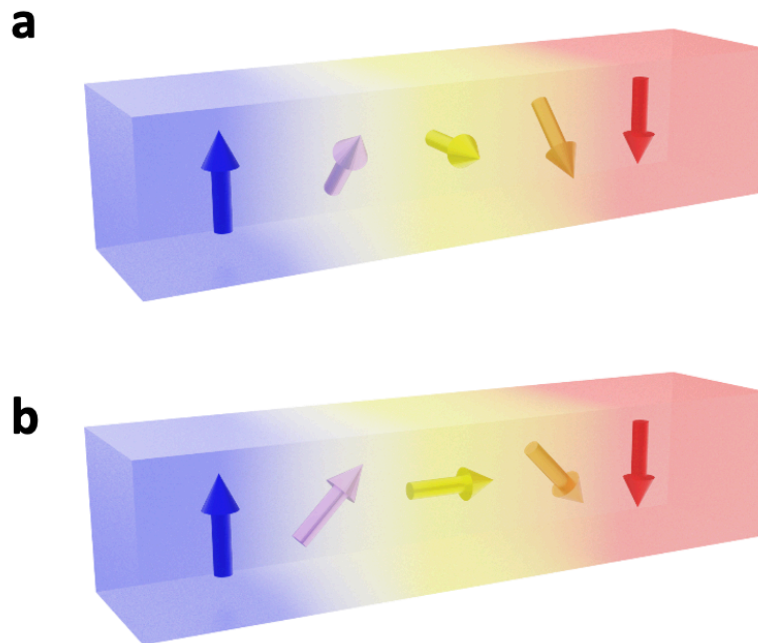


Fig. 2.2: Sketch of domain walls in perpendicularly magnetized film. a) Bloch wall (b) Néel wall. The arrows indicate magnetization directions.

When non-collinearity is extended from one-dimensional DW to two dimensions, the spin texture evolves into a complex chiral structure such as magnetic skyrmions, which will be discussed in the subsequent section. Non-collinear spin textures have become the focus of recent research after the experimental discovery of magnetic skyrmions [14] due to their potential application in future spintronic devices. Since then, the focus has been on exploring different kinds of skyrmions in various magnetic materials. This quest led to the recent discovery of another kind of skyrmions, known as magnetic antiskyrmion [14], in a D_{2d} Heusler compound.

2.2 Magnetic skyrmions and antiskyrmions

The topological nature of magnetic skyrmion is characterized by a non-zero topological charge, also called as skyrmion number, Q defined by the following equation:

$$Q = \frac{1}{4\pi} \iint \mathbf{n}(\mathbf{r}) \cdot \left(\frac{\partial \mathbf{n}(\mathbf{r})}{\partial x} \times \frac{\partial \mathbf{n}(\mathbf{r})}{\partial y} \right) d^3r \quad (2.3)$$

Q represents how many times the magnetization direction \mathbf{n} wraps around a unit sphere. Here $\mathbf{n} = \mathbf{m}/|\mathbf{m}|$ is the unit vector of the local magnetization [14, 35]. The sign of Q (\pm) represents the magnetization at the skyrmion core i.e., $Q = +1$ for up magnetization at the core (skyrmion) and $Q = -1$ for down magnetization at the core (anti-skyrmion). Since skyrmions have an integer topological charge, they are robust and topologically protected against small deformations.

The internal spin structure of magnetic skyrmion is defined by the symmetry of the underlying crystal lattice and the type of DMI. Various forms of skyrmions are formed depending on the crystal lattice symmetry. Based on the rotation of the magnetization within the skyrmion, it can be classified into three types:

1. **Bloch skyrmion:** Stabilized by bulk DMI in compounds with cubic B20 crystal structure and tetrahedral symmetry compounds [14, 36, 37].
2. **Néel skyrmion:** Stabilized by interfacial DMI in Multilayer films [38-42] and compounds with C_{nv} crystal symmetry [26, 43, 44].
3. **Antiskyrmion:** Stabilized by anisotropic DMI in compounds with D_{2d} [20, 21, 23-25, 45, 46] and S_4 crystal symmetry [47].

Fig. 2.3 shows a schematic of the spin configuration of the Bloch skyrmion, Néel skyrmion, and antiskyrmion, where the arrows depict the direction of the spins. Bloch skyrmion is characterized by Bloch domain wall i.e., spins rotate as helical spin spirals in a plane perpendicular to the direction of propagation as one moves from its core to the

periphery (Fig. 2.3a), whereas Néel skyrmion is characterized by Néel domain wall i.e., spins rotate as cycloidal spin spirals in a plane parallel to the direction of propagation as one moves from its core to the periphery (Fig. 2.3b). Antiskyrmion is composed of successive Bloch and Néel domain walls as one traces around the boundary. As shown in Fig. 2.3c, the spin configuration of an antiskyrmion consists of both helical and cycloidal spin.

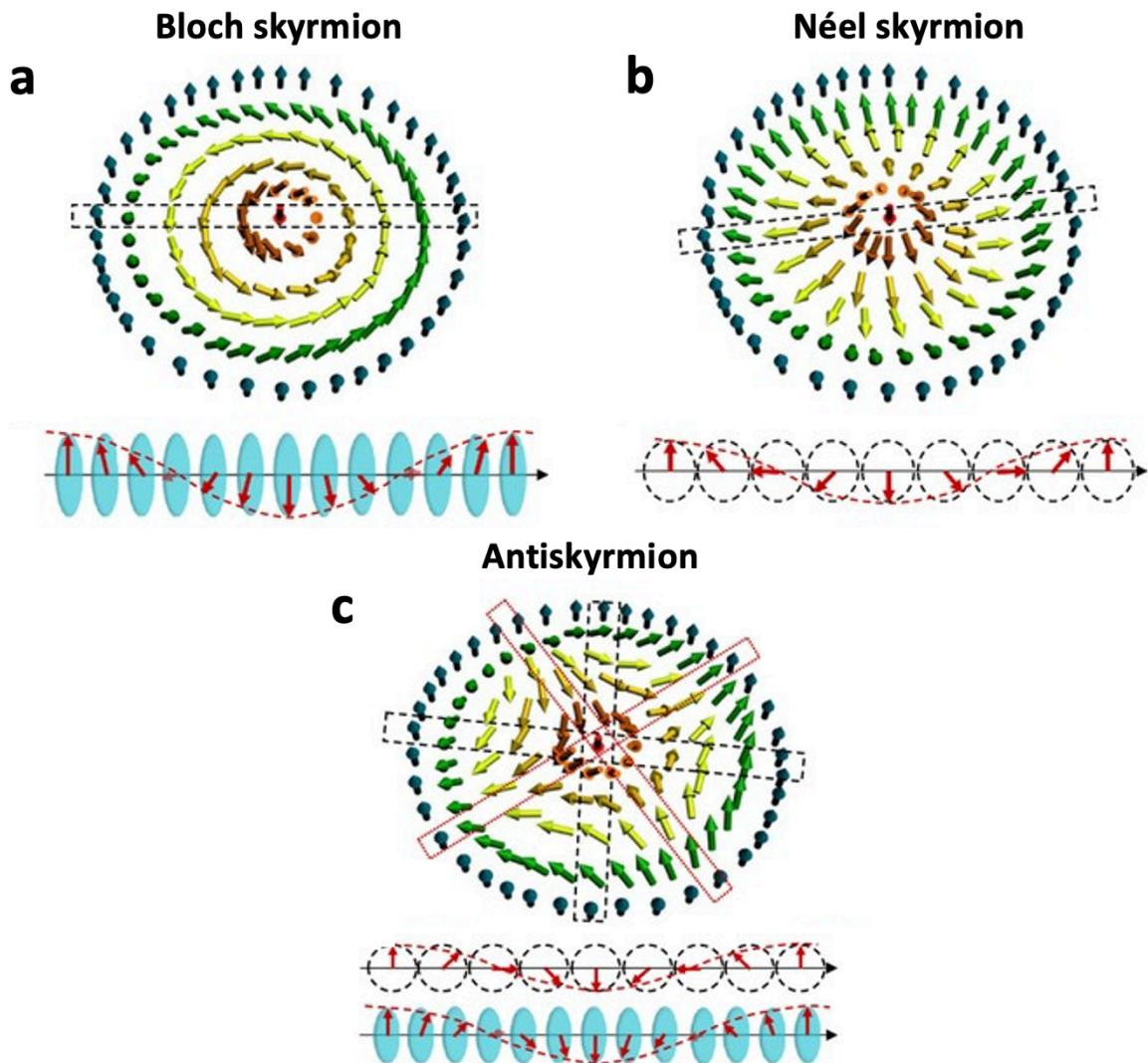


Fig. 2.3: Spin configuration of magnetic skyrmion (a) Bloch (b) Néel and (c) Antiskyrmion. The lower panel in each figure shows a cross-section of skyrmions along the radial directions indicated by the dashed rectangles. For Bloch and Néel skyrmion, the helimagnetic structure is helix and cycloid, respectively. Whereas antiskyrmion shows both helix and cycloid structure. (Reprinted by permission from Springer Nature Customer Service Centre GmbH: Springer Nature, Nature, [20],

(Magnetic antiskyrmions above room temperature in tetragonal Heusler materials, Ajaya K. Nayak *et al.*), COPYRIGHT (2017)).

2.3 Magnetic interactions

The topological properties and dynamics of skyrmions arise from various magnetic interactions competing with each other. The total energy of the skyrmion system is the contribution of the following energy terms:

$$H = E_H + E_{\text{DMI}} + E_{\text{dip}} + E_{\text{an}} + E_Z \quad (2.4)$$

Where E_H is Heisenberg exchange energy, E_{DMI} is DMI exchange energy, E_{dip} dipole coupling energy, E_{an} is anisotropy energy and E_Z is Zeeman energy. Depending on the ratio between these energy terms, a certain kind of magnetic ground state and skyrmion is realized.

There have been several different mechanisms proposed to stabilize skyrmion in magnets. There are: (1) DMI interaction [48-50], (2) Magnetic dipolar interaction [31, 51-53], (3) Four-spin exchange interactions [54], and (4) Frustrated exchange interaction [55]. Out of these, two major mechanisms (1) and (2) are extensively studied, which are discussed below.

2.3.1 DMI interaction

One major mechanism for skyrmion formation is the competition between the ferromagnetic exchange interaction and antisymmetric exchange interaction Dzyaloshinskii-Moriya interaction (DMI) [48-50]. Skyrmions stabilized through DMI have a well-defined skyrmion number Q and fixed chirality.

In ferromagnets with non-centrosymmetric crystal structures such as B20 compounds [14, 36, 37], the bulk DMI which originates from the relativistic spin-orbit coupling (SOC) becomes finite and plays a key role in forming skyrmion [28, 29]. A schematic of bulk DMI is shown in Fig. 2.4a. Skyrmions stabilized by bulk DMI in these bulk materials are classified as Bloch skyrmions. In these magnetic systems, helical spin order is a magnetic ground state realized in the absence of an external field. When the magnetic field is applied, the helical spin structures transform into Bloch skyrmions. The helical wavelength λ or the skyrmion size is determined by the ratio in the form of J/D , where J and D , are the magnitudes of the ferromagnetic exchange interaction and DMI. Typically, this ratio ranges from 1 to 100 nm.

In thin film heterostructures [38-42], interfacial DMI (i -DMI) is one of the most important mechanisms to stabilize Néel skyrmions. In these multilayer films, i -DMI originates at the interface where a thin ferromagnet is coupled to a large SOC material. A schematic of interfacial DMI is shown in Fig. 2.4b.

In compounds with D_{2d} [20] and S_4 [47] symmetry, antiskyrmions are stabilized by anisotropic DMI which comes from the underlying crystal symmetry. Due to the anisotropic nature of DMI, the spin texture of antiskyrmion composes of a chiral boundary of helical and cycloidal propagation, as shown in Fig. 2.3c.

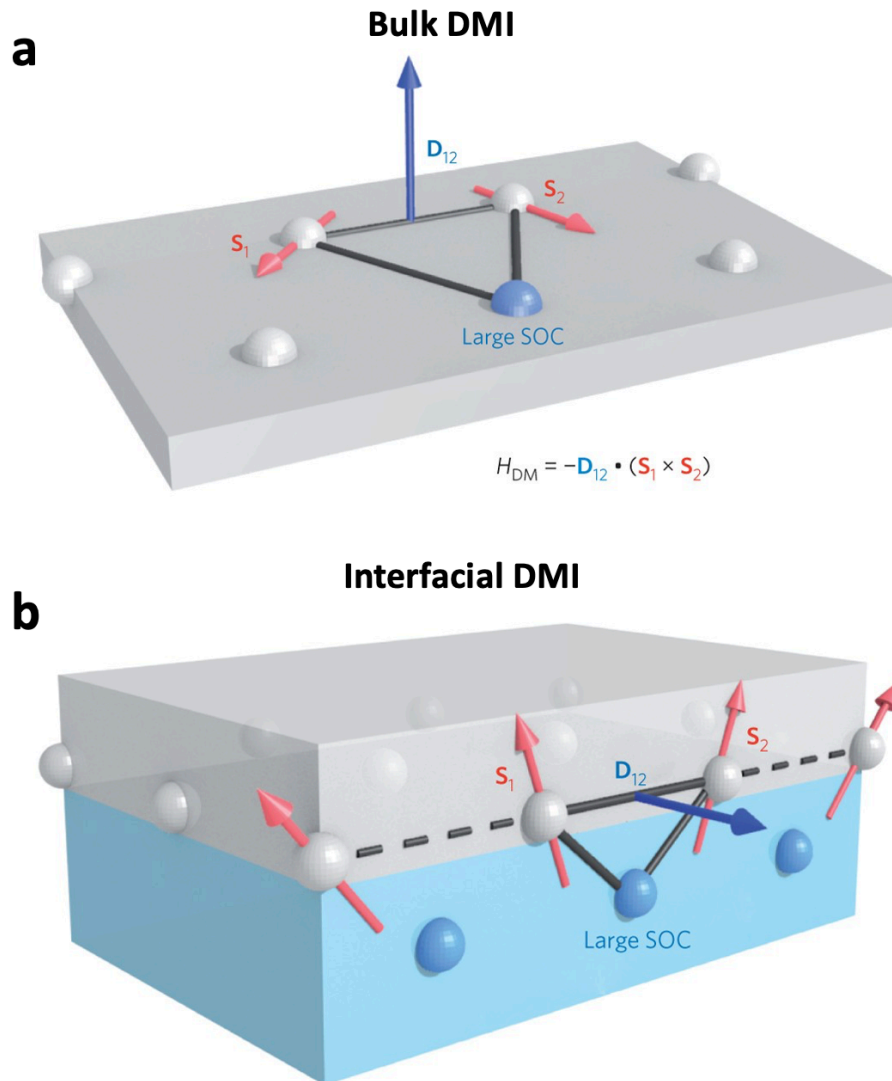


Fig. 2.4: Sketch of DMI. a) Bulk DMI originated from the indirect exchange mechanism between two spins (S_1 and S_2) with a large neighboring atom having large SOC. b) Interfacial DMI at the interface between a ferromagnetic thin film (grey) and a metallic layer (blue) having large SOC. The resulting bulk and interfacial DMI vector points perpendicular to the triangle consist of two magnetic atoms and an atom with large SOC. (Figure a-b, Reprinted by permission from Springer Nature Customer Service Centre GmbH: Springer Nature, Nature Nanotechnology, [12], (Skyrmions on the track, Albert Fert *et al.*), COPYRIGHT (2013))

2.3.2 Magnetic dipolar interaction

Another mechanism to stabilize skyrmion is the interplay between the magnetic dipolar-dipolar interaction and easy-axis anisotropy. A typical example of skyrmions stabilized through this mechanism is centrosymmetric ferrimagnets with PMA [31, 51-53]. Here, due to the centrosymmetric space group, DMI is no longer present. In such systems, only dipolar energy and anisotropy energy are relevant which prefers in-plane magnetization and out-of-plane magnetization, respectively. The competition between these two energy terms leads to the formation of a periodic cylindrical domain structure known as a magnetic bubble or skyrmion bubble [31, 51-53]. Several spin textures associated with skyrmion bubbles have been observed in various centrosymmetric compounds [56-59].

Because DMI is absent in centrosymmetric magnetic materials, skyrmion bubbles can have random spin helicity i.e., clockwise and anti-clockwise spin rotations are degenerate [60]. Therefore, unlike skyrmion in chiral magnets, spin helicity in skyrmion bubbles is not fixed by crystallographic chirality.

2.4 Detection of skyrmions

After understanding the properties of skyrmions, in this section, we would like to address, how skyrmions can be detected experimentally. First, a brief overview of magnetic imaging techniques used for direct imaging of skyrmions is given. Thereafter, an indirect method of skyrmion detection i.e., electrical detection is presented.

2.4.1 Magnetic imaging techniques

Magnetic skyrmions were first characterized using the small angle neutron scattering (SANS) technique performed on MnSi crystal, which revealed the skyrmion lattice in

reciprocal space [14]. To probe into the static and dynamic properties of skyrmions, their real-space observation at nano-scale is highly desired. The first real-space observation of skyrmions was made using Lorentz transmission electron microscopy (LTEM) [36]. Since then, skyrmions have been observed by various direct magnetic imaging techniques such as spin-polarized scanning tunneling microscopy (SP-STM) [54], magnetic force microscopy (MFM) [61], magneto-optical Kerr effect (MOKE) microscopy [62], spin-polarized low-energy electron microscopy (SPLEEM) [63], photoemission electron microscopy combined with X-ray magnetic circular dichroism (XMCD-PEEM) [39], magnetic transmission soft X-ray microscopy (MTXM) [41], and NV (nitrogen-vacancy) magnetometry [64]. In this thesis, MFM is used to study magnetic skyrmions and antiskyrmions. MFM is a well-established technique for the investigation of magnetic nanostructures with a high spatial resolution, which will be discussed in chapter 3.

2.4.2 Electrical detection

Apart from the direct experimental observation of skyrmions, another way of detecting skyrmions is an indirect method through electrical means by utilizing the topological Hall effect (THE). When current is passed through the skyrmion hosting metallic material, an interaction between the conduction electrons and the spin structure of skyrmions gives rise to an intriguing phenomenon known as the topological Hall effect (THE) [65]. The spatial variation of localized magnetization within the spin structure of the skyrmion generates a fictitious magnetic field known as emergent magnetic field [65, 66]. The coupling of conduction electrons to the emergent magnetic field of the skyrmion causes a transverse deflection of the electrons, thus, giving rise to an unconventional Hall signal i.e., THE. A schematic of THE is shown in Fig. 2.5a. THE is directly proportional to the skyrmion density and therefore labeled as a hallmark for the presence of the skyrmions.

THE was first experimentally observed in the bulk crystal of MnSi [35]. Fig 2.5b shows the topological Hall resistivity measured for MnSi at various temperatures in the “A phase” i.e., skyrmion lattice phase. This effect has been observed in the thin films of various systems hosting skyrmions [42, 67] and antiskyrmions [68, 69]. Due to the unique signature of THE for non-collinear spin textures, it can be utilized for local detection of skyrmions in a racetrack device. The electrical detection of skyrmions was recently realized in multilayer racetrack devices at room temperature by combination MFM and Hall resistivity measurements [70], as shown in Fig. 2.5c-d.

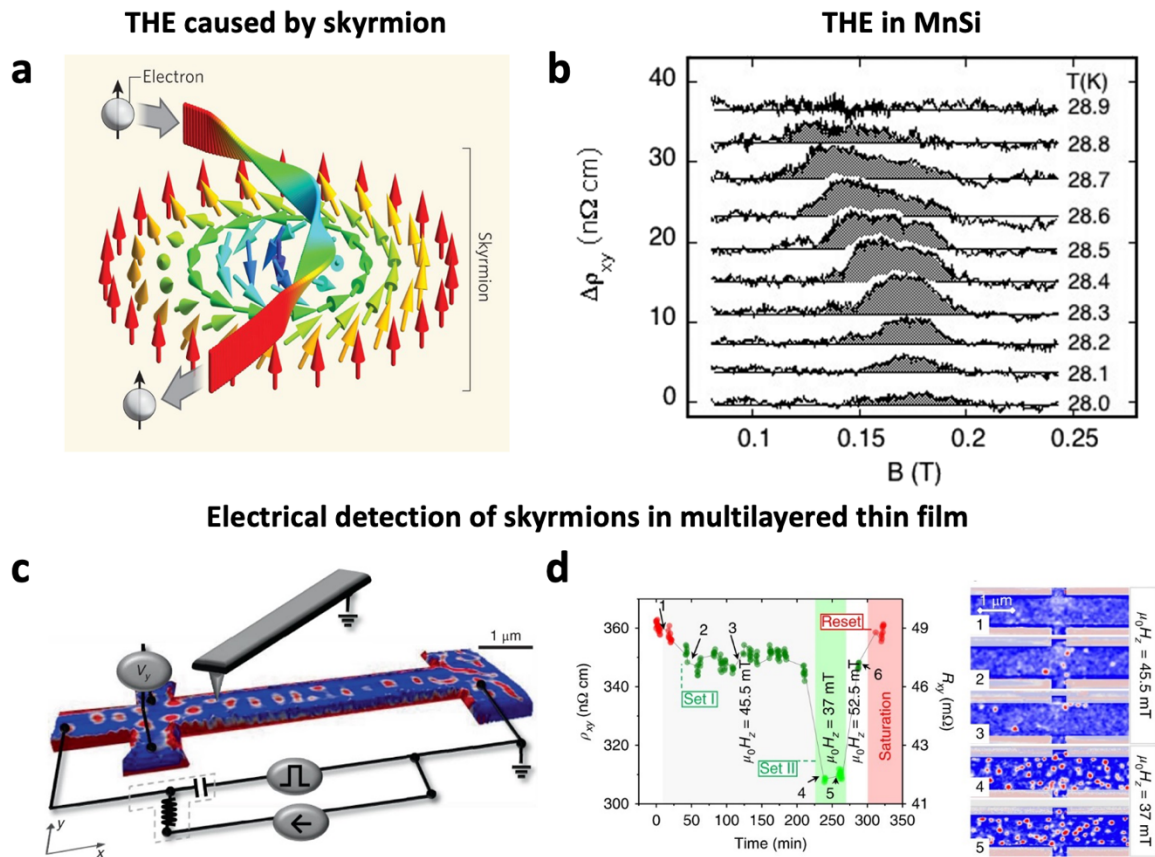


Fig. 2.5: Electrical detection of skyrmions utilizing the topological Hall effect (THE). (a) A schematic of THE caused by skyrmion. (Reprinted by permission from Springer Nature Customer Service Centre GmbH: Springer Nature, Nature, [71], (Single skyrmions spotted, Christian Pfleiderer *et al.*), COPYRIGHT (2010)). (b) Temperature-dependent Topological Hall resistivity of MnSi for ‘A-

Phase'. (Reprinted figure with permission from [35] as follows: A. Neubauer, C. Pfleiderer, B. Binz, A. Rosch, R. Ritz, P. G. Niklowitz, and P. Böni, Topological Hall Effect in the A Phase of MnSi, *Physical Review Letters*, 102, 186602 (2009). Copyright (2009) by the American Physical Society.) (c) An integrated experimental setup of magnetic force microscopy for electrical measurements of skyrmions in multilayer racetrack device. The blue and red contrast represents the up and down magnetization of the sample. (d) Measured Hall resistivity and Hall resistance at the different magnetic fields as a result of the skyrmions nucleation by current pulses. MFM images at different fields corresponding to the Hall resistivity. (Figure c-d, Reprinted by permission from Springer Nature Customer Service Centre GmbH: Springer Nature, *Nature Nanotechnology*, [70], (Electrical detection of single magnetic skyrmions in metallic multilayers at room temperature, Davide Maccariello *et al.*), COPYRIGHT (2018))

2.5 Experimental realization of skyrmions

After understanding the properties of skyrmions, experimental observation of magnetic skyrmions will be discussed in this section. Here, we focus only on skyrmions stabilized through the DMI in compounds with non-centrosymmetric crystal structures. Experimental discovery of Bloch, Néel, and antiskyrmions in a variety of materials are briefly discussed.

2.5.1 Experimental observation of Bloch skyrmions

Magnetic skyrmions were first predicted to exist in chiral magnets [48]. These non-trivial magnetic structures were first experimentally revealed in reciprocal space using small-angle neutron scattering (SANS) in non-centrosymmetric B20 compound MnSi [14]. Fig. 2.6a shows the magnetic field versus temperature (B - T) phase diagram for the bulk sample of MnSi. The ground state of MnSi is a helical phase at $B=0$. At certain temperatures, an increase in the magnetic field changes the helical phase to the 'A-phase' which represents

the skyrmion lattice phase. Fig. 2.6b shows a typical SANS image for the A-phase. The six-fold intensity maxima in reciprocal space correspond to the magnetic modulation along with the crystallographic directions, which is equivalent to a periodic skyrmion lattice.

These findings in the bulk sample were further followed up by real-space observation of a two-dimensional Bloch skyrmion crystal [36]. These measurements were performed in the thin lamella of $\text{Fe}_{0.5}\text{Co}_{0.5}\text{Si}$ using Lorentz transmission electron microscopy (LTEM). Fig. 2.6c shows an LTEM image of the skyrmion lattice, where arrows represent the orientation of in-plane magnetic moments. Since $\text{Fe}_{0.5}\text{Co}_{0.5}\text{Si}$ compound belongs to the B20 crystal structure, the inherent bulk DMI stabilizes Bloch skyrmions, as discussed in section 2.3. A B - T phase diagram for the thin lamella of single-crystalline $\text{Fe}_{0.5}\text{Co}_{0.5}\text{Si}$ is shown in Fig. 2.6d. Here, the skyrmion phase is stabilized over a large range of temperatures in contrast to the case for bulk sample, Fig. 2.6a, where the skyrmion phase is limited to a narrow temperature range.

Since the first observation of skyrmions in MnSi, the Bloch skyrmions have been discovered in several non-centrosymmetric B20 bulks and thin-film systems [37, 72-75].

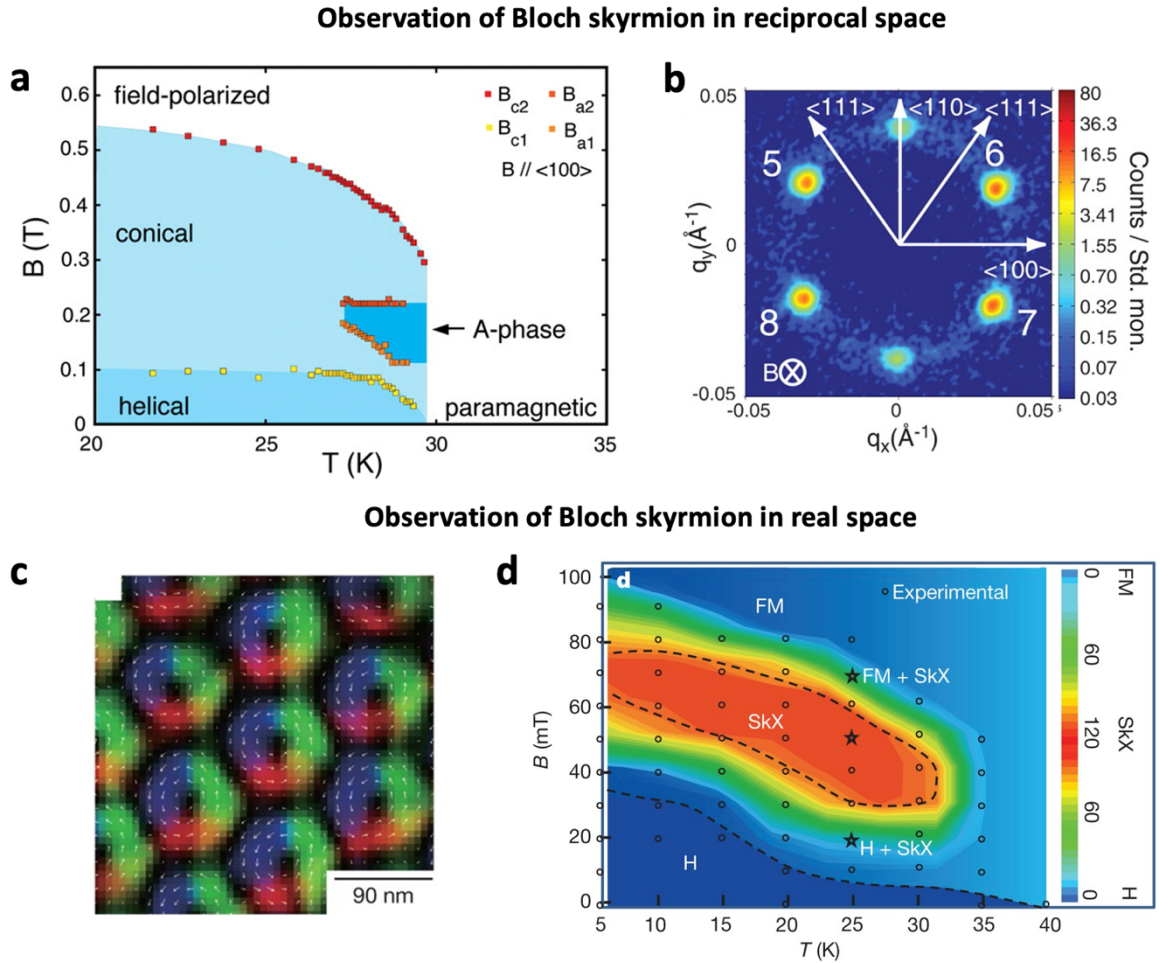


Fig. 2.6: Experimental observation of Bloch skyrmion in B20 alloys. (a) Phase diagram of MnSi obtained from SANS measurements. The “A-Phase” represents the skyrmion lattice phase. (b) Typical SANS image for the ‘A-Phase’ with six-fold intensity maxima in reciprocal space corresponding to the periodic skyrmion lattice. (Figure a-b from [14]. Reprinted with permission from AAAS). (c) LTEM image of the Bloch skyrmion lattice in $\text{Fe}_{0.5}\text{Co}_{0.5}\text{Si}$. The arrows and colors indicate the in-plane orientation of the magnetization. (d) Field-temperature phase diagram of Bloch skyrmions obtained using LTEM. The symbols H, Skx, and FM represent the helical structure, skyrmion crystal structure, and ferromagnetic structure, respectively. (Figure c-d, Reprinted by permission from Springer Nature Customer Service Centre GmbH: Springer Nature, Nature, [36], (Real-space observation of a two-dimensional skyrmion crystal, X. Z. Yu *et al.*), COPYRIGHT (2010))

2.5.2 Experimental observation of Néel skyrmions

Following observations of Bloch skyrmions in the bulk samples, Néel skyrmions were discovered at the interface of Fe and Ir (111) by spin-polarized scanning tunneling microscopy (SP-STM) [54], as shown in Fig. 2.7. In thin film heterostructures, Néel skyrmions are prominently formed due to the presence of an anti-symmetric interfacial DMI (iDMI). In such systems, iDMI occurs at the interface between a ferromagnet and a heavy metal due to the presence of large spin-orbit coupling and inversion symmetry breaking [12, 13, 76]. Further studies revealed that Néel skyrmions could be stabilized in a variety of magnetic thin-film heterostructures even at room temperature [39, 41, 42].

Other than multilayer films, Néel skyrmions have also been reported in non-centrosymmetric bulk compounds with C_{nv} ($n=3, 4, 6$) crystal structures such as GaV_4S_8 with C_{3v} structure [43], VOSe_2O_5 with C_{4v} [44] and PtMnGa crystal with C_{3v} structure [26].

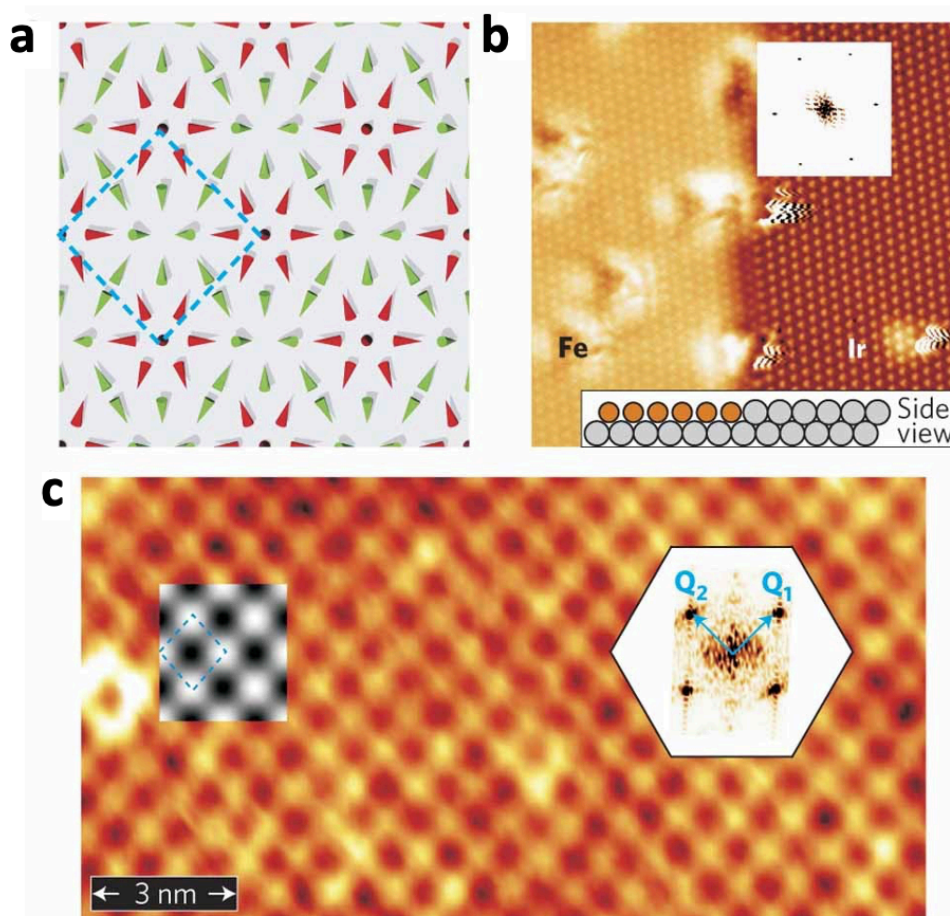


Fig. 2.7: Experimental observation of Néel skyrmion at the interface of Fe and Ir (111). (a) Sketch of the Néel skyrmion lattice. (b) STM image of the hexagonal Fe layer at Ir edge. (c) ST-STM image of the nanoskyrmion lattice. The bright and dark contrast represents magnetization parallel and antiparallel to the tip magnetization. (Reprinted by permission from Springer Nature Customer Service Centre GmbH: Springer Nature, Nature Physics, [54], (Spontaneous atomic-scale magnetic skyrmion lattice in two dimensions, Stefan Heinze *et al.*), COPYRIGHT (2011))

2.5.3 Experimental observation of antiskyrmions

Magnetic antiskyrmions were first theoretically predicted to exist in systems with bulk DMI [48, 77]. Antiskyrmions were first experimentally discovered in Heusler compound $\text{Mn}_{1.4}\text{Pt}_{0.9}\text{PdSn}$ with D_{2d} symmetry using LTEM [20], as shown in Fig. 2.8. Since then, antiskyrmions have been observed in various D_{2d} Heusler compounds [21, 23-25, 45, 46]. These spin textures are stabilized by anisotropic DMI which comes from the underlying D_{2d} crystal symmetry. Since DMI is anisotropic in D_{2d} systems, it has no component along the thickness direction [001], unlike B20 compounds. This leads to enhanced stability of antiskyrmions with respect to field and temperature [46]. An interplay between DMI and dipolar energy leads to the tunability of antiskyrmion size by simply varying the thickness of the lamella [21], which will be discussed in Chapter 4. Furthermore, antiskyrmions have been found to co-exist with Bloch skyrmions in the same material, which makes them promising for device applications [23-25].

In addition to D_{2d} Heusler compounds, recently antiskyrmions have been reported in S_4 symmetry material $\text{Fe}_{1.9}\text{Ni}_{0.9}\text{Pd}_{0.2}\text{P}$ [47].

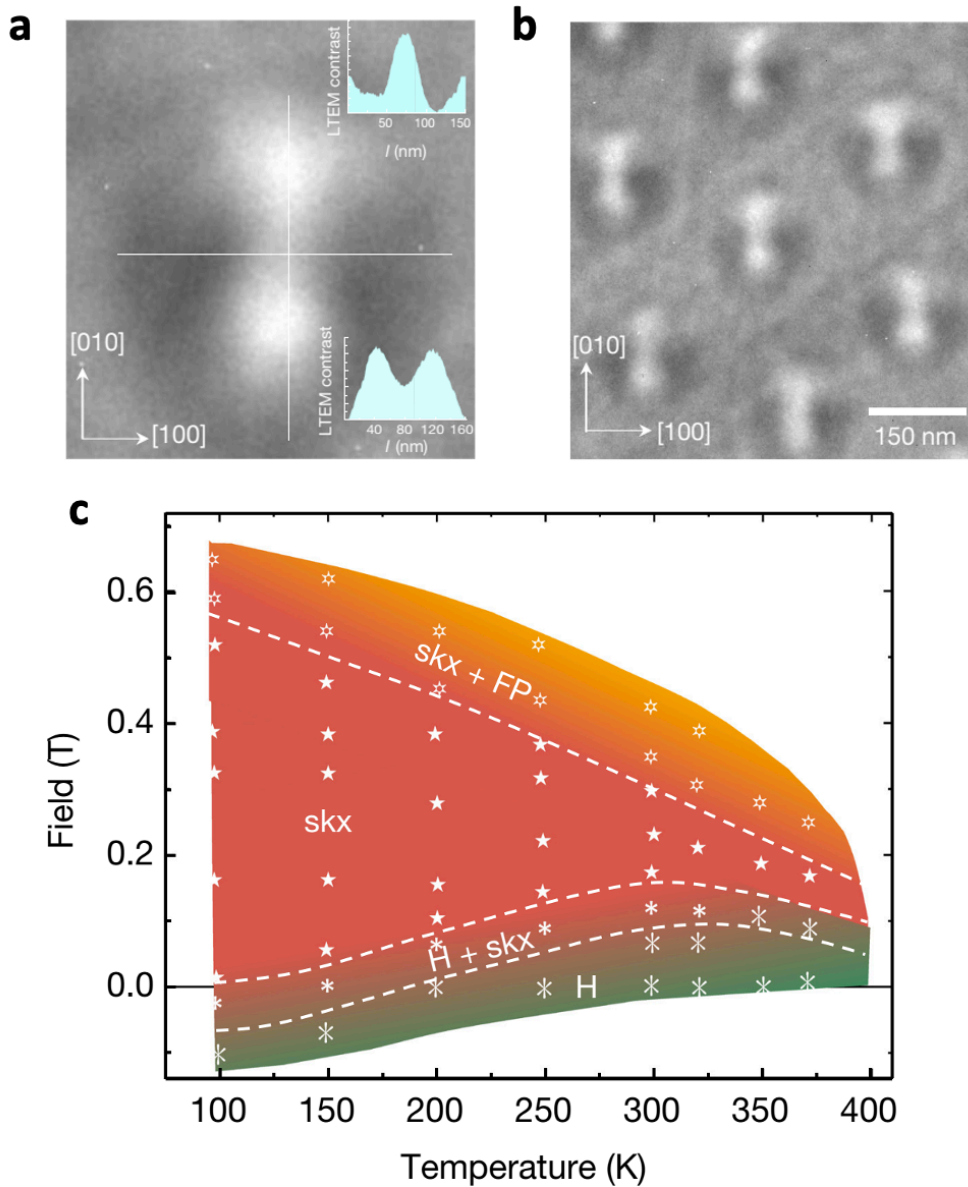


Fig. 2.8: Experimental observation of antiskyrmion in $\text{Mn}_{1.4}\text{Pt}_{0.9}\text{Pd}_{0.1}\text{Sn}$. (a) LTEM contrast of a single antiskyrmion which shows two bright and two dark spots along the [010] and [100] directions, marked by white lines. (b) LTEM image of a hexagonal lattice of antiskyrmions. (c) Field-temperature phase diagram of antiskyrmions. The symbols H, skx, and FP represent helical phase, antiskyrmions, and field polarized phase, respectively. (Reprinted by permission from Springer Nature Customer Service Centre GmbH: Springer Nature, Nature, [20], (Magnetic antiskyrmions above room temperature in tetragonal Heusler materials, Ajaya K. Nayak *et al.*), COPYRIGHT (2017))

3. Experimental methods

In this chapter, first magnetic force microscopy (MFM) is discussed, which is the basis of the results presented in this thesis. Then, sample preparation techniques are discussed which were used to prepare lamellae and thin films for MFM measurements. The last section describes the techniques used for structural and magnetic characterization of the samples.

3.1 Magnetic force microscopy (MFM)

In this section, a scanning probe microscopy technique called Magnetic force microscopy (MFM) is presented which is used to image and study non-collinear spin textures in this thesis. First, an introduction to the MFM technique and its working principle is discussed. Then, the experimental setup of variable-temperature MFM is presented.

3.1.1 Introduction to magnetic force microscopy

The study of magnetism at the nanoscale has attracted intense research interest in recent times due to the discovery of exotic magnetic objects, such as magnetic domain walls and skyrmions, and their technological applications in Spintronics. To visualize and study the properties of these nanoscale magnetic structures, a high-resolution imaging technique is required. Over time, a wide range of magnetic imaging techniques have been developed to image magnetic textures at the nanoscale, such as Magnetic force microscopy (MFM) [61], Lorentz transmission electron microscopy (LTEM) [36], Spin-polarized scanning tunneling microscopy (SP-STM) [38, 54], magneto-optical Kerr effect (MOKE) microscopy [62],

scanning transmission X-ray microscopy (STXM) [41], scanning superconducting quantum interference device (SQUID) microscopy [78] and nitrogen-vacancy (NV) magnetometry [64]. Among them, MFM is a widely used technique for measuring magnetic domains on a variety of materials and surfaces, due to its non-destructive, high resolution, and sensitivity. Also, MFM does not require specific sample preparation and it is compatible with measuring in vacuum or air. Furthermore, MFM becomes a valuable method to study various magnetic systems due to the wider range of temperature and magnetic fields. MFM can be used for the detection of magnetic objects for example magnetic domain walls [79], vortices on superconductors [80], magnetic skyrmions [61], and antiskyrmions [21]. By controlling the magnetic interaction between the sample and MFM probe, magnetic domains can be created and deleted. Thus, expanding the scope of the MFM technique beyond imaging. Moreover, MFM brings the advantage of studying the current-driven motion of the spin textures and simultaneously detecting their topological signal [70].

3.1.2 General principle

Magnetic force microscopy belongs to the family of scanning probe techniques [81], which utilizes the principle of atomic force microscopy (AFM) [82]. The main feature of the MFM is an AFM tip coated with magnetic material which is scanned across the magnetic surface to map out the z-component of the magnetic stray field emanating from the sample. In MFM, the magnetic signal is generated by a magnetostatic interaction between the stray field above the sample surface and the magnetic tip. A schematic of the interaction between MFM tip and sample stray field is shown in Fig. 3.1.

Typically, when the tip is brought into contact with the sample surface, the interaction force consists of all kinds of short- and long-range interaction forces depending upon the tip-sample separation. At a very small tip-sample distance, the interaction force is

3. Experimental methods

repulsive due to Coulomb repulsion or Pauli exclusion. At a large tip-sample distance, the interaction force is dominant from long-range attractive van der Waals, magnetostatic, or electrostatic forces. These contributions from short- and long-range interaction forces can be approximated in terms of Lennard-Jones potential [83]. The tip-sample interaction regime can be specified as ‘contact’ and ‘non-contact’, when the force is attractive and repulsive, respectively. In the MFM experiment, we are only interested in long-range magnetostatic forces. For this purpose, different MFM operation modes are utilized which are discussed below.

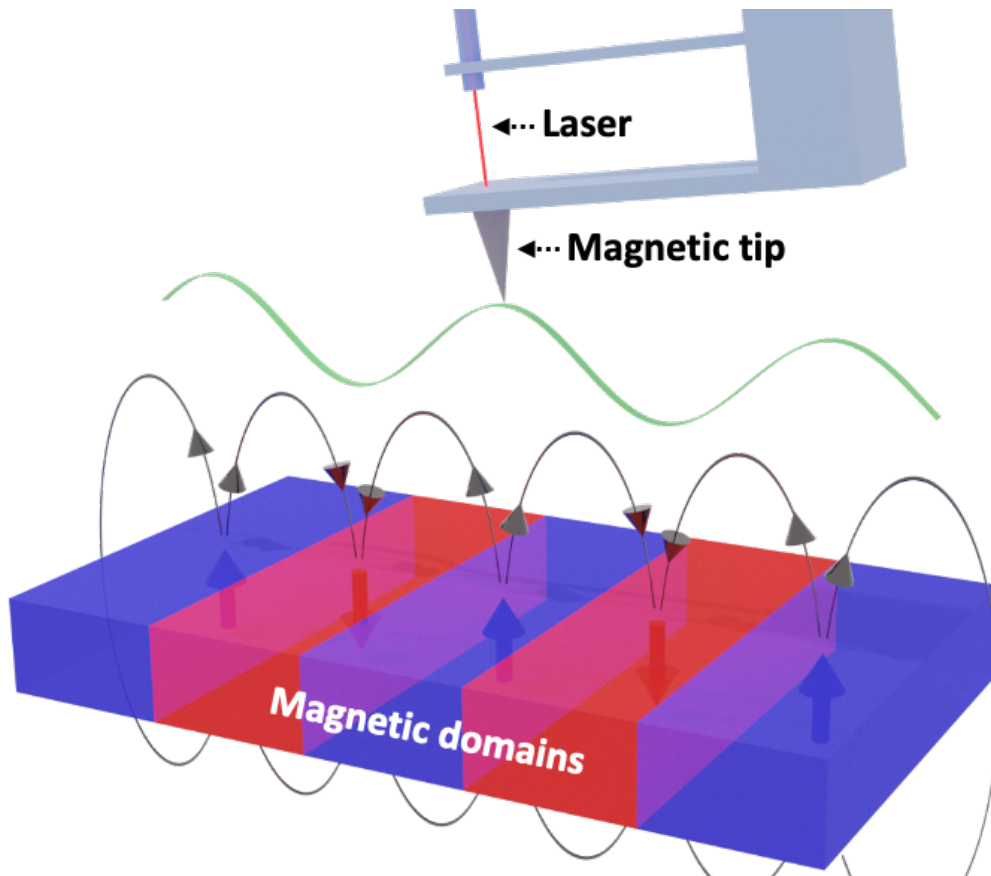


Fig. 3.1: Schematic of the MFM tip and sample interaction. The magnetic tip interacts with the stray field of the sample (black lines with arrow), which leads to a shift of the cantilever resonance frequency (green trace line). The resulting

deflection of the cantilever is recorded by the laser-detector system to produce an image.

The working principle of MFM is based on the detection of magnetic forces between the surface of a sample and the magnetic stray fields of a cantilever tip that is coated with a suitable magnetic film. To separate the topography and magnetic signal in MFM, a tapping or dynamic mode is employed in a pure noncontact regime of the tip-sample interaction. In dynamic mode, the cantilever is excited at its resonance frequency f_0 and scanned over the sample surface at a particular height (>10 nm). The tip-sample interaction leads to a change in the resonance frequency of the cantilever. The frequency shift, Δf , of the cantilever due to the magnetic forces can be expressed by using a dipole-dipole approximation [61]:

$$\Delta f = -f_0 \frac{\mu_0}{2k} m_{tip,z} \frac{\partial^2 H_S}{\partial z^2} \quad (3.1)$$

where f_0 is the resonance frequency of the cantilever, k is the spring constant of the cantilever, μ_0 is the vacuum permeability, $m_{tip,z}$ is the magnetic dipole moment of the tip, and H_S is the magnetic field created by the sample. Magnetic information in the MFM images hence represents the second derivative of the z -component of the stray field created by the sample, which corresponds to the out-of-plane magnetization of the sample. The magnetic signal i.e., Δf can be detected by phase or frequency modulation while measuring in constant frequency, constant height, or tapping/lift mode.

A typical MFM image is shown in Fig. 3.2. A helical phase in wedge lamella of $Mn_{1.4}PtSn$ is shown in Fig. 3.2a and the corresponding line profile of MFM contrast is shown in Fig. 3.2b.

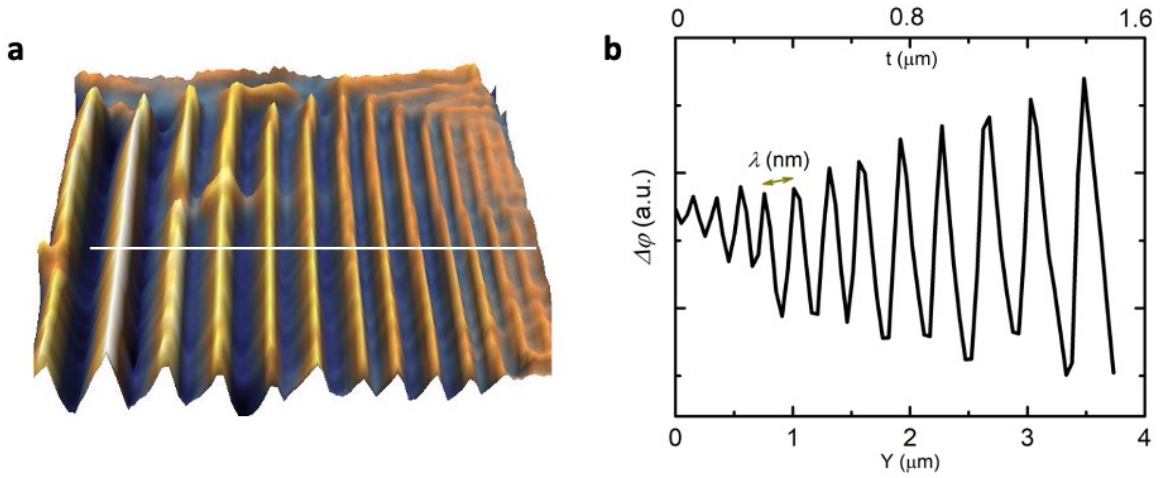


Fig. 3.2: Typical MFM image. (a) 3D MFM image of helical phase in wedge lamella of Mn_{1.4}PtSn. (b) Line profile of MFM contrast along the white line shown in (a).

3.1.3 MFM experimental technique

All of the MFM measurements presented in this thesis are conducted using the Attocube system (attoAFM I) in a liquid helium-based cryostat (attoLIQUID2000) for convenient temperature control (1.5-320 K). The cryostat is equipped with a vector superconducting magnet, which is capable of applying high magnetic fields both in-plane (3 T) and out-of-plane (9 T) to the sample.

The MFM system consists of a microspore stick, which holds the measurement head on its lower end. Fig. 3.3a shows the standard setup of the MFM measurement head. The sample to be measured is placed on a positioner and scanner stack unit. There is a temperature sensor and a small heater underneath the sample holder to control the sample temperature. Above the sample housing unit, the measurement head contains the AFM cantilever, which is placed before the end of an optical fiber. The length of the optical cavity formed between the fiber and cantilever is measured by a laser-detector system. The

mechanical excitation of the cantilever is realized by applying an AC voltage to the diether piezo.

The magnetic signal can be detected either from the phase shift while measuring at constant frequency or correspondingly from the measured frequency shift in a phase-locked mode to keep a constant phase shift. MFM measurements are performed at bigger tip-sample distances (>40 nm) to avoid intermixing of the magnetic and topographic signals.

To perform variable temperature MFM measurements, the microscope stick is first placed in a vacuum tube and evacuated. Once the vacuum inside the tube reaches $\sim 10^{-4}$ mbar, it is then backfilled with 20 mbar helium exchange gas for exchanging the heat outside the vacuum tube. This tube is then cooled by insertion into a variable temperature insert (VTI) of the liquid cryostat. Fig. 3.3 b-c shows images of the MFM system with the cryostat. To achieve a low temperature (1.5 K) below 4.2 K, the vapor pressure above the helium bath is reduced by pumping with a rotary pump.

3. Experimental methods

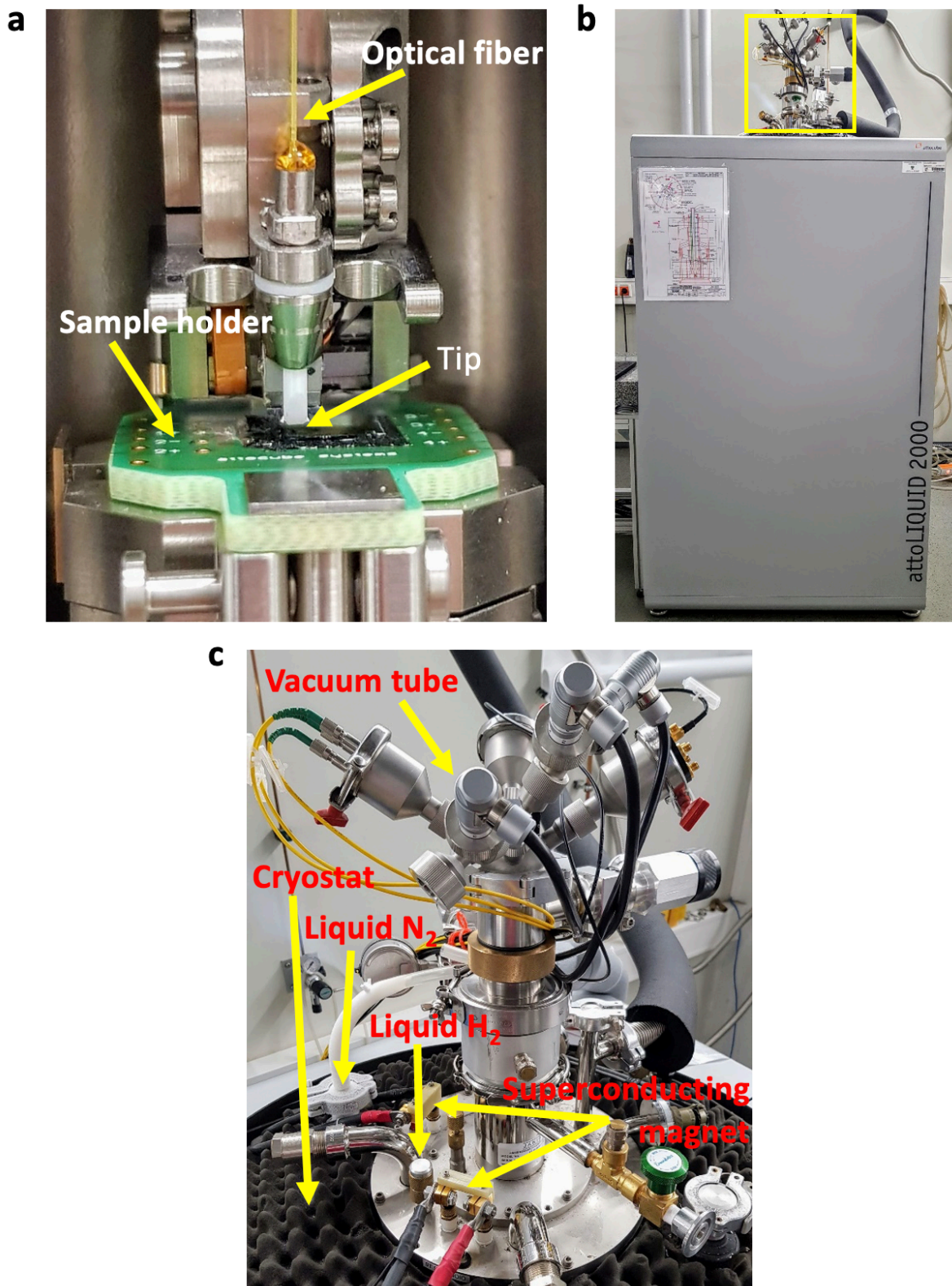


Fig. 3.3: Images of the MFM system. (a) MFM microscope head. (b) Liquid cryostat with MFM microscope (highlighted in the yellow box). (c) Top view of the MFM system inserted in the cryostat.

3.2 Sample preparation

The samples in this thesis work were prepared using three different techniques. In this section, firstly, the bulk crystal and lamella preparation methods are explained. Lastly, the thin film preparation method is described.

3.2.1 Bulk crystal preparation

Single crystals of $\text{Mn}_{1.4}\text{PtSn}$ were prepared using a flux growth method. First, high purity elements of manganese (Mn) and platinum (Pt) in an atomic ratio of 3:1 and a weight of 0.75 grams were loaded into an alumina crucible along with the element of tin, Sn, (~10 g). This alumina crucible was sealed in a quartz ampule under an argon pressure of 0.2 bar. The quartz ampule was then inserted into a furnace and heated at 1050 °C for 24 h to achieve a good homogeneous solution. This solution was first cooled quickly to 650 °C and then slowly cooled to 450 °C, where it was kept for a few hours to crystallize more of the desired compound. After growth, the flux with excess Mn was removed by centrifugation process at high temperatures (400-450 °C).

Polycrystalline samples of $\text{Mn}_2\text{Rh}_{0.95}\text{Ir}_{0.05}\text{Sn}$ were prepared by inductive melting of stoichiometric amounts of the elements Mn, Ir (iridium), Rh (rhodium), and Sn with high purity (>99.99%) in alumina crucibles. Due to the high melting points of Ir and Rh, their powders were first pre-alloyed together with Sn. The resulting alloy was kept in the melted state for approximately a minute before cooling down. This procedure was repeated three times to ensure good homogenization of the pre-alloy. Then, Mn chips were added to the Rh/Ir–Sn ingot followed by remelting and turning the ingots several times for better homogeneity. This procedure ensures a low loss of Mn due to evaporation. The as-prepared ingots were then packed in closed tantalum crucibles that were further encapsulated in an

evacuated fused quartz glass ampule. Subsequent heat treatment for 1 week at 900 °C was performed followed by quenching in an ice-water mixture resulting in the final polycrystalline ingot of $\text{Mn}_2\text{Rh}_{0.95}\text{Ir}_{0.05}\text{Sn}$ compound.

Single crystals of PtMnGa were grown from a melt using the vertical Bridgman crystal growth technique. First, polycrystalline ingots of PtMnGa were prepared using induction melting of stoichiometric mixture of Mn, Pt, and Ga (gallium) pieces of 99.99% purity. The resulting alloy was annealed for three days at 900°C followed by quenching in an ice-water mixture. The crushed precursor pieces were then placed in a custom-designed sharp-edged alumina tube and finally sealed inside a tantalum tube with an argon atmosphere. The crystal growth temperature was controlled using the thermocouple situated at the bottom of the tantalum ampoule containing the sample. The sample was first heated to 1150 °C, hold there for 12 hours, and then slowly cooled to the temperature of 900 °C with a rate of 0.8 mm/h. The single crystallinity of the as-prepared crystal was confirmed by the white-beam backscattering Laue X-ray diffraction technique at room temperature.

3.2.2 Focused ion beam milling (FIB)

The focused ion beam is a technique designed for modifying the sample's geometry by removal of material using heavy ions. It is pretty similar to scanning electron microscopy (SEM) which utilizes focused ion beams to scan the sample surface except that the primary beam of FIB consists of accelerated ions instead of electrons. FIB uses ions that have a much heavier mass than electrons so that they can transfer enough momentum to the nuclei of the sample. When accelerated ions hit the sample, it results in atoms leaving the sample surface. This process leads to material removal and desired sample size can be obtained in the form of nanowires or lamellae.

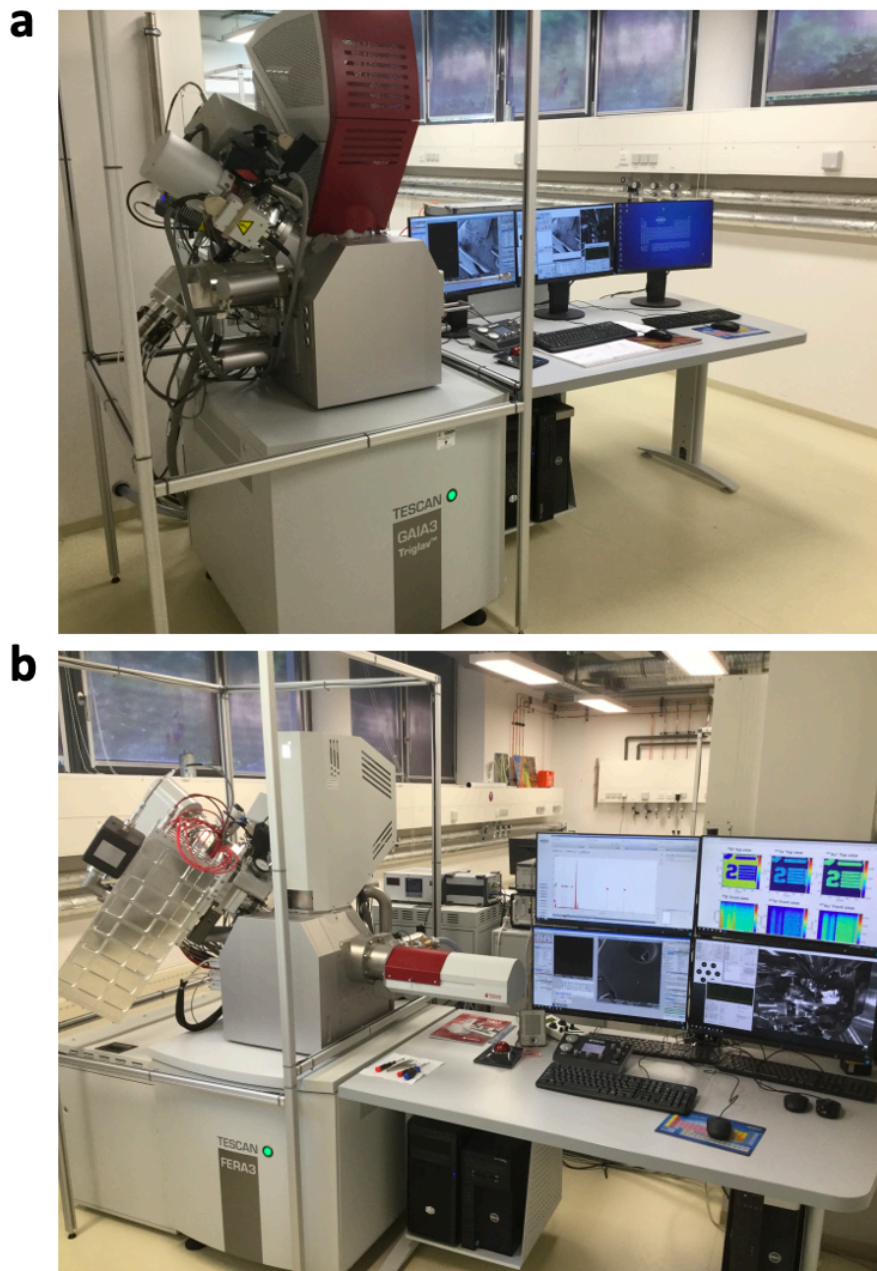


Fig. 3.4: FIB systems. (a) Ga⁺ ion FIB GAIA 3 and (b) Xe plasma FIB FERA

Single crystalline lamellae of $\text{Mn}_{1.4}\text{PtSn}$, $\text{Mn}_2\text{Rh}_{0.95}\text{Ir}_{0.05}\text{Sn}$, and PtMnGa were fabricated from [001] oriented grains of bulk crystals using dual-beam SEM-FIB systems TESCAN GAIA 3 (Ga⁺ FIB) and FERA 3 (Xe plasma FIB), that are shown in Fig. 3.4a and b, respectively. Both FIB systems are equipped with a Gas Injection System (GIS) to deposit different materials. The Ga⁺ FIB system has an ion beam energy range of 0.5–30 keV with

3. Experimental methods

a resolution of < 2.5 nm at 30 keV and is suitable for preparing lamella samples. The Xe plasma FIB has the ion beam energy range of 3 – 30 keV with a resolution of < 15 nm at 30 keV and is best suitable for milling large-size structures. Both FIB systems were used for lamella preparation so that the observed results are independent of the artifacts or damage caused by Ga ion implantation.

A scanning electron microscopy (SEM) image of the typical wedge lamella prepared using FIB is shown in Fig. 3.5a. along with a schematic diagram of wedge lamella in Fig. 3.5b.

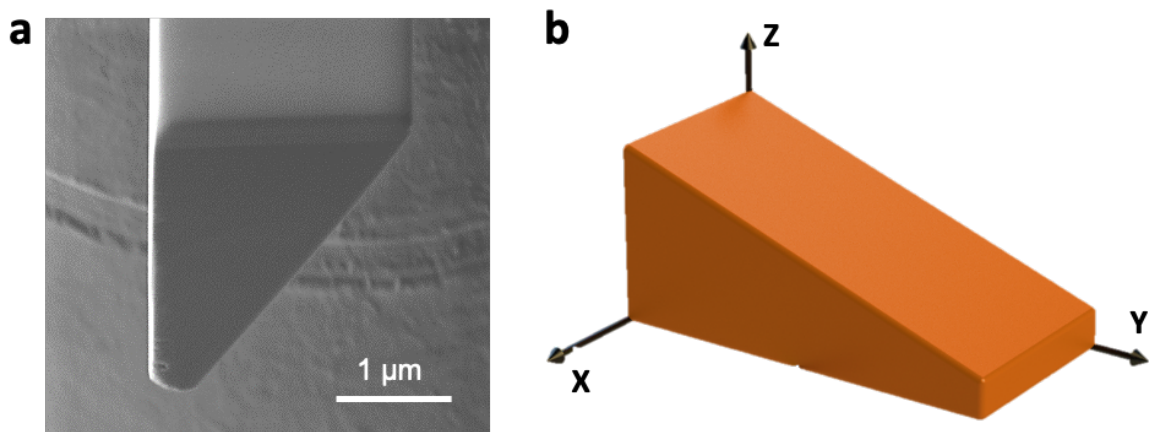


Fig. 3.5: FIB prepared wedge lamella (a) Typical SEM image of a wedge-shaped lamella. (b) Schematic of the lamella.

For MFM measurements, lamellae prepared using FIB were transferred on a pre-patterned silicon substrate with the help of the nano manipulator needle in FIB and fixed by depositing Pt on the corner of the lamella. This step makes it easier to locate such very small lamella (~ 5 - $10 \mu\text{m}^2$) for MFM scan. A typical example of such a lamella is shown in Fig. 3.6.

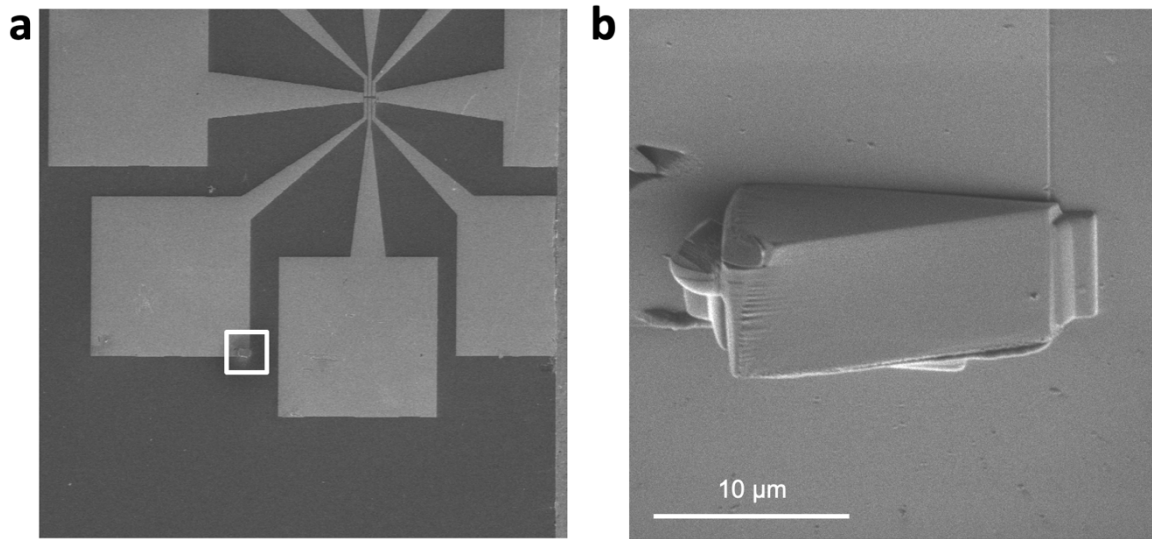


Fig. 3.6: Lamellae for MFM measurements. (a) Overview of Lamella placed on a pre-patterned Si substrate. (b-c) Magnified view of the white box in a.

3.2.3 Thin film preparation

The thin films of Mn₂RhSn in this work were grown heteroepitaxially on MgO (001) single crystal substrates. A BESTEC UHV magnetron sputtering system was used for the thin films deposition using three independent Mn, Rh, and Sn sources in a confocal geometry. The deposition chamber was evacuated to a base pressure ($<2 \times 10^{-9}$ mbar) before the deposition, while the process gas (Ar 5N) pressure was 3×10^{-3} mbar. The Mn₂RhSn films were co-sputtered from Mn, Rh, and Sn targets with the sputter rate adjusted on each magnetron to obtain the correct stoichiometry. The films were grown at 400 °C and then post-annealed in situ for 30 min to improve chemical ordering. The films were capped with 3 nm-thick TaN films at room temperature to prevent oxidation. The film structure and stoichiometry were characterized using X-ray diffraction (XRD), X-ray photoelectron spectroscopy (XPS), and Rutherford backscattering spectrometry (RBS).

3.3 Additional measurement techniques

3.3.1 Lorentz transmission electron microscopy (LTEM)

LTEM is a transmission electron microscope (TEM) based real-space magnetic imaging technique for the observation of magnetic structures like skyrmions in this work. In LTEM mode, when an electron is passed through the magnetic specimen, it experiences a Lorentz force induced by the in-plane magnetization of the sample. The electron is deflected from its original trajectory by this Lorentz force. The resulting deflection of the electron is visualized by focusing the beam over or under the specimen.

In this study, an aberration-corrected high-resolution TEM [FEI TITAN 800-300] was used to observe the magnetic contrast in the LTEM mode. An image of the LTEM system is shown in Fig. 3.7. The magnetic field was applied along the microscope axis by increasing the current in the objective lens. A double-tilt liquid nitrogen holder was used to vary the temperature of the sample from 100 K to 300 K. The in-plane field components were realized at the sample surface by tilting the sample holder up to $\pm 32^\circ$.

3.3.2 X-ray diffraction (XRD)

The XRD technique is based on irradiating a sample with powerful x-rays and measuring the scattering angles and intensities of the x-rays that leave the sample. In this thesis, a detailed investigation of the crystal structure of the Mn₂RhSn thin films was carried out by XRD using a high brilliance gallium-Jet X-ray source and a six-circle diffractometer specially designed for the study of thin films. The X-ray source was operated at 70 keV and 100 W power emitting Ga-K α radiation ($\lambda=1.3414 \text{ \AA}$).



Fig. 3.7: LTEM system (TITAN 80-300 from FEI)

The monochromatized and focused X-ray beam is incident on the sample under a constant grazing incidence angle of $\mu = 1^\circ$ to the surface. The horizontal and vertical beam size was $2 \text{ mm} \times 100 \text{ }\mu\text{m}$. Integrated reflection intensities from the sample were collected by a six-circle x-ray diffractometer operated in the z-axis mode by rotating the sample around its surface while the two-dimensional pixel detector is kept fixed at a constant angle to accept the scattered beam. The crystal structure analysis was carried out by least-squares refinement of calculated structure factor magnitudes to the observed ones.

3.3.3 Magnetometer quantum interference device (SQUID)

The SQUID system consists of a magnetometer quantum interference device to detect the total magnetic moment of the sample. It is a very sensitive detector of magnetic flux and can detect extremely small changes of magnetic flux ($<10^{-8}$ emu) within the superconducting loops containing Josephson junctions.

The magnetization of the thin films and crystals studied in this thesis was measured in a Quantum Design MPMS3 SQUID magnetometer. The magnetization as a function of temperature (M - T curve) was measured in both zero-field cooling (ZFC) and field cooling (FC) modes. In ZFC, the sample was first cooled down to low temperature (2 K) in zero fields and the magnetization was measured in the presence of the contact magnetic field by increasing the temperature from 2 K to higher temperatures. In FC, the sample was cooled down to 2 K in the presence of a constant magnetic field. The easy axis of magnetization (along the c -axis) was confirmed by obtaining hysteresis loops (M - H curve) with a magnetic field applied parallel and perpendicular to the sample plane. The diamagnetic contribution of the MgO substrate to the magnetization signal of the Mn_2RhSn thin films was removed by subtracting the magnetic signal of the MgO substrate obtained in a separate measurement.

4. Tunable magnetic antiskyrmion size and helical period from nanometers to microns in a D_{2d} Heusler compound

This chapter discusses the wide range of tunability of the helical period and the size of the antiskyrmion in thin lamellae formed from a single crystal of $Mn_{1.4}PtSn$ with D_{2d} symmetry. Using a combination of MFM and LTEM, it is shown that by varying the thickness of lamella, the size of the antiskyrmion and corresponding helical period can be systematically tuned by more than an order of magnitude from ~ 100 nm to ~ 1.1 μ m. This extensive size tunability and intrinsic stability are unique to the D_{2d} antiskyrmion system in which both DMI and magnetostatic interactions play a significant role in stabilizing spin textures over a much-extended thickness range. The thickness-dependent behavior of the characteristic size of the spin texture in D_{2d} compound $Mn_{1.4}PtSn$ is distinct from other material systems (such as B20 bulk systems [37, 74, 84, 85], magnetic bubble systems [86-88], interfacial DMI systems [89-92] and C_{3v} systems [26] due to the important differences in the underlying physical mechanisms.

The following chapter of this cumulative thesis has been reprinted from my publication (Reprinted from [21]. Link to the Creative Commons license: <https://creativecommons.org/licenses/by/4.0/>):

T. Ma, **A. K. Sharma***, R. Saha, A. K. Srivastava, P. Werner, P. Vir, V. Kumar, C. Felser, S. S. P. Parkin. “Tunable Magnetic Antiskyrmion Size and Helical Period from Nanometers to Micrometers in a D_{2d} Heusler Compound”. *Adv. Mater.* **2020**, 32, 2002043. (*co-first author).

Tunable Magnetic Antiskyrmion Size and Helical Period from Nanometers to Micrometers in a D_{2d} Heusler Compound

Tianping Ma, Ankit K. Sharma, Rana Saha, Abhay K. Srivastava, Peter Werner, Praveen Vir, Vivek Kumar, Claudia Felser, and Stuart S. P. Parkin*

Skyrmions and antiskyrmions are magnetic nano-objects with distinct chiral, noncollinear spin textures that are found in various magnetic systems with crystal symmetries that give rise to specific Dzyaloshinskii–Moriya exchange vectors. These magnetic nano-objects are associated with closely related helical spin textures that can form in the same material. The skyrmion size and the period of the helix are generally considered as being determined, in large part, by the ratio of the magnitude of the Heisenberg to that of the Dzyaloshinskii–Moriya exchange interaction. In this work, it is shown by real-space magnetic imaging that the helix period λ and the size of the antiskyrmion d_{aSk} in the D_{2d} compound $\text{Mn}_{1.4}\text{PtSn}$ can be systematically tuned by more than an order of magnitude from ≈ 100 nm to more than $1.1 \mu\text{m}$ by varying the thickness of the lamella in which they are observed. The chiral spin texture is verified to be preserved even up to micrometer-thick layers. This extreme size tunability is shown to arise from long-range magnetodipolar interactions, which typically play a much less important role for B20 skyrmions. This tunability in size makes antiskyrmions very attractive for technological applications.

One of the major topics in spintronics today is the study of the steady state and dynamical properties of spin textures with various topologies.^[1] Amongst these are magnetic skyrmions (Sks) which are magnetic nano-objects with chiral magnetic boundaries, namely, an in-plane magnetized region that separates the interior and exterior of the object where the magnetization points up/down or vice versa. Another distinct magnetic nano-object, an antiskyrmion (aSk), that has a more complex

boundary than aSk, was recently discovered.^[2] The boundaries in an aSk are composed of successive left-hand Bloch, left-hand Néel, right-hand Bloch, and right-hand Néel wall segments.^[2] The intrinsic stability of aSks over a large range of field and temperature was recently demonstrated.^[3] The detailed magnetic structures of both Sks and aSks are controlled by the magnitude and symmetry of the Dzyaloshinskii–Moriya exchange interaction (DMI).^[4]

The dependence of Sks and helices on the thickness of the host material has been studied in several B20 materials including FeGe ,^[5] $\text{Mn}_{1-x}\text{Fe}_x\text{Ge}$ of various compositions,^[6] and $\text{Fe}_{0.5}\text{Co}_{0.5}\text{Si}$.^[7] In all these cases no significant dependence of the size of the Sk or the helix period on the thickness of the host compound was found. It was concluded that the fundamental length scale is determined by a competition between the

Heisenberg exchange and the DMI. By contrast, it was shown some time ago that the size and arrangement of achiral magnetic bubbles is strongly influenced by magnetostatic interactions.^[8] What have been called “biskyrmions” and “skyrmions” in centrosymmetric materials fall into this latter category.^[9] We show here that antiskyrmion systems are unique in that both DMI and magnetostatic interactions play a significant role and that, thereby, give rise to extensive size tunability as well as intrinsic stability. We demonstrate, using a combination of Lorentz transmission electron microscopy (LTEM) and magnetic force microscopy (MFM) that the size of the antiskyrmion scales with the period of the helical structure and that both can be tuned over a wide range of more than an order of magnitude by adjusting the thickness of the host layer in which they are imaged.

In these studies, we focus on exploring spin textures in thin lamellae formed from a single crystal of $\text{Mn}_{1.4}\text{PtSn}$ which is an inverse tetragonal Heusler compound with D_{2d} symmetry (see Supporting Information). High-quality single crystals were prepared using a flux method. One single crystal was fashioned into a uniform thickness lamella (L1) and several wedge-shaped lamellae (L2–L4) by Ga^+ focused ion beam milling. The spin textures reported here were imaged using two different techniques. LTEM was used to both confirm the existence of aSks and to explore their size and the helix period for thinner wedges. Thicker wedges were studied using MFM. A schematic drawing of the aSk spin texture, that consists of chiral boundaries formed from helicoids (Bloch-like) and cycloidal

T. Ma, A. K. Sharma, Dr. R. Saha, A. K. Srivastava, Dr. P. Werner, Prof. S. S. P. Parkin
Max Planck Institute of Microstructure Physics
Weinberg 2, Halle (Saale) D-06120, Germany
E-mail: stuart.parkin@mpi-halle.mpg.de

T. Ma, A. K. Sharma, A. K. Srivastava, Prof. S. S. P. Parkin
Institute of Physics
Martin Luther University
Halle-Wittenberg, Halle (Saale) D-06120, Germany

P. Vir, Dr. V. Kumar, Prof. C. Felser
Max Planck Institute for Chemical Physics of Solids
Nöthnitzer Straße 40, Dresden 01187, Germany



The ORCID identification number(s) for the author(s) of this article can be found under <https://doi.org/10.1002/adma.202002043>.

© 2020 The Authors. Published by WILEY-VCH Verlag GmbH & Co. KGaA, Weinheim. This is an open access article under the terms of the Creative Commons Attribution License, which permits use, distribution and reproduction in any medium, provided the original work is properly cited.

DOI: 10.1002/adma.202002043

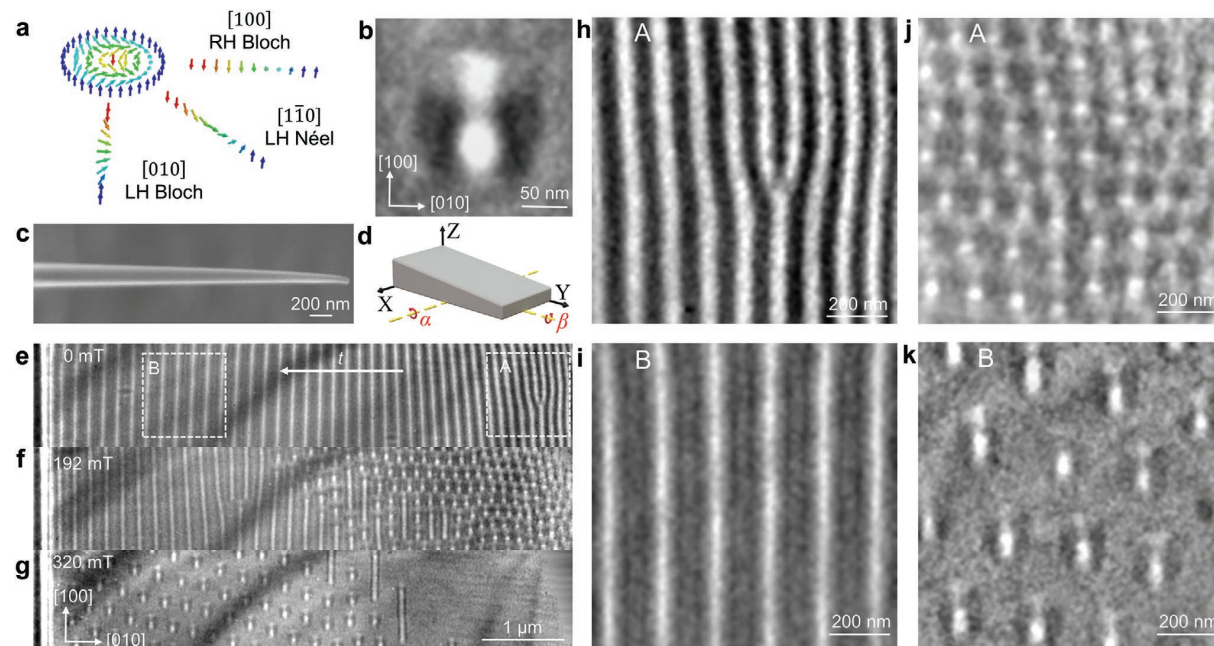


Figure 1. LTEM images of chiral spin textures in $\text{Mn}_{1.4}\text{PtSn}$. a) Schematics of aSk and spin configurations along different crystallographic directions. b) LTEM image of a single aSk obtained from a uniform thickness lamella in the presence of a magnetic field of 368 mT. c) SEM image of a wedge-shaped lamella that is $\approx 6.4 \mu\text{m}$ long: the wedge is rotated by 35° so it looks foreshortened. d) Schematic of a lamella where α and β correspond to the double-stage tilt angles. e–g) LTEM images at 0, 192, and 320 mT. h,i) Helical magnetic phase in zero magnetic field and j,k) magnified images of the aSk phase in thinner and thicker regions of the wedge labeled A and B in (e). All LTEM images were recorded with an underfocus value of 1.5 nm except for (b) which was recorded at an underfocus value of 2 nm. The magnetic field is along [001] in all cases.

spin propagations (Néel-like), is shown in **Figure 1a**. Néel domain walls of right- and left-hand propagate along the [110] and $[1\bar{1}0]$ directions, respectively, and Bloch domain walls of right- and left-hand propagate along the [100] and [010] directions, respectively. The helix in the D_{2d} system propagates along these latter directions (in the absence of an in-plane magnetic field) because its energy is lower for the Bloch structure (see Supporting Information).

Antiskyrmions were observed over a wide range of temperature and field in all samples. Only room temperature data are reported here because we find that the characteristic size of the spin textures in $\text{Mn}_{1.4}\text{PtSn}$ increases only a little as the temperature is reduced below room temperature, for otherwise the same thickness. Typical LTEM images are given in **Figure 1** for a lamella with a uniform thickness of $t \approx 200 \text{ nm}$ (sample L1) and a wedged lamella whose thickness varies from ≈ 116 to $\approx 206 \text{ nm}$ (sample L2). **Figure 1b** shows a magnified image of a single antiskyrmion in L1 that has a distinctive four-spot pattern with alternating black and white contrast, as previously observed for the closely related compound $\text{Mn}_{1.4}\text{Pt}_{0.9}\text{Pd}_{0.1}\text{Sn}$.^[2] A scanning electron microscopy (SEM) image of the wedge L2 is shown in **Figure 1c**, and a schematic diagram showing the definition of the coordinate axes and tilting angles used in the discussion below is given in **Figure 1d**. Electron energy loss spectroscopy was used to determine the thickness t of the wedge.^[10] The [001] zone axis is oriented along the transmission electron microscopy (TEM) column using a double-tilt sample holder. An LTEM image recorded in zero

magnetic field is shown in **Figure 1e**, in which the helices have been oriented along the [100] direction by using the in-plane component of an applied magnetic field. The most important finding is that the helix period varies significantly and monotonically from ≈ 96 to $\approx 185 \text{ nm}$ as the sample thickness is varied from ≈ 116 to $\approx 206 \text{ nm}$. Magnified images of two representative regions A and B, each $1 \mu\text{m} \times 1 \mu\text{m}$ in area, with thicknesses of ≈ 142 and $\approx 206 \text{ nm}$ are shown in **Figure 1h,i**. The helix period is $\approx 108 \pm 13 \text{ nm}$ in region A (**Figure 1h**) and $\approx 185 \pm 2 \text{ nm}$ in region B (**Figure 1i**). Note that across the width of the wedge, where the thickness is unchanged, the helix period does not change significantly.

The helical state evolves into an aSk phase when a perpendicular magnetic field is introduced. A magnetic field oriented along the microscope column is generated by applying current in the objective lens of the TEM. The following protocol was used: after an LTEM image is taken, the sample's [001] axis is tilted away from the TEM column axis by $\alpha = 30^\circ$ and the magnetic field is then increased in steps of 32 mT. Note that the presence of the in-plane field provided by the tilt allows for the aSk phase to be more easily stabilized.^[2] The sample is then tilted back to 0° and the next LTEM image is recorded. This tilting procedure and step-wise increase in magnetic field is repeated until the magnetic field is so large that the sample reaches the fully magnetized ferromagnetic state. Typical LTEM images of L2 corresponding to fields of 192 and 320 mT are shown in **Figure 1f,g**. A complete sequence of LTEM images of the wedge, starting from a zero-field helical state with both [100] and [010] propagating

components, as the field is increased till the fully polarized state is reached, is shown in Figure S1 of the Supporting Information. These data illustrate the sensitivity of the field dependence of the spin texture to thickness. Moreover, it is clear that the size of the aSk, just like the helix period, depends strongly on the wedge thickness. This is more visible in Figure 1j,k that show magnified images of regions A (192 mT) and B (320 mT), in which the aSk size is respectively, $\approx 128 \pm 5$ and $\approx 200 \pm 4$ nm. As shown previously for $\text{Mn}_{1.4}\text{Pt}_{0.9}\text{Pd}_{0.1}\text{Sn}$,^[2] the aSk size changes little with magnetic field. Thus, the aSk size variation arises predominantly from the change in thickness of the lamella rather than the change in magnetic field.

To explore possible variations in the aSk size and the helix period at thicknesses beyond those measurable by LTEM, we performed MFM measurements on two wedged lamellae with thicknesses varying from ≈ 630 to ≈ 4260 nm (L3) and ≈ 60 to ≈ 1600 nm (L4). The helical phase is clearly revealed in the MFM images. Typical results in zero magnetic field are summarized in Figure 2. An SEM image of the wedge L3 is shown in Figure 2a where the inset shows a schematic of the coordinate axis and the in-plane field direction φ_H . A saturation field of 1 T is applied in the plane of L3 at an angle φ_H and is then reduced to zero where the MFM image is taken: the MFM contrast corresponds to the stray field produced mainly by the out of plane magnetization component, M_z . By varying φ_H the helix propagation axis can be switched from predominantly [100] (Figure 2b, $\varphi_H = 180^\circ$) to predominantly [010] (Figure 2c,

$\varphi_H = 90^\circ$) or a mixture of both (Figure 2d, $\varphi_H = 135^\circ$). A representative line profile of M_z taken from Figure 2c is shown in Figure 2e. A typical 3D colormap of the helical region of an MFM image of wedge L4 is shown in Figure 2f. Both Figure 2e and Figure 2f clearly show a sinusoidal variation of M_z along the wedge, as well as a monotonic increase in helix period and amplitude with increasing lamella thickness. Note that the magnitude of the MFM signal increases approximately linearly with thickness. The helix period was determined from the peak to peak distance along an MFM line scan along the helix propagation direction, as shown in Figure 2e. The dependence of the helical period on the lamella thickness for all the wedges studied are shown in Figure 2g. Also included in the figure are LTEM data from Figure 1. The data show good agreement from wedge to wedge and between the LTEM and MFM techniques. The inset in Figure 2g shows the helical period variation for the wedge L2 obtained from LTEM studies and comparison with similar data on a wedge of comparable geometry for the sister compound $\text{Mn}_{1.4}\text{Pt}_{0.9}\text{Pd}_{0.1}\text{Sn}$.^[2] The data closely resemble one another.

The helical phase transforms into an aSk phase in the presence of a magnetic field, as shown in Figure 3 for wedge L3. Typical MFM images are shown for an initial field of zero, followed by magnetic fields of 300, 420, and 480 mT applied at 30° from the z-axis (Figure 3a–d) rotated toward the in-plane direction [010]. These images clearly show a gradual transformation from the helical phase into an aSk phase and finally into the

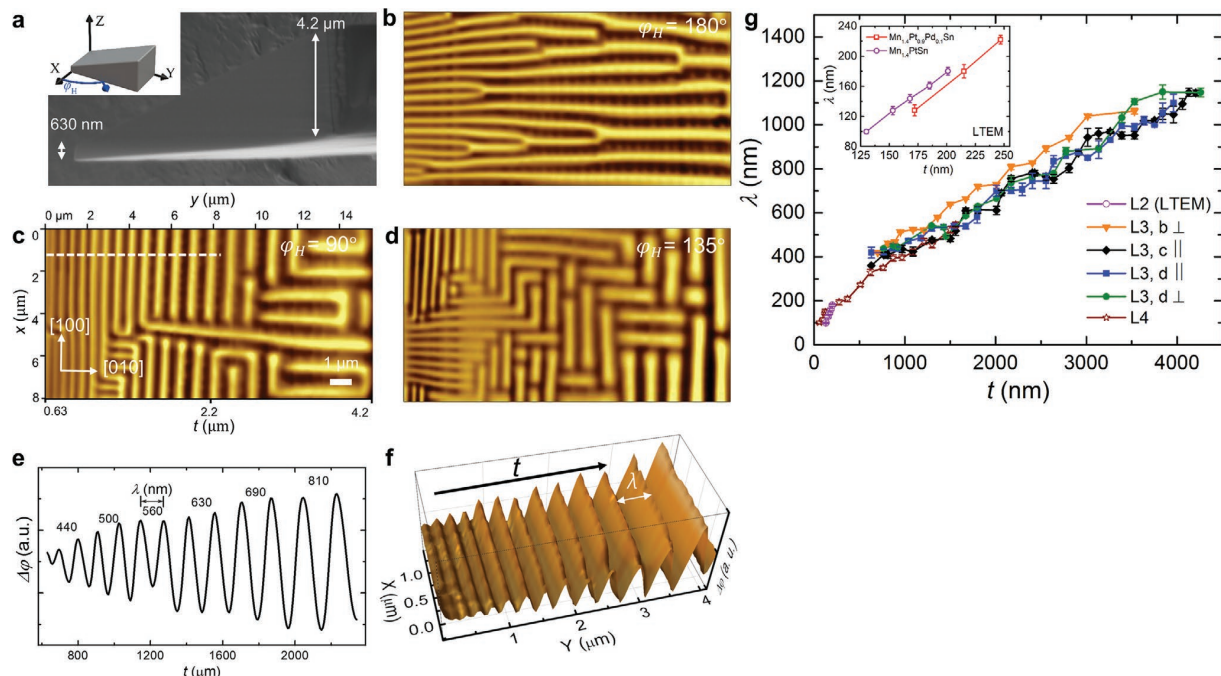


Figure 2. MFM images of helical spin textures in $\text{Mn}_{1.4}\text{PtSn}$. a) SEM image of the wedge-shaped lamella L3. The in-plane rotation angle φ_H is defined in the inset. b–d) MFM images with the helix aligned perpendicular (b), parallel (c), or both parallel and perpendicular (d) to the wedge. The size and thickness of the wedge are indicated in (c). The scanned area is $8 \times 16 \mu\text{m}^2$ where the lamella thickness increases from left to right. e) Line profile of MFM contrast, $\Delta\varphi$, along the white dashed line shown in (c). f) 3D colormap of $\Delta\varphi$ for wedge L4. g) Helix period as a function of thickness for wedges L3 and L4 for various orientations of the helices. Inset shows the variation of helical period with thickness in wedged lamellae of $\text{Mn}_{1.4}\text{PtSn}$ (L2) and $\text{Mn}_{1.4}\text{Pt}_{0.9}\text{Pd}_{0.1}\text{Sn}$ from LTEM studies. The error bar corresponds to the standard deviation of the helical period measured within the same thickness region.

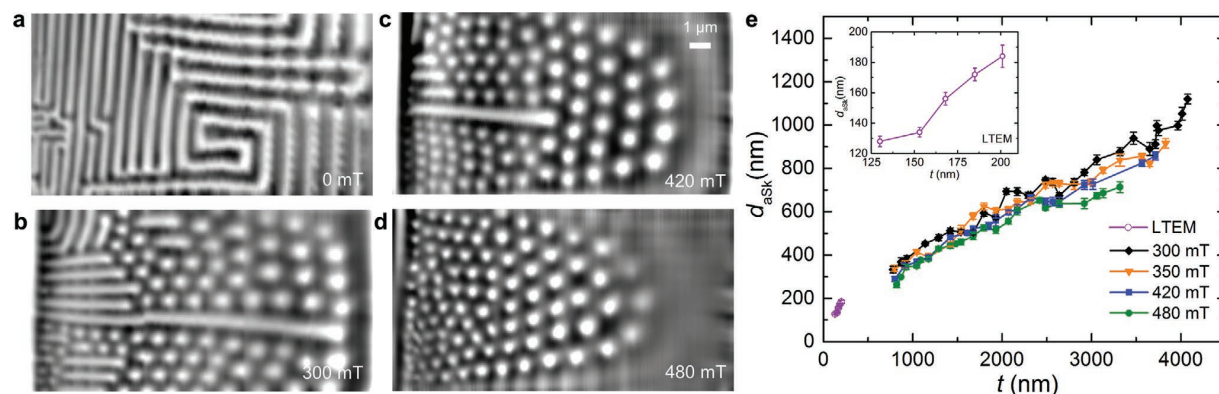


Figure 3. MFM images of antiskyrmion phase. a–d) Helical phase in zero magnetic field (a) and evolution to aSk phase as the field is increased to 300 mT (b), 420 mT (c), and 480 mT (d). The scanned area is $8 \times 16 \mu\text{m}^2$ where the thickness increases from left to right. e) aSk size versus thickness for various magnetic fields for wedge L4. Inset shows aSk size versus thickness for wedge L2 from LTEM images shown in Figure 1f,g.

fully polarized state that depends on sample thickness. The critical fields at which these transformations take place depend sensitively on the in-plane component of the field (see Supporting Information). A large thickness range where the aSk can be seen simultaneously was found for a tilt angle of $\approx 30^\circ$ which also matches the tilt angle used for the LTEM data. At a field of ≈ 550 mT the complete wedge was fully magnetized.

The aSk phase could be stabilized at all thicknesses which enabled the dependence of the aSk size on the lamella thickness to be determined. These results are summarized in Figure 3e together with results from the LTEM data in Figure 1 that are shown in the inset to Figure 3e. The protocol used to determine the aSk size is discussed in the Supporting Information. The combined MFM and LTEM data clearly show that the aSk size has a weak dependence on magnetic field but a very strong dependence on the lamella thickness. Indeed, the aSk size increases by one order of magnitude from ≈ 128 nm to nearly $1.2 \mu\text{m}$ as the lamella thickness is varied from 142 nm to $\approx 4.2 \mu\text{m}$. The aSk size and helix period are found to be close to one another for the same lamella thickness (see Figure S3, Supporting Information).

For the thinner wedge sample that is measured by LTEM, one can see from Figure 1 that the antiskyrmions appear at the thinner side first under a smaller field and then appear at the thicker side under a larger field. However, the result is opposite for the thicker wedge sample that is measured by MFM in Figure 3. These differences could arise from the different field tilting angles used in the measurements of these images, which is $\approx 0^\circ$ for LTEM and $\approx 30^\circ$ for MFM, or possibly from the different shapes (inclination angles) of the wedges used. However, the measured helix period and aSk size are hardly influenced by the measurement protocols or the wedge shapes.

In order to study the large-scale magnetic textures that we find in thicker lamellae, MFM measurements were performed in the presence of an in-plane magnetic field applied along distinct directions. We first apply an in-plane field of $H = 1.5$ T along the direction $\varphi_H = 0^\circ$ to polarize the magnetization along $+x$, after which H is gradually decreased to 0.3 T. Then we observe that the magnetic texture has become triangularly shaped throughout much of the lamella (L3), as shown in Figure 4a. All the triangles point along the same direction: we

note that their size corresponds well to that of the original helix or aSk. Similar measurements for $\varphi_H = -90^\circ$, $\varphi_H = -180^\circ$, and $\varphi_H = -270^\circ$ were performed, as shown in Figure 4b–d. In each case similar triangular magnetic textures are found but, most interestingly, they clearly point along different directions.

Let us consider the evolution of an aSk structure under an in-plane field applied along $\langle 100 \rangle$. Along these directions, the boundaries are Bloch like so that one expects that the area of the regions of in-plane magnetization within these boundaries pointing along the field direction will increase, whereas those pointing in the opposite direction will decrease in area. This will give rise to a distorted triangularly shaped object that is observed. Furthermore, when the field direction is rotated in a clockwise fashion, we find experimentally that the triangular shape rather rotates in the counterclockwise direction. This is in agreement with the expected distortion of the aSk structure under an in-plane magnetic field, as illustrated schematically in Figure 4e. Note that for a skyrmion structure, whether Bloch or Néel, the distorted spin textures would rotate in the same direction as the field. Another explanation for the triangularly shaped magnetic structures, which has recently been proposed, are “nontopological bubbles,”^[11] in which half of the object is a square antiskyrmion and the other half is a round skyrmion. This “nontopological bubble” will also rotate in the opposite direction to the in-plane magnetic field. Since MFM cannot readily distinguish between an antiskyrmion and such a “nontopological bubble,” the detailed magnetic structures, especially in the large thickness regime, require further studies. There is, however, strong experimental evidence, by comparing Figure 3 with Figure 4, that the round shape magnetic object in Figure 3 is indeed an antiskyrmion.

In order to probe the microscopic mechanism of the thickness dependence of the aSk size and helix period, an analytic calculation was carried out for a model D_{2d} system. The DMI energy density in a D_{2d} material is given by

$$E_{\text{DMI}} = D \left(m_x \frac{\partial m_z}{\partial y} + m_y \frac{\partial m_z}{\partial x} - m_z \frac{\partial m_x}{\partial y} - m_z \frac{\partial m_y}{\partial x} \right) \quad (1)$$

where D is the DMI strength (J m^{-2}).

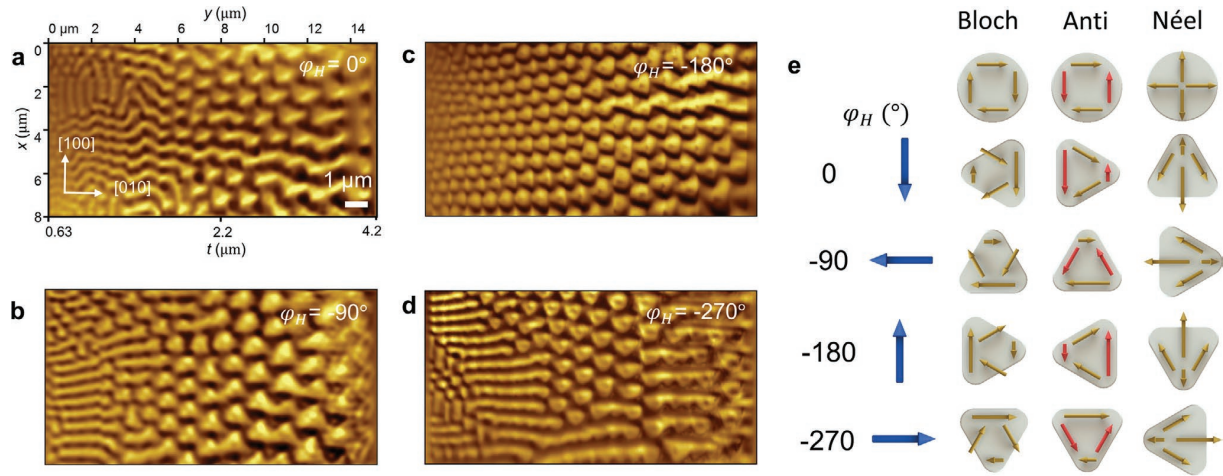


Figure 4. MFM images for different in-plane magnetic field directions. a–d) The field direction is $\varphi_H = 0^\circ, -90^\circ, -180^\circ,$ and $-270^\circ,$ respectively, and the field amplitude in each case is 0.3 T. e) Schematic spin textures for Bloch, antiskyrmion, and Néel skyrmion for different in-plane field directions. The blue arrow indicates the field direction. The red and yellow arrows indicate the in-plane magnetization. For the antiskyrmion, the arrows indicate the in-plane magnetization only for the Bloch regions of the boundary.

As shown in **Figure 5a**, we assume that the helix magnetization changes only along the helix direction with a Bloch sine function and a period of λ . The model assumes a slab of infinite extent in the xy plane and a finite thickness t along z . We assume the magnetization is constant along z which is a good approximation in a D_{2d} system where the DMI has no component along z . We note that this same assumption may not be appropriate for B20 systems in which the DMI imposes a twisted structure along z . The resultant total energy density is given by

$$E_{\text{Tot}} = E_{\text{Exc}} + E_{\text{DMI}} + E_{\text{Ani}} + E_{\text{Dip}}$$

$$= \frac{4\pi^2 A}{\lambda^2} - \frac{2\pi |D|}{\lambda} + \frac{K}{2} + \frac{\mu_0 M_s^2 \lambda}{8\pi t} \left(1 - e^{-\frac{2\pi t}{\lambda}} \right) \quad (2)$$

where A is the exchange stiffness (J m^{-1}), K is the anisotropy energy (J m^{-3}), E_{Exc} is the volume exchange energy (J m^{-3}), E_{DMI} is the volume DMI energy, E_{Ani} is the volume magnetic anisotropy energy, E_{Dip} is the volume magnetic dipolar energy, and E_{Tot} is the volume total energy. Since the exchange interaction, DMI and anisotropy in this system are of bulk origin, there are no thickness dependent prefactors in the energy functionals. The DMI energy term does not depend on the helix/cycloid propagation direction.^[12] The detailed calculations are summarized in the Supporting Information. Most importantly the long-range magnetostatic energy E_{Dip} can be given as an exact analytical expression. Atomistic numerical calculations were also carried out which agree well with this expression (see Supporting Information).

The dipolar energy as a function of helix period for various t are plotted in **Figure 5b**. When the film thickness is very small ($t \ll \lambda$), E_{Dip} can be simplified as $E_{\text{Dip}} = \frac{\mu_0 M_s^2}{4} \left(1 - \frac{\pi t}{\lambda} \right)$, so that E_{Dip} varies little in this thickness range. Similarly, when the film thickness is very large ($t \gg \lambda$), E_{Dip} is given by

$E_{\text{Dip}} = \frac{\mu_0 M_s^2 \lambda}{8\pi t}$, which has a linear dependence on λ with a very small slope. In these two regimes, the dipolar energy has a weak dependence on λ , as shown in **Figure 5b** for $t = 1$ nm and $t = 2500$ nm. However, for intermediate thicknesses (e.g., $t = 200$ nm), E_{Dip} changes significantly on the order of $\frac{\mu_0 M_s^2}{4}$ for the λ of interest.

The helix period corresponds to that which minimizes E_{Tot} . The calculated values of λ are summarized in **Figure 5c,d** for various ranges of model parameters. In **Figure 5c** the thickness and DMI strength dependent λ are shown as a colormap for constant A and M_s , whereas the thickness and M_s dependent λ are shown in **Figure 5d** for constant A and D . As shown in **Figure 5c**, when the DMI is very strong, λ is determined by $\frac{4\pi A}{|D|}$. When the DMI strength is weaker, λ drops rapidly to a minimum value as t is increased and then slowly increases back to $\frac{4\pi A}{|D|}$ for very thick layers. As shown in **Figure 5d**, when M_s is increased, λ shrinks.

The dipole energy is dominantly located at the surfaces of the lamella except for very thin t . As shown in **Figures S10** and **S11** of the Supporting Information, E_{Dip} is greatest at the surfaces, decaying exponentially into the interior of the lamella with a characteristic length-scale that is set by λ . Thus, in the limit of large t , the helix wavelength is no longer influenced by the dipole energy but is rather determined by the ratio of the Heisenberg and DMI energies. However, for the range of t of interest here the dipole energy strongly influences λ because, in very simplistic terms, the twisted helical structure reduces the dipole charge at the top and bottom surfaces. Since the total dipolar energy decreases, in this range, as $\approx 1/t$, thus λ monotonically increases as t is increased, thereby accounting for our experimental observation that λ approximately linearly increases with thickness. In **Figure S13** of the Supporting Information a comparison between our experimental results and the model discussed above is made. Qualitatively the model

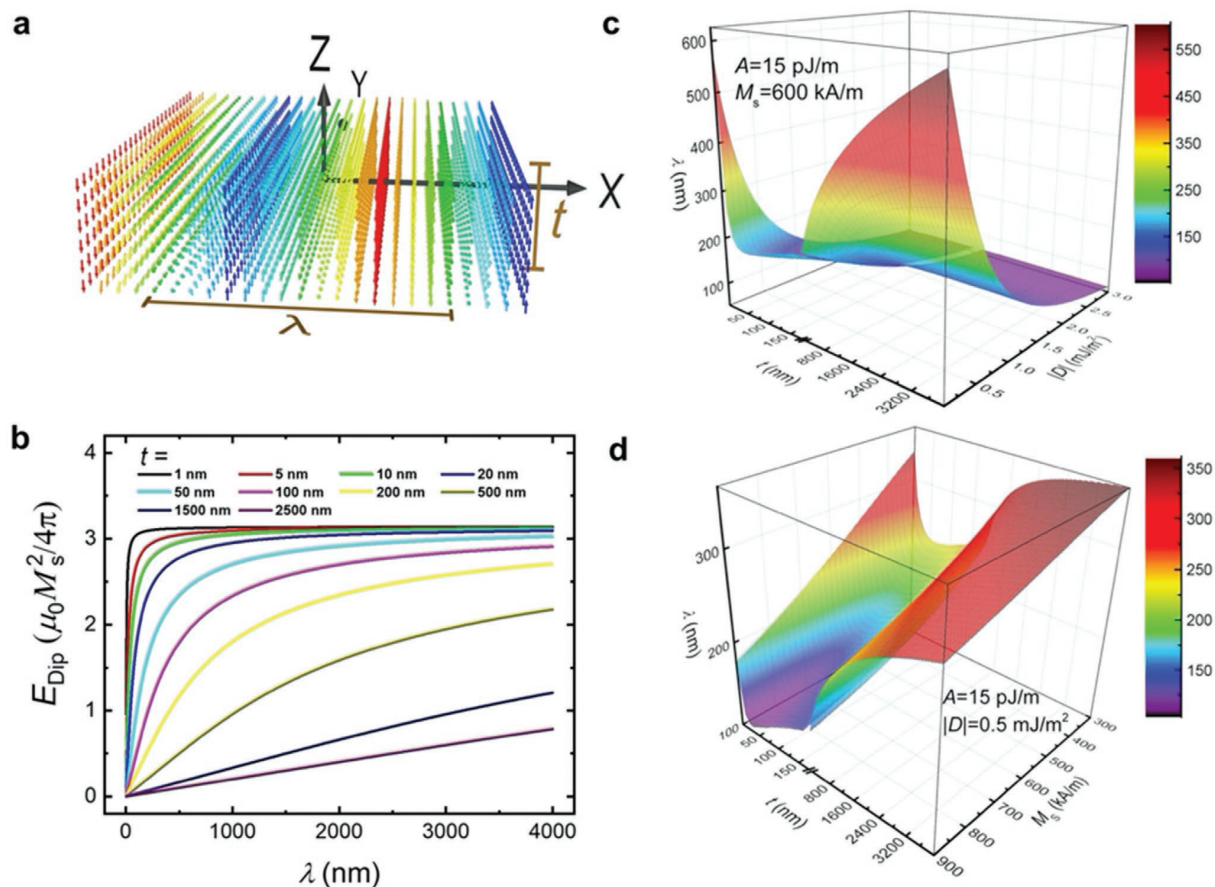


Figure 5. Model calculation for helix structure in D_{2d} system versus thickness. a) Schematic diagram of magnetic helical structure in a D_{2d} system with a helical period of λ and a thickness of t . b) Magnetodipolar energy per unit volume as a function of λ at various t . c) 3D colormap of λ versus t and M_s . d) 3D colormap of λ versus t and $|D|$.

accounts well for the observed trend of increasing λ with thickness. But it is difficult to find within the limitations of our model an exact agreement. We attribute this to deviations from the assumed pure helical Bloch-like form of the magnetic structure throughout the thickness. Our MFM data show that the helix structure is nearly sinusoidal and, since the magnitude of the MFM signal increases linearly with thickness, that the helix exists throughout the thickness. Nevertheless, there can clearly be deviations from this simple structure due to the complex interplay between all the relevant energy terms including the dipolar energy.

The calculation of the magnetodipolar interaction for the aSk phase is much more complicated and needs further theoretical studies. However, since, as shown in our experiments (Figures 2g and 3e), the helix period and aSk size are similar to each other, it is reasonable to assume that the same mechanism, i.e., the thickness dependence of the dipolar energy, accounts for the size variation of the aSk, as well as the helix period.

The thickness dependent behavior of the characteristic size of the spin texture reported in this work is distinct from other material systems due to important differences in the underlying

physical mechanisms. In magnetic bubble systems,^[8] the magnetic structure is achiral since there is no DMI interaction. For a given thickness, the size of the bubble is not fixed and can vary strongly, and, moreover, has a significant dependence on the external magnetic field. Recently, our group reported the experimental discovery of Néel skyrmions in lamellae formed from PtMnGa which has a C_{3v} structure.^[13] There, the Néel skyrmion size was also found to have a large thickness dependence. However, the width of the boundary of the Néel skyrmion is small compared to the size of the object itself, so that this system is more akin to conventional magnetic “bubbles.” In an interfacial DMI system,^[14] although it has been reported theoretically that dipolar interactions could play some role,^[15] the effective strength of the DMI decreases with magnetic layer thickness, so limiting these systems to the nanometer thickness range.

In B20 bulk materials^[5–7] the DMI has nonzero components along all three spatial directions, which is distinct from the D_{2d} system where the DMI is zero along the [001] direction. Thus, skyrmion tubes in a B20 material will have an additional twist in their magnetic structure along the tube direction. Such a twisted structure might weaken the contribution of the dipolar

interaction, thus resulting in a weak thickness dependence of the skyrmion size. Another type of twisted magnetic structure is a “Néel cap” in magnetic multilayer systems^[16] or a horizontal Bloch line,^[17] but these structures are induced by dipolar effects at the surface, and will be less influential than the twisted structures induced by DMI. Nevertheless, they may account for small differences between our experiments and model.

Thus, the D_{2d} antiskyrmion system is the only material system to date in which volume DMI and dipolar interactions together play an important role. This unique property ensures the stability of spin textures in this system over a very extended thickness range and their large size tunability. At the same time this competition between the D_{2d} volume DMI and dipolar interactions can lead to the formation of metastable elliptical Bloch skyrmions.^[11,18]

In conclusion, our work shows how important is the role of the magnetodipolar interaction in influencing the size scale of noncollinear spin textures, depending on the symmetry of the host material. The wide range of tunability of the size of the antiskyrmion and corresponding helical spin textures in the D_{2d} system makes these materials particularly interesting for applications. For example, in racetrack memory devices^[19] the size of antiskyrmions could be locally adjusted to make them easier to read and to create by adjusting the thickness of the racetrack spatially. Our results also clearly show how the size of antiskyrmions can be tuned by manipulating their magnetization rather than the DMI. For example, by chemical doping, by using materials with a strong temperature dependence of magnetization, or by the use of ferrimagnets or synthetic antiferromagnets, thereby opening up a new direction in the field of chiraltronics.

Supporting Information

Supporting Information is available from the Wiley Online Library or from the author.

Acknowledgements

T.M., A.K.S., R.S., and A.K.S. contributed equally to this work. This project received funding from the European Research Council (ERC) under the European Union's Horizon 2020 research and innovation program (Grant Agreement No. 670166) and the Deutsche Forschungsgemeinschaft (DFG, German Research Foundation) – Project No. 403505322.

Conflict of Interest

The authors declare no conflict of interest.

Keywords

antiskyrmion, D_{2d} symmetry, Heusler compound, Lorentz transmission electron microscopy, spintronics

Received: March 24, 2020

Revised: April 27, 2020

Published online: June 2, 2020

- [1] a) S. Mühlbauer, B. Binz, F. Jonietz, C. Pfleiderer, A. Rosch, A. Neubauer, R. Georgii, P. Böni, *Science* **2009**, 323, 915; b) U. K. Röbner, A. N. Bogdanov, C. Pfleiderer, *Nature* **2006**, 442, 797; c) X. Z. Yu, Y. Onose, N. Kanazawa, J. H. Park, J. H. Han, Y. Matsui, N. Nagaosa, Y. Tokura, *Nature* **2010**, 465, 901; d) A. Fert, V. Cros, J. Sampaio, *Nat. Nanotechnol.* **2013**, 8, 152; e) N. Nagaosa, Y. Tokura, *Nat. Nanotechnol.* **2013**, 8, 899; f) W. Koshibae, N. Nagaosa, *Nat. Commun.* **2016**, 7, 10542; g) F. Jonietz, S. Mühlbauer, C. Pfleiderer, A. Neubauer, W. Münzer, A. Bauer, T. Adams, R. Georgii, P. Böni, R. A. Duine, *Science* **2010**, 330, 1648; h) A. Soumyanarayanan, M. Raju, A. G. Oyarce, A. K. Tan, M.-Y. Im, A. P. Petrović, P. Ho, K. Khoo, M. Tran, C. Gan, *Nat. Mater.* **2017**, 16, 898; i) N. Romming, C. Hanneken, M. Menzel, J. E. Bickel, U. Wolter, K. von Bergmann, A. Kubetzka, R. Wiesendanger, *Science* **2013**, 341, 636; j) A. N. Bogdanov, U. K. Röbner, M. Wolf, K.-H. Müller, *Phys. Rev. B* **2002**, 66, 214410.
- [2] A. K. Nayak, V. Kumar, T. Ma, P. Werner, E. Pippel, R. Sahoo, F. Damay, U. K. Röbner, C. Felser, S. S. P. Parkin, *Nature* **2017**, 548, 561.
- [3] R. Saha, A. K. Srivastava, T. Ma, J. Jena, P. Werner, V. Kumar, C. Felser, S. S. P. Parkin, *Nat. Commun.* **2019**, 10, 5305.
- [4] a) I. Dzyaloshinsky, *J. Phys. Chem. Solids* **1958**, 4, 241; b) T. Moriya, *Phys. Rev.* **1960**, 120, 91; c) A. N. Bogdanov, D. A. Yablonskii, *Zh. Eksp. Teor. Fiz.* **1989**, 95, 182.
- [5] a) X. Z. Yu, N. Kanazawa, Y. Onose, K. Kimoto, W. Z. Zhang, S. Ishiwata, Y. Matsui, Y. Tokura, *Nat. Mater.* **2011**, 10, 106; b) F. Zheng, F. N. Rybakov, A. B. Borisov, D. Song, S. Wang, Z.-A. Li, H. Du, N. S. Kiselev, J. Caron, A. Kovács, *Nat. Nanotechnol.* **2018**, 13, 451.
- [6] K. Shibata, X. Z. Yu, T. Hara, D. Morikawa, N. Kanazawa, K. Kimoto, S. Ishiwata, Y. Matsui, Y. Tokura, *Nat. Nanotechnol.* **2013**, 8, 723.
- [7] H. S. Park, X. Yu, S. Aizawa, T. Tanigaki, T. Akashi, Y. Takahashi, T. Matsuda, N. Kanazawa, Y. Onose, D. Shindo, *Nat. Nanotechnol.* **2014**, 9, 337.
- [8] a) Z. Málek, V. Kamberský, *Czech. J. Phys.* **1958**, 8, 416; b) J. Cape, G. Lehman, *J. Appl. Phys.* **1971**, 42, 5732; c) P. Grundy, S. Herd, *Phys. Status Solidi A* **1973**, 20, 295.
- [9] a) X. Z. Yu, Y. Tokunaga, Y. Kaneko, W. Zhang, K. Kimoto, Y. Matsui, Y. Taguchi, Y. Tokura, *Nat. Commun.* **2014**, 5, 3198; b) W. Wang, Y. Zhang, G. Xu, L. Peng, B. Ding, Y. Wang, Z. Hou, X. Zhang, X. Li, E. Liu, *Adv. Mater.* **2016**, 28, 6887; c) X. Z. Yu, M. Mostovoy, Y. Tokunaga, W. Zhang, K. Kimoto, Y. Matsui, Y. Kaneko, N. Nagaosa, Y. Tokura, *Proc. Natl. Acad. Sci. USA* **2012**, 109, 8856.
- [10] T. Malis, S. Cheng, R. Egerton, *J. Electron Microsc. Tech.* **1988**, 8, 193.
- [11] L. Peng, R. Takagi, W. Koshibae, K. Shibata, K. Nakajima, T.-H. Arima, N. Nagaosa, S. Seki, X. Z. Yu, Y. Tokura, *Nat. Nanotechnol.* **2020**, 15, 181.
- [12] L. Camosi, N. Rougemaille, O. Fruchart, J. Vogel, S. Rohart, *Phys. Rev. B* **2018**, 97, 134404.
- [13] A. K. Srivastava, P. Devi, A. K. Sharma, T. Ma, H. Deniz, H. L. Meyerheim, C. Felser, S. S. P. Parkin, *Adv. Mater.* **2020**, 32, 1904327.
- [14] a) G. Chen, J. Zhu, A. Quesada, J. Li, A. N'Diaye, Y. Huo, T. Ma, Y. Chen, H. Kwon, C. Won, *Phys. Rev. Lett.* **2013**, 110, 177204; b) G. Chen, T. Ma, A. T. N'Diaye, H. Kwon, C. Won, Y. Wu, A. K. Schmid, *Nat. Commun.* **2013**, 4, 2671.
- [15] a) I. Lemesch, F. Büttner, G. S. Beach, *Phys. Rev. B* **2017**, 95, 174423; b) F. Büttner, I. Lemesch, G. S. Beach, *Sci. Rep.* **2018**, 8, 4464.
- [16] a) W. Legrand, N. Ronceray, N. Reyren, D. Maccariello, V. Cros, A. Fert, *Phys. Rev. Appl.* **2018**, 10, 064042; b) I. Lemesch, G. S. Beach, *Phys. Rev. B* **2018**, 98, 104402; c) S. Montoya, S. Couture, J. Chess, J. Lee, N. Kent, D. Henze, S. Sinha, M.-Y. Im, S. Kevan, P. Fischer, *Phys. Rev. B* **2017**, 95, 024415.
- [17] A. P. Malozemoff, J. C. Slonczewski, *Magnetic Domain Walls in Bubble Materials*, Academic Press, New York **1979**.
- [18] J. Jena, B. Göbel, T. Ma, V. Kumar, R. Saha, I. Mertig, C. Felser, S. S. Parkin, *Nat. Commun.* **2020**, 11, 1115.
- [19] a) S. S. P. Parkin, M. Hayashi, L. Thomas, *Science* **2008**, 320, 190; b) S. S. P. Parkin, S.-H. Yang, *Nat. Nanotechnol.* **2015**, 10, 195.

ADVANCED MATERIALS

Supporting Information

for *Adv. Mater.*, DOI: 10.1002/adma.202002043

Tunable Magnetic Antiskyrmion Size and Helical Period from
Nanometers to Micrometers in a D_{2d} Heusler Compound

*Tianping Ma, Ankit K. Sharma, Rana Saha, Abhay K.
Srivastava, Peter Werner, Praveen Vir, Vivek Kumar, Claudia
Felser, and Stuart S. P. Parkin**

Supporting Information

Tunable Magnetic Antiskyrmion Size and Helical Period from Nanometers to Micrometers in a D_{2d} Heusler compound

*Tianping Ma, Ankit K. Sharma, Rana Saha, Abhay K. Srivastava, Peter Werner, Praveen Vir, Vivek Kumar, Claudia Felser and Stuart S.P. Parkin**

Synthesis of single crystal

Single crystals of Mn_{1.4}PtSn were prepared using a flux growth method using tin as the flux. High purity elements of manganese and platinum in a 3:1 atomic ratio with a weight of 0.75 gram were loaded into an alumina crucible with approximately 10 g tin. The alumina crucible was sealed in a quartz ampule under 0.2 bar argon pressure. The quartz ampule was then placed in a box furnace and heated at 1050 °C for 24 h in order to achieve a homogeneous solution. It was then cooled quickly to 650 °C and then slowly cooled to 450 °C where it was kept for a few hours to crystallize more of the desired compound. After growth, the flux with excess Mn was removed by centrifugation at high temperatures (400-450 °C).

Lamellae preparation by focused ion beam (FIB)

Several lamellae of uniform thickness or with a wedge profile were prepared from the same single crystal of Mn_{1.4}PtSn using Ga⁺ Focused Ion Beam (FIB) milling [TESCAN GAIA3 operating at 30 keV ion-beam energy]. Lamellae were taken out of the bulk single crystal using standard lift-out procedures and transferred to a copper grid for TEM observations. The lamellae were then thinned down to the desired shape and thickness. Finally, both faces of each lamella were polished with

lower Ga ion-beam energies (5 keV) to reduce the thickness of any damaged surface layers that might result from any Ga ion implantation. For MFM measurements, the lamella was transferred from the copper grid to a gold pad that had been deposited on a silicon substrate and attached to the gold pad by platinum deposited using the FIB. After this process the lamella was again polished using a low energy Ga ion beam.

Transmission electron microscopy (TEM)

An aberration-corrected high-resolution transmission electron microscope [FEI TITAN 80-300] operated at an acceleration voltage of 300 keV was used for the TEM and LTEM studies. A double tilt sample holder was used. A magnetic field along the microscope column, varying from 0 to 416 mT, was applied by adjusting the current in the objective lens. The thickness of the TEM lamella was determined by EELS using a log-ratio formula to determine the local thickness, $t = \lambda \ln (I_t/I_0)$, where λ is the total inelastic mean free path of electrons, and I_t and I_0 are the total and zero-loss areas under the EELS spectrum, respectively. A typical thickness error determined by the above mentioned log-ratio method is $\sim 10\%$. The EELS was carried out on the lamella slightly tilted from the zone axis to avoid channeling effects.

Magnetic force microscopy (MFM)

MFM experiments are carried out in a variable temperature Attocube system equipped with a 2D vector superconducting magnet, which can generate a magnetic field of 3 T in plane and 9 T perpendicular to the sample surface. A magnetic tip from Nanosensors (PPP-LM-MFMR) was used. The soft coating on the magnetic tip ensures a low disturbance of the magnetic samples so that a higher spatial resolution (~ 20 nm) could be achieved. The tip was initialized with its moment along a negative z direction by a small permanent magnet. A dual scanning technique to obtain

simultaneous topographic and magnetic contrast was used. The topographic measurement result was used to calibrate the sample thickness which agreed well with scanning electron microscopy images. The tip first interacts with the sample in the tapping mode to acquire the surface topography and is then lifted to 80 nm above the sample surface to record the magnetic texture, where a phase detection technique is used.

Effect of magnetic field on the helical phase and anti-skyrmion phase in a wedge-shaped lamella of $M_{1.4}PtSn$ at 300K

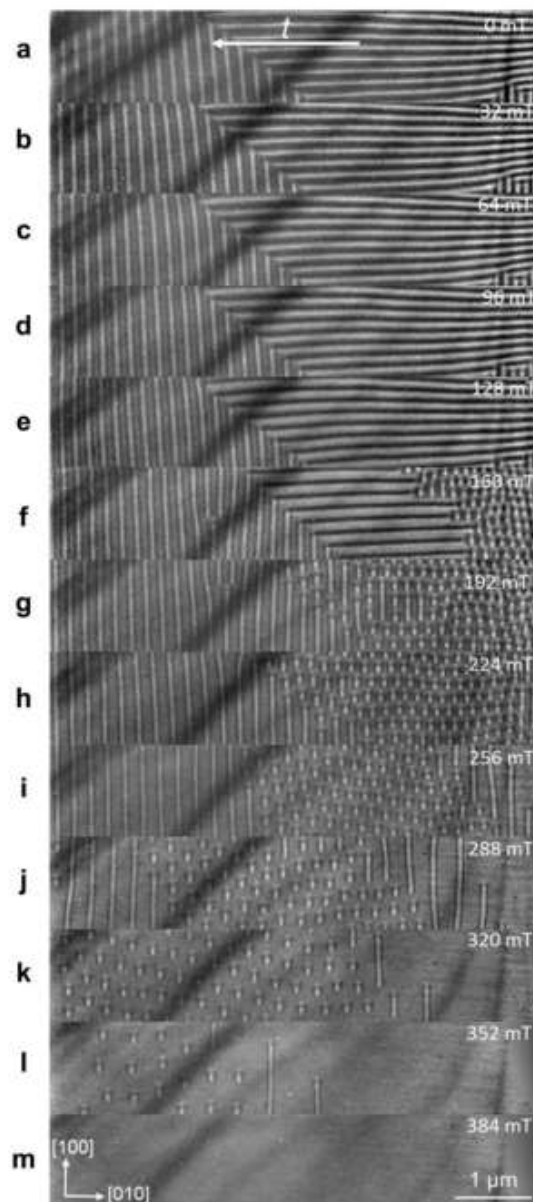


Figure S1. (a-m) Lorentz transmission electron microscopy (LTEM) images at different magnetic fields showing the variation of helical period and size of aSk across the wedge, where the thickness decreases from left to right in the image.

At zero magnetic field the helical phase appears throughout the lamella (L2), where the helix propagates along either [100] or [010]. The helical phase exists in the field range from 0 to 128 mT for all thicknesses. In the field range of 160-224 mT the helical phase coexists with the aSk phase as shown in f-h. When the magnetic field is further increased, the field polarized phase eventually appears. The aSk phase first appears in the thinner part at 160 mT, then, with increasing field, the aSk phase gradually appears in the thicker part, while the thinner part transforms to the fully field-polarized state. Finally, at 384 mT the field-polarized state appears throughout the wedge. In the images **h-i**, the helical phase reappears in the thinner region at higher fields because of the tilting protocol (mentioned in the main text) that was employed to stabilize the aSk phase.

Selected area electron diffraction (SAED) pattern of $\text{Mn}_{1.4}\text{PtSn}$

SAED pattern along the [001] zone axis for L2. The pattern is consistent with the $I\bar{4}2m$ tetragonal symmetry (D_{2d}) of an inverse tetragonal Heusler.

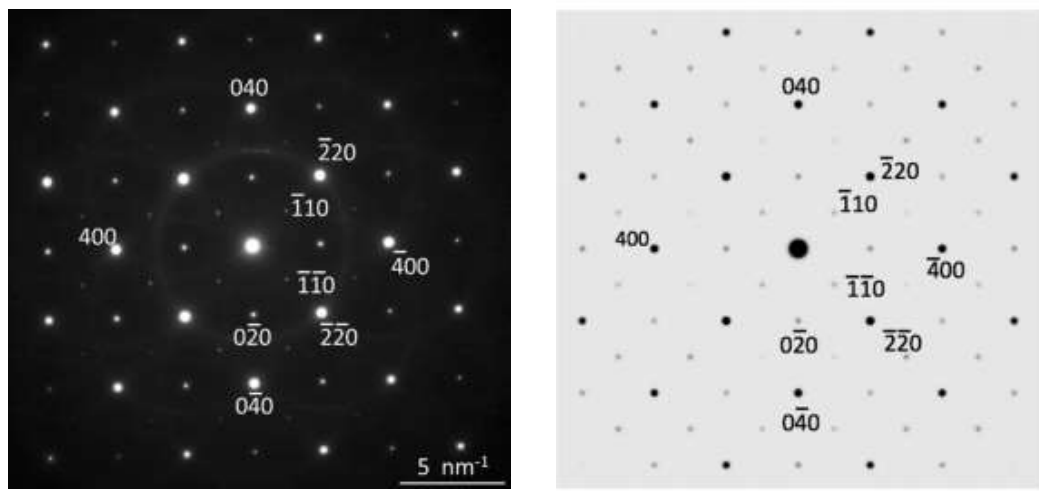


Figure S2. SAED pattern from the [001] oriented wedge L2. **a)** experiment and **b)** simulation.

Comparison of helix period and anti-skyrmion size

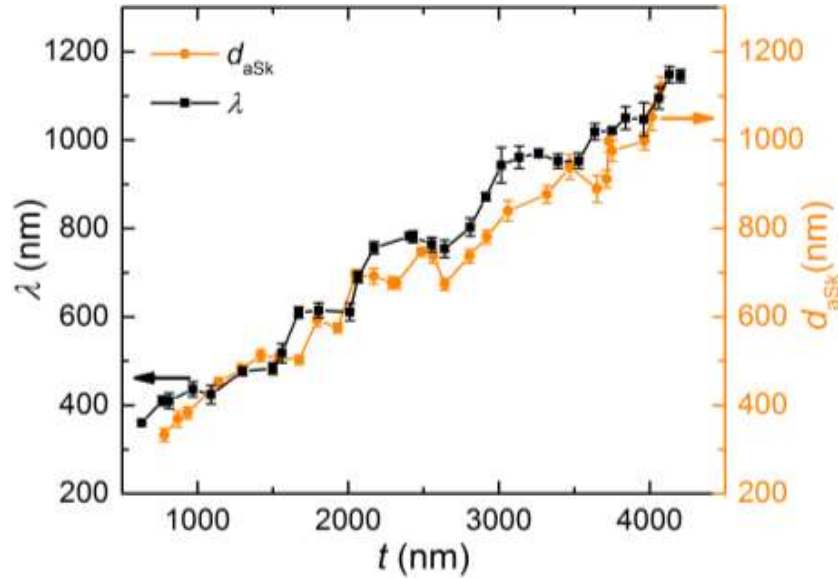


Figure S3. Comparison of helical period (black symbols and line) and anti-skyrmion size (orange symbols and line) for wedge L3: data is from Figure 2g (black data) and Figure 3e (black data), respectively, of the main manuscript.

Method to deduce anti-skyrmion size from LTEM and MFM images

The LTEM/MFM images were analyzed as follows: after loading the image into a graphical data analysis program, the center position of the first aSk and the boundary of the same aSk were found manually by clicking on these positions. The size of this aSk was thus determined according to the nanometer to pixel ratio. This same two-click procedure is repeated for all aSk. As shown in Figure S4, the aSk are then displayed as red circles. The corresponding thickness for each aSk are determined via the AFM topographic maps. The error bar of the aSk size is determined by the standard deviation of aSk at around the same thickness.

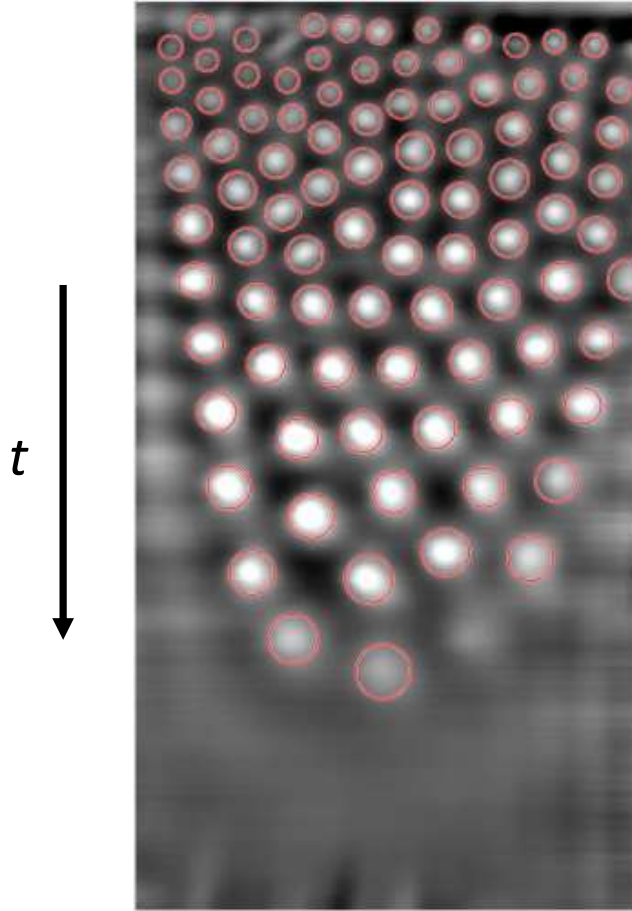


Figure S4. Analysis of anti-skyrmion size: A MFM image of the anti-skyrmion phase for a magnetic field of 480 mT for L3. The red circles represent the position and size of each aSk.

MFM measurements as a function of field and out of plane tilt angle

The helical phase transforms into an anti-skyrmion phase in the presence of a large enough out of plane magnetic field. However, the tilting angle of the field plays a crucial role in stabilizing an aSk phase throughout the lamella. When the field is applied along the z-axis (0°) the helix region shrinks and the aSk phase stabilizes only in a smaller region of the lamella as shown in Figure S5a. As the tilt angle is increased to 10° , the aSk phase region extends to a larger area of the lamella as shown in Figure S5b. The field tilting angle that stabilized the aSk phase for the widest range of thickness of the lamella (L3) was found to be $\sim 30^\circ$, as shown in Figure 3 of the main manuscript. At a tilting angle of 45° , the aSk phase is again limited to a small region of the lamella, as shown in

Figure S5c. Regions of the lamella which are fully polarized at the thicker end of the wedge are not fully shown.

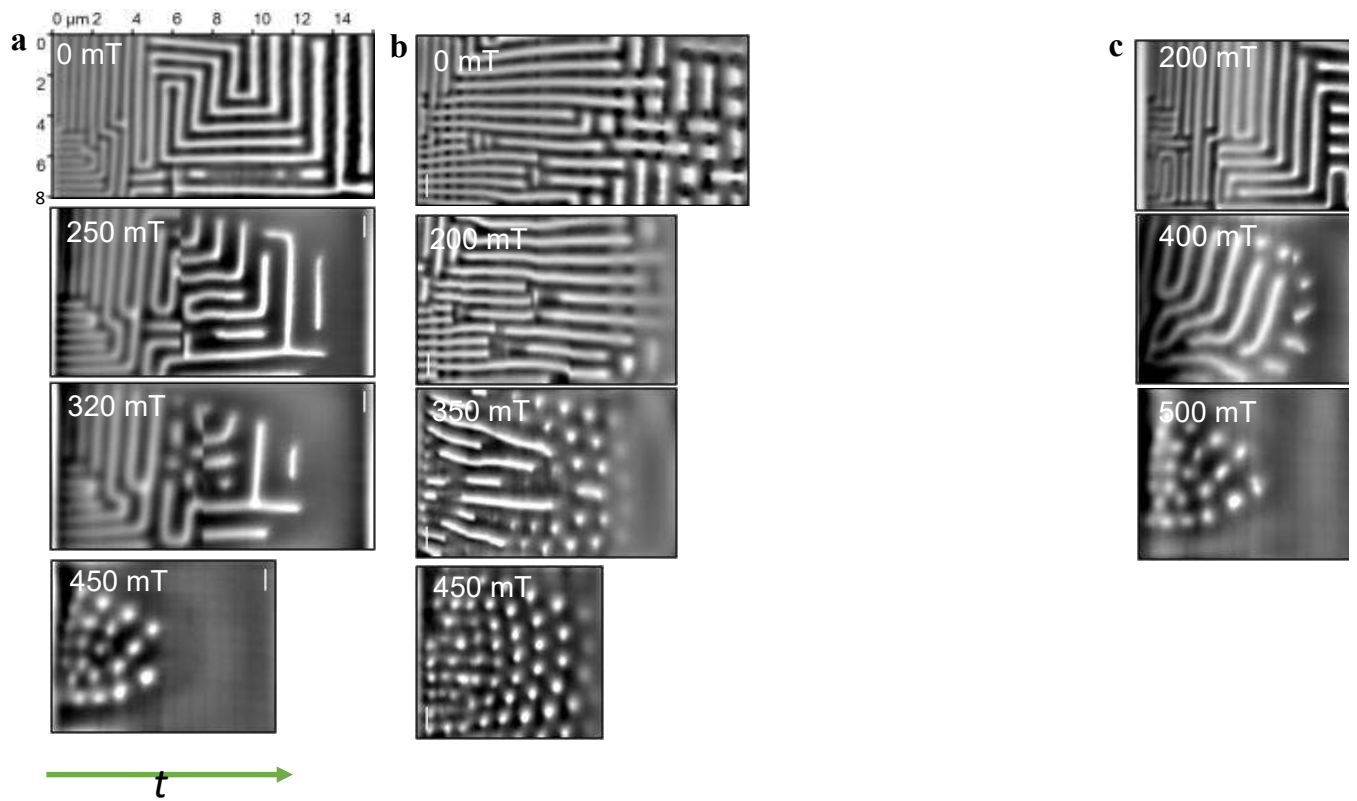


Figure S5. (a-c), MFM images show the evolution of the helical state into the anti-skyrmion phase under the application of a magnetic field applied at tilting angles of **a** 0°, **b** 10° and **c** 45°. The thickness of lamella increases from left to right.

MFM measurements of magnetic triangle structure as a function of in-plane field

Starting from a helix state with mixed [100] and [010] orientation under zero field (Figure S6a), the in-plane magnetic field is gradually increased along $\varphi_H = 0^\circ$. The MFM results for fields from 100 mT to 700 mT are shown in Figure S6b-f. When the field reaches 200 mT, the triangularly shaped magnetic structures start to appear. At 700 mT the MFM contrast disappears indicating that all the magnetization is aligned with the in-plane magnetic field.

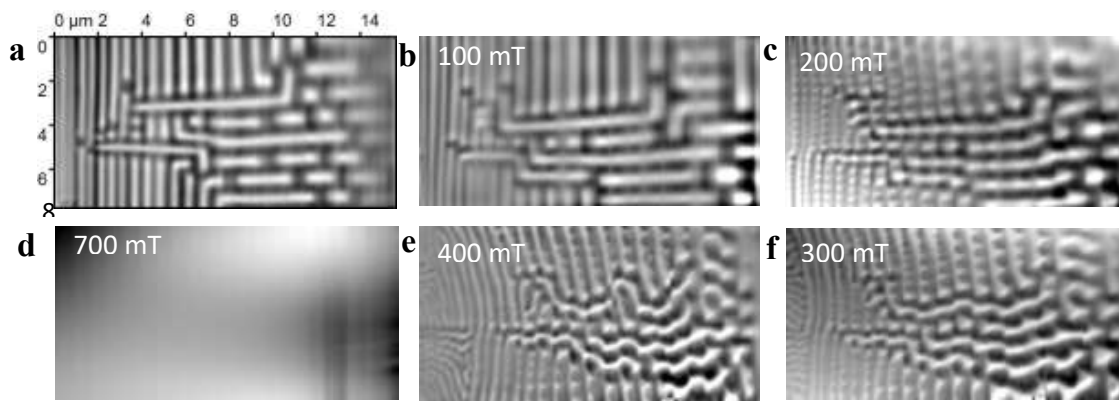


Figure S6. (a-f), MFM images show the evolution of the helical state into the triangular phase and eventually into the field polarized state under the application of an in-plane magnetic field applied at $\varphi_H = 0^\circ$.

Model and calculation for the magnetic dipolar interaction

A. Analytical expression of E_{Dip} for a Bloch helix

As described in the main manuscript and shown in Figure 5a of the main text. The magnetization

$\vec{M} = (M_x, M_y, M_z)$ is described as:

$$\begin{cases} M_x(x, y, z) = 0 \\ M_y(x, y, z) = M_s \sin\left(\frac{x}{\lambda} 2\pi\right) \\ M_z(x, y, z) = M_s \cos\left(\frac{x}{\lambda} 2\pi\right) \end{cases} \quad \text{for } -\frac{L_z}{2} < z < \frac{L_z}{2} \quad (\text{S1})$$

$$\begin{cases} M_x(x, y, z) = 0 \\ M_y(x, y, z) = 0 \\ M_z(x, y, z) = 0 \end{cases} \quad \text{for } z < -\frac{L_z}{2} \text{ or } z > \frac{L_z}{2} \quad (\text{S2})$$

The volume magneto-dipolar energy E_{Dip} is calculated from the expression:

$$E_{Dip} = -\frac{\mu_0}{2V} \int \vec{M} \cdot \vec{H} d\tau \quad (\text{S3})$$

where V is the volume.

In order to calculate the dipolar energy, we need to calculate the field $\vec{H} = -\nabla U$

(S4)

where U is a scalar potential and should satisfy the following formulae:^[1]

$$\nabla^2 U_{in} = \vec{\nabla} \cdot \vec{M} \quad \text{inside the sample body} \quad (\text{S5})$$

$$\nabla^2 U_{out} = 0 \quad \text{outside the sample body} \quad (\text{S6})$$

$$U_{in} = U_{out} \quad \text{on the boundary} \quad (\text{S7})$$

$$\frac{\partial U_{in}}{\partial n} - \frac{\partial U_{out}}{\partial n} = \vec{M} \cdot \vec{n} \quad \text{on the boundary, where } \vec{n} \text{ is the unit vector normal to the surface.} \quad (\text{S8})$$

U is calculated from^[1]:

$$U(\vec{r}) = \frac{1}{4\pi} \left(-\int \frac{\vec{\nabla}' \cdot \vec{M}(\vec{r}')}{|\vec{r} - \vec{r}'|} d\tau' + \int \frac{\vec{n} \cdot \vec{M}(\vec{r}')}{|\vec{r} - \vec{r}'|} dS' \right) \quad (\text{S9})$$

where $\overrightarrow{\nabla'}$ contains derivatives with respect to the components of $\overrightarrow{r'}$

Substituting Equation S1-S2 into Equation S9 we perform the integration to obtain the analytical expression:

$$U(x, y, z) = \frac{M_s \lambda}{4\pi} \cos\left(\frac{2\pi x}{\lambda}\right) \left(e^{-\frac{2\pi}{\lambda} \left| z - \frac{L_z}{2} \right|} - e^{-\frac{2\pi}{\lambda} \left| z + \frac{L_z}{2} \right|} \right) \quad (\text{S10})$$

We checked that Equation S10 is consistent with Equations S5-S8.

Then the field is calculated from $\vec{H} = -\nabla U$

$$= \left(\frac{M_s}{2} \sin\left(\frac{2\pi x}{\lambda}\right) \left[e^{-\frac{2\pi}{\lambda} \left(\frac{L_z}{2} - z \right)} - e^{-\frac{2\pi}{\lambda} \left(z + \frac{L_z}{2} \right)} \right] \quad 0 \quad -\frac{M_s}{2} \cos\left(\frac{2\pi x}{\lambda}\right) \left[e^{-\frac{2\pi}{\lambda} \left(\frac{L_z}{2} - z \right)} + e^{-\frac{2\pi}{\lambda} \left(z + \frac{L_z}{2} \right)} \right] \right) \quad (\text{S11})$$

Substituting Equations S1-S2, S11 into Equation S3 and performing the integration, we obtain the final result:

$$E_{Dip} = \frac{\mu_0 M_s^2 \lambda}{8\pi L_z} \left(1 - e^{-\frac{2\pi L_z}{\lambda}} \right) \quad (\text{S12})$$

B. Numerical calculation to confirm the validity of E_{Dip}

We perform a numerical calculation to confirm the validity of Equation S12

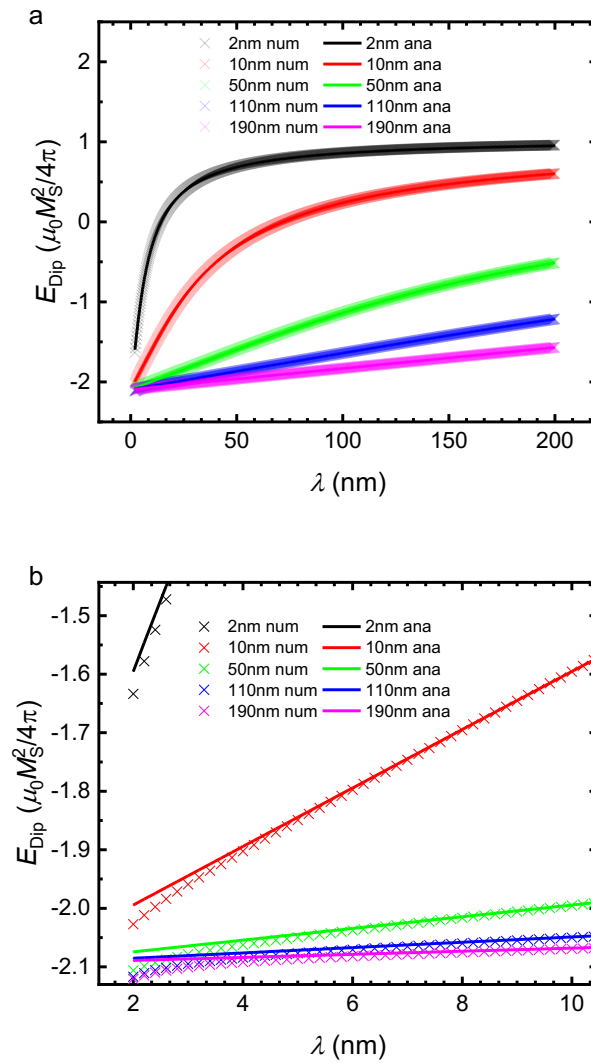
Between two atoms, the dipolar energy is given by

$$E_{Dip,ab} = \frac{\mu_0}{4\pi} \frac{\overrightarrow{S_a} \cdot \overrightarrow{S_b} |\overrightarrow{P_a} - \overrightarrow{P_b}|^2 - 3\overrightarrow{S_a} \cdot (\overrightarrow{P_a} - \overrightarrow{P_b}) \overrightarrow{S_b} \cdot (\overrightarrow{P_a} - \overrightarrow{P_b})}{|\overrightarrow{P_a} - \overrightarrow{P_b}|^5} \quad (\text{S13})$$

where $\overrightarrow{P_a}$ and $\overrightarrow{P_b}$ are the position of two atoms and $\overrightarrow{S_a}$ and $\overrightarrow{S_b}$ are the magnetic moments located at each of these atoms.

The total dipolar energy is calculated by summing up over the pairs of atoms over the sample area using similar numerical methods used in previous work^[2] but expanding this approach to the 3D case. As shown in Figure S7a, an excellent match between the numerical calculation and the analytical formula is found which confirms the validity of the analytical formula we obtained in Equation S12. A constant energy difference between the numerical and analytical results of $\frac{\mu_0 M_s^2}{6}$ is

simply due to the choice of zero-energy which is not important. As shown in Figure S7b-c, tiny differences occur when the helix period or thickness are very small on the order of the lattice constant. Such differences are due to the assumption of continuous change in the analytic method^[1] which is not then satisfied and is not relevant to the experimental region considered in this work.



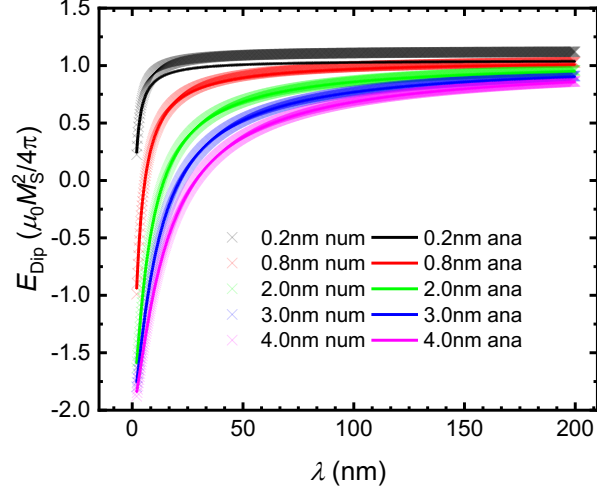


Figure S7. Comparison of results of numerical calculation with those of analytical formula. a) Excellent matching is found. Small differences are shown at very small helix period, **b)** or thickness **c).**

C. Analytical expression of E_{Dip} for other types of Helices, cycloids or geometry in between

Consider the situation of other types of structure: Néel cycloid, or intermediate state between Néel and Bloch.

The magnetization $\vec{M} = (M_x, M_y, M_z)$ is described by:

$$\begin{cases} M_x(x, y, z) = M_s \sin\left(\frac{x}{\lambda} 2\pi\right) \sin(\varphi_0) \\ M_y(x, y, z) = M_s \sin\left(\frac{x}{\lambda} 2\pi\right) \cos(\varphi_0) & \text{for } -\frac{L_z}{2} < z < \frac{L_z}{2} \\ M_z(x, y, z) = M_s \cos\left(\frac{x}{\lambda} 2\pi\right) \end{cases} \quad (\text{S14})$$

$$\begin{cases} M_x(x, y, z) = 0 \\ M_y(x, y, z) = 0 & \text{for } z < -\frac{L_z}{2} \text{ or } z > \frac{L_z}{2} \\ M_z(x, y, z) = 0 \end{cases} \quad (\text{S15})$$

where $\varphi_0 = 0, \pi$ corresponds to a Bloch Helix which propagates along $[100]/[010]$ directions in a D_{2d} system, $\varphi_0 = \frac{\pi}{2}, \frac{3\pi}{2}$ corresponding to a Néel cycloid which propagates along $[110]/[1\bar{1}0]$ directions, other values of φ_0 correspond to the more general propagation direction.

Similar to the discussion above in part a, U is calculated from Equation S9, with the result that:

$$U(x, y, z) =$$

$$\begin{cases} U_1(x, y, z) = \frac{1}{4\pi} \lambda M_s \cos\left(\frac{2\pi x}{\lambda}\right) e^{-\frac{2\pi}{\lambda}z} (e^{\frac{\pi}{\lambda}L_z} - e^{-\frac{\pi}{\lambda}L_z}) (1 - \sin \varphi_0) & z > \frac{L_z}{2} \\ U_2(x, y, z) = \frac{\lambda M_s}{4\pi} \cos\left(\frac{2\pi x}{\lambda}\right) \left[-2 \sin(\varphi_0) + \sin(\varphi_0) e^{-\frac{\pi}{\lambda}L_z} (e^{\frac{2\pi}{\lambda}z} + e^{-\frac{2\pi}{\lambda}z}) + e^{-\frac{\pi}{\lambda}L_z} (e^{\frac{2\pi}{\lambda}z} - e^{-\frac{2\pi}{\lambda}z}) \right] & -\frac{L_z}{2} < z < \frac{L_z}{2} \\ U_3(x, y, z) = \frac{1}{4\pi} \lambda M_s \cos\left(\frac{2\pi x}{\lambda}\right) e^{\frac{2\pi}{\lambda}z} (e^{-\frac{\pi}{\lambda}L_z} - e^{\frac{\pi}{\lambda}L_z}) (1 + \sin \varphi_0) & z < -\frac{L_z}{2} \end{cases} \quad (S16)$$

The following formulae are used:

$$\int_0^{+\infty} \frac{\cos(x)}{\sqrt{x^2+A}} dx = K_0(\sqrt{A}) \quad (S17)$$

where $K_0(x)$ is the modified Bessel function of the second kind, zero order

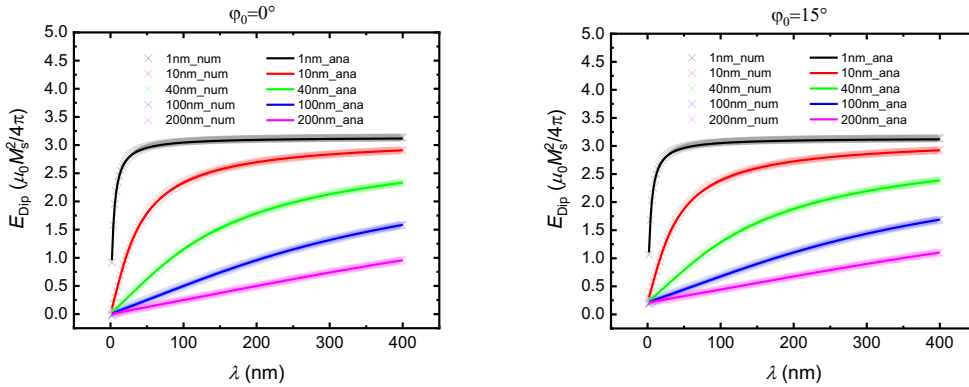
$$\int_0^{+\infty} K_0(|a|\sqrt{x^2+b^2}) dx = \frac{\pi}{2|a|} e^{-|a||b|} \quad (S18)$$

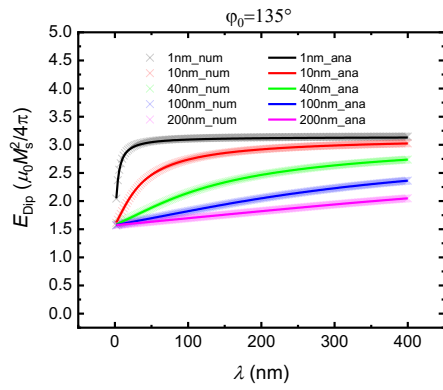
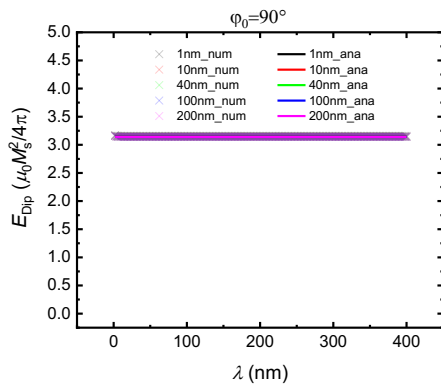
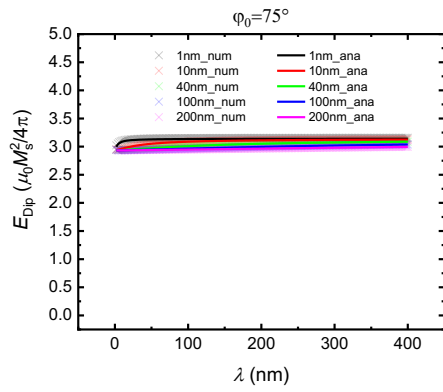
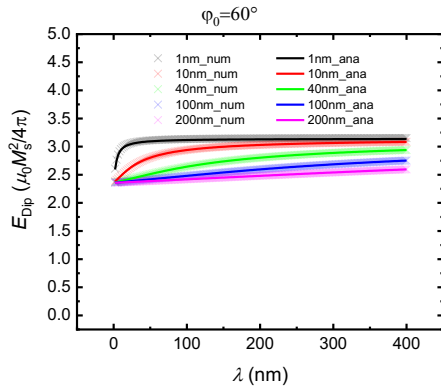
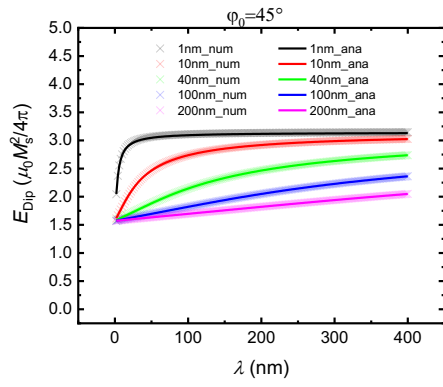
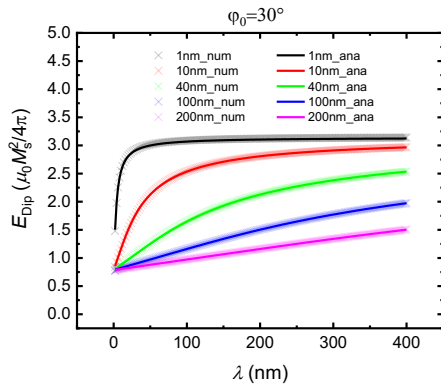
Equation S16 is consistent with Equation S5-S8 so confirming its validity.

The field is then calculated from $\vec{H} = -\nabla U$ and thus we calculate the final volume dipolar energy:

$$E_{Dip} = \frac{\mu_0 M_s^2 \sin^2(\varphi_0)}{4} + \frac{\mu_0 M_s^2 \lambda}{8L_z \pi} \left(1 - e^{-\frac{2\pi}{\lambda}L_z} \right) (1 - \sin^2 \varphi_0) \quad (S19)$$

Numerical calculations are also performed to confirm the validity of Equation S19, as shown in Figure S8.





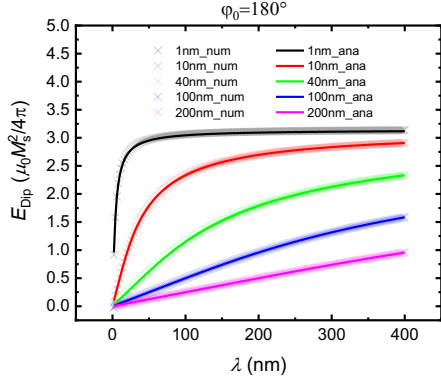


Figure S8. Comparison of numerical calculations with analytical formula

We now compare the energy of a Bloch helix with other structural forms. The energy difference is calculated to be:

$$\Delta E_{Dip} = E_{Dip,Bloch} - E_{Dip,Other} = \frac{\sin^2 \varphi_0 \mu_0 M_s^2}{4} \left[\frac{\lambda}{2\pi L_z} \left(1 - e^{-\frac{2\pi L_z}{\lambda}} \right) - 1 \right] \quad (S20)$$

We define $x = \frac{2\pi L_z}{\lambda}$, due to the positive value of L_z and λ , $x > 0$

$$\text{Thus, } \Delta E_{Dip} = \frac{\sin^2 \varphi_0 \mu_0 M_s^2}{4} \left(\frac{1 - e^{-x}}{x} - 1 \right) \leq 0 \quad (S21)$$

Equation S21 shows that a Bloch helix will always have the lowest dipolar energy as compared to all other structures regardless of thickness and period. This is the reason that, when there is no field, the helix in a D_{2d} system will always have a Bloch form and thus will propagate only along the $[100]/[010]$ directions.

D. Finite size effect on the magnetic dipolar interaction

In the above calculations, the sample was considered to have infinite size within the XY plane. In a real sample, the size is limited, e.g. in our FIB lamella L1-4 the in-plane dimension is of the order of a few μ m. Here we perform some calculations to show the influence of such a finite size effect. We use two methods. The first method is similar to that described in section B, but with size confinement along X. The second method uses micromagnetic simulations, where the helix structure is fixed and the dipolar energy is calculated using the open source micromagnetic simulation software OOMMF's^[3] internal energy calculator. As shown in Figure S9, the agreement between the two methods is very good. We find that the dipolar energy has, on top of the

dependence on thickness found earlier, an additional term which oscillates with thickness. The period and amplitude of this oscillation increase as the helix period increases. Such an additional term can lead to plateaus in the thickness dependent helix period.

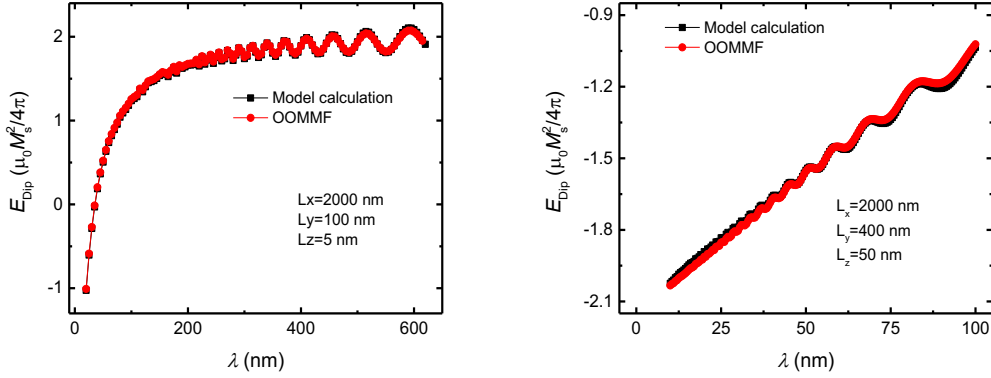


Figure S9. E_{Dip} as a function of λ for several sizes calculated by a model and via OOMMF. **a**, $L_x = 2000 \text{ nm}$, $L_y = 100 \text{ nm}$ and $L_z = 5 \text{ nm}$, **b**, $L_x = 2000 \text{ nm}$, $L_y = 400 \text{ nm}$ and $L_z = 50 \text{ nm}$.

E. Position dependence of the dipolar energy density

In section A we calculated the averaged volume dipolar energy. From the model discussed in section A, the dipolar energy density can be expressed as:

$$E_{Dip,density}(x, y, z) = \frac{\mu_0 M_S^2}{4} \cos^2\left(\frac{2\pi x}{\lambda}\right) \left[e^{-\frac{2\pi}{\lambda}\left(\frac{L_z}{2}-z\right)} + e^{-\frac{2\pi}{\lambda}\left(z+\frac{L_z}{2}\right)} \right] \quad (\text{S22})$$

In this section, we plot the position dependent energy density in the XZ cross section plane to help better understand the thickness dependent behavior of the dipolar energy.

Figure S10 shows the dipolar energy density in a sample with $t = 200 \text{ nm}$. In Figure S10a-l, the helix wavelength is varied from 50 nm to 600 nm. In Figure S11, the dipolar energy density is shown in a system with $\lambda = 500 \text{ nm}$. In Figure S11a-l, the thickness is varied from 100 nm to 650 nm. As shown in Equation S22, the dipolar energy density has a $\cos^2\left(\frac{2\pi x}{\lambda}\right)$ variation along the x direction and two exponentially decaying terms with a characteristic length of λ along the z direction. When λ is much smaller than t , the dipolar energy is dominant at the surfaces with a rapid decay to zero towards the middle of the sample. When λ is increased or t is decreased, the dipolar energy is not only increased at the surfaces but also appears towards the center of the sample. Clearly, the volume dipolar energy decreases as λ becomes smaller and/or t becomes larger, since the less twisted structure increases the net accumulated ‘magnetic charge’.

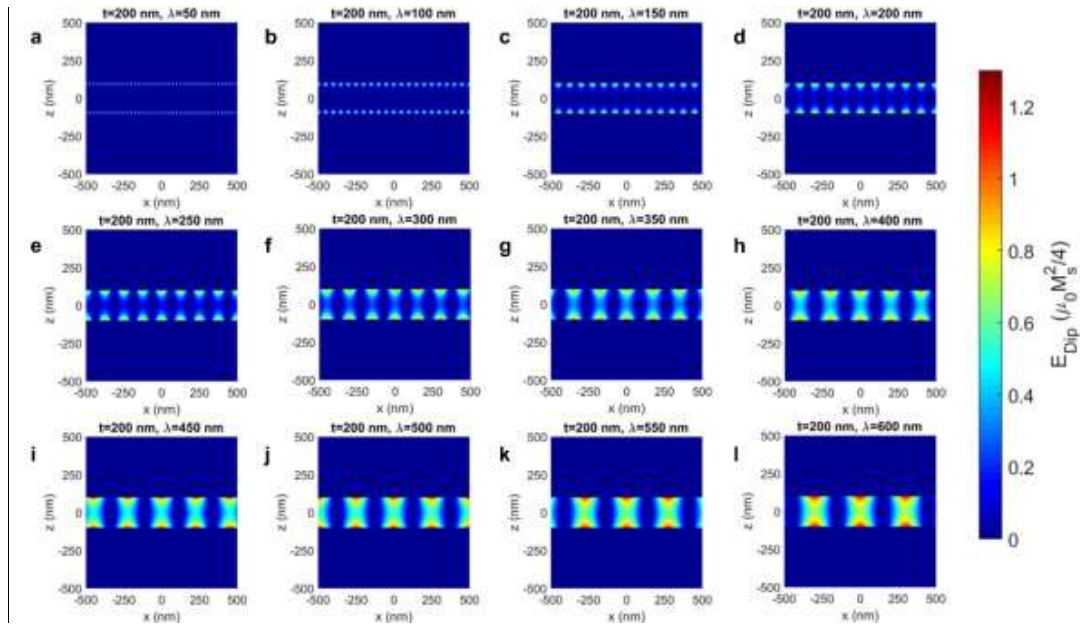


Figure S10. Position dependent dipolar energy density as a function of λ for $t=200$ nm. (a-l) λ is varied from 50 nm to 600 nm.

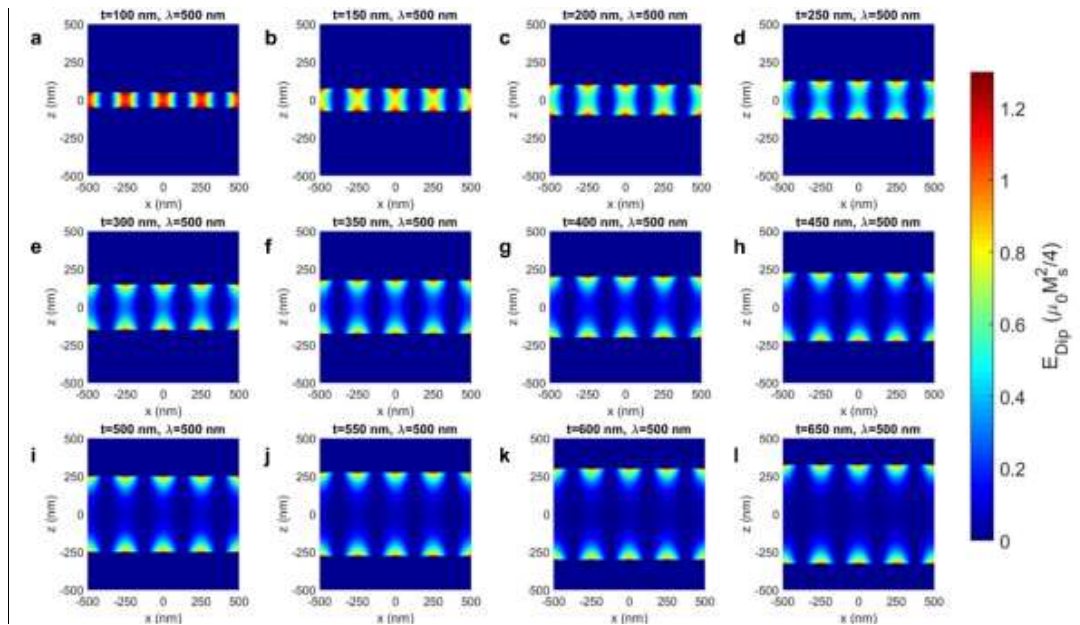


Figure S11. Position dependent dipolar energy density as a function of t for $\lambda = 500$ nm. (a-l) t is varied from 100 nm to 650 nm.

Typical calculated results of helix wavelength as a function of thickness

Calculated results of helical wavelength λ versus t are shown as 3D colormaps in Figure 5c-d of the main manuscript. In Figure S12a, λ vs t is shown for $A=15 \text{ pJ m}^{-1}$, and $M_s=600 \text{ kA m}^{-1}$ for $|D|$ ranging from 0.5 mJ m^{-2} to 3.0 mJ m^{-2} . In Figure S12b, λ vs t is shown for $A=15 \text{ pJ m}^{-1}$, and $|D|=0.5 \text{ mJ m}^{-2}$ for M_s ranging from 300 kA m^{-1} to 900 kA m^{-1} .

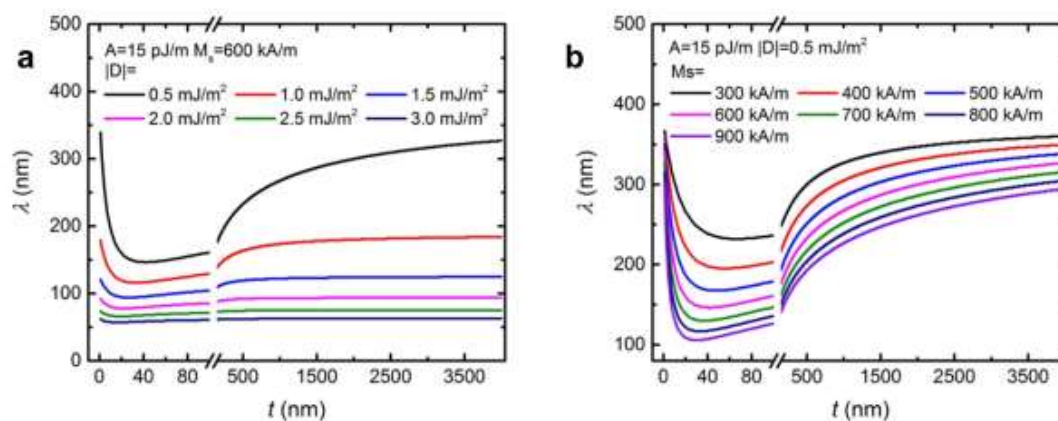


Figure S12. Typical calculated results of helix wavelength λ as a function of lamella thickness t .

Comparison of the experiment result of helix wavelength as a function of thickness with model calculation

In Figure S13, the experimentally determined dependence of λ vs t is compared with a model calculation using $A=30 \text{ pJ m}^{-1}$, $D=0.1 \text{ mJ m}^{-2}$ and $M_s=445 \text{ kA m}^{-1}$. The trend of increasing λ with thickness that we find experimentally is well reproduced. Note that, as discussed in the main manuscript, the model is qualitative rather than quantitative. This is likely because the actual magnetic structure is very likely somewhat distorted from the assumed simple Bloch-like helix, and, the calculated λ vs t is a complex competition between Heisenberg exchange, DMI and the dipolar and anisotropy energies, so is difficult to extract these magnetic parameters by fitting the data. The parameters used here are for a qualitative comparison only.

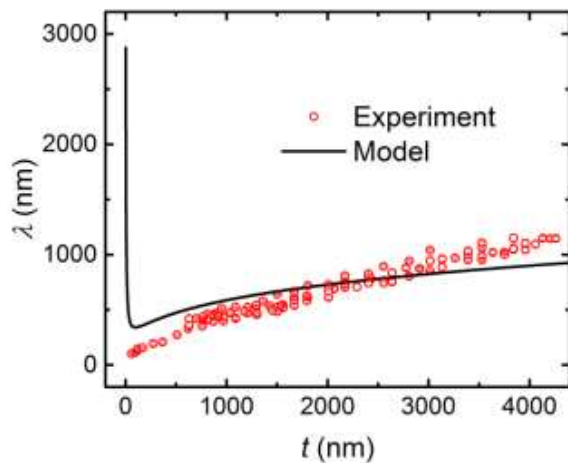


Figure S13. Comparison of the experimentally determined helix wavelength λ as a function of thickness with a model calculation: the modal calculation uses these parameters: $A=30 \text{ pJ m}^{-1}$, $D=0.1 \text{ mJ m}^{-2}$ and $M_s=445 \text{ kA m}^{-1}$.

References

- [1] A. Aharoni, *Introduction to the Theory of Ferromagnetism*, Oxford University Press, Oxford, **2001**.
- [2] a) G. Chen, J. Zhu, A. Quesada, J. Li, A. N'Diaye, Y. Huo, T. Ma, Y. Chen, H. Kwon, C. Won, *Phys. Rev. Lett.* **2013**, *110*, 177204; b) G. Chen, T. Ma, A. T. N'Diaye, H. Kwon, C. Won, Y. Wu, A. K. Schmid, *Nat. Commun.* **2013**, *4*, 2671.
- [3] M. J. Donahue, D. G. Porter, User's Guide, version 1.0, Interagency Report NISTIR 6376 (National Institute of Standards and Technology, Gaithersburg, 1999); available at <http://math.nist.gov/oommf>.

5. Nanoscale non-collinear spin textures in thin films of a D_{2d} Heusler compound

After studying antiskyrmions in bulk crystals of the D_{2d} compound in the previous chapter, this chapter discusses the observation of non-collinear spin textures in thin films of a D_{2d} Heusler compound. To date, the observations of non-collinear spin textures in D_{2d} systems have been made using lamella extracted from bulk crystals. However, their observation in thin films is desired for technological applications.

In this chapter, the evidence for magnetic nano-objects in epitaxial thin films of Mn_2RhSn using MFM is presented. These nano-objects exhibit a wide range of stability regions with respect to magnetic field and temperature that is similar to single-crystalline lamellae. However, evidence is found for elliptically distorted nano-objects along with perpendicular crystallographic directions within the epitaxial films, which is consistent with elliptical Bloch skyrmions observed in single-crystalline lamellae. Thus, these measurements provide strong evidence for the formation of non-collinear spin textures in thin films of Mn_2RhSn . Using these films, we show that individual nano-objects can be deleted using a local magnetic field from a magnetic tip, and collections of nano-objects can be similarly written. These observations suggest a path towards the use of these objects in thin films with D_{2d} symmetry as magnetic memory elements.

The following chapter of this cumulative thesis has been reprinted from my publication (Reprinted from [27]. Link to the Creative Commons license: <https://creativecommons.org/licenses/by/4.0/>):

A. K. Sharma, J. Jena, K. G. Rana, A. Markou, H. L. Meyerheim, K. Mohseni, A. K. Srivastava, I. Kostanoskiy, C. Felser, S. S. P. Parkin. “Nanoscale non-collinear spin textures in thin films of a D_{2d} Heusler compound”. *Adv. Mater.* **2021**, 2101323

Nanoscale Noncollinear Spin Textures in Thin Films of a D_{2d} Heusler Compound

Ankit K. Sharma, Jagannath Jena, Kumari Gaurav Rana, Anastasios Markou, Holger L. Meyerheim, Katayoon Mohseni, Abhay K. Srivastava, Ilya Kostanoskiy, Claudia Felser, and Stuart S. P. Parkin*

Magnetic nano-objects, namely antiskyrmions and Bloch skyrmions, have been found to coexist in single-crystalline lamellae formed from bulk crystals of inverse tetragonal Heusler compounds with D_{2d} symmetry. Here evidence is shown for magnetic nano-objects in epitaxial thin films of Mn_2RhSn formed by magnetron sputtering. These nano-objects exhibit a wide range of sizes with stability with respect to magnetic field and temperature that is similar to single-crystalline lamellae. However, the nano-objects do not form well-defined arrays, nor is any evidence found for helical spin textures. This is speculated to likely be a consequence of the poorer homogeneity of chemical ordering in the thin films. However, evidence is found for elliptically distorted nano-objects along perpendicular crystallographic directions within the epitaxial films, which is consistent with elliptical Bloch skyrmions observed in single-crystalline lamellae. Thus, these measurements provide strong evidence for the formation of noncollinear spin textures in thin films of Mn_2RhSn . Using these films, it is shown that individual nano-objects can be deleted using a local magnetic field from a magnetic tip and collections of nano-objects can be similarly written. These observations suggest a path toward the use of these objects in thin films with D_{2d} symmetry as magnetic memory elements.

and a ferromagnetic exchange interaction. Perhaps the most extensively studied spin textures are, first, Bloch-like skyrmions that have been observed in noncentrosymmetric B20 compounds, both in single crystals^[5] and in epitaxial films,^[10] and, second, Néel-like skyrmions in thin-film heterostructures formed from ultrathin ferromagnetic layers and a heavy metal layer.^[6,11] The former relies on a volumetric and the latter an interface derived DMI.

In recent studies, the family of inverse tetragonal Mn_2YZ -based Heusler compounds has been shown to sustain magnetic antiskyrmions,^[12–14] another type of noncollinear spin texture that exhibits distinct topological characteristics, and, in addition, elliptical Bloch skyrmions.^[15] These textures are a result of the underlying D_{2d} crystal symmetry that necessarily gives rise to an anisotropic DMI. This DMI also leads to an enhanced stability of antiskyrmions with respect to field and temperature and, the extreme tunability of their size by simply

varying the thickness of the lamella in which exist.^[16,17] The latter is a result of dipole–dipole interactions that is important in compounds with low symmetry, such as D_{2d} and also accounts for the possibility of elliptical Bloch skyrmions in the same material system.^[15,18,19]

To date, all of these observations of noncollinear spin textures in D_{2d} systems have been made using lamella extracted from bulk crystals. However, their observation in thin-films is desired for technological applications, such as Racetrack memory devices.^[20] It remains challenging to make thin films of tetragonal Heusler compounds. In single crystals, high degrees of chemical ordering are achieved by very high temperature annealing processes, but this is not possible in thin-films. This is especially true for the complex thin-film heterostructures that are needed for technological applications, where even modest annealing temperatures leads to intermixing of the constituent layers.

Skyrmions can be observed in real-space by various direct imaging techniques.^[4,21–26] Here, we use magnetic force microscopy (MFM) imaging to investigate magnetic textures in thin films of [001]-oriented Mn_2RhSn . We observe magnetic nano-objects over a wide range of temperature (from 2 to 280 K) and magnetic field. We compare these textures with those that we

1. Introduction

Recently, magnetic skyrmions have received much attention. These topologically protected, noncollinear magnetic spin textured nano-objects^[1–7] are stabilized in magnetic compounds with broken inversion symmetry, and are the result of a competition between a chiral Dzyaloshinskii–Moriya interaction (DMI)^[8,9]

A. K. Sharma, J. Jena, Dr. K. G. Rana, Dr. H. L. Meyerheim, Dr. K. Mohseni, Dr. A. K. Srivastava, Dr. I. Kostanoskiy, Prof. S. S. P. Parkin

Max Planck Institute of Microstructure Physics
Weinberg 2, 06120 Halle, Germany
E-mail: stuart.parkin@mpi-halle.mpg.de

Dr. A. Markou, Prof. C. Felser
Max Planck Institute for Chemical Physics of Solids
Nöthnitzer Str. 40, 01187 Dresden, Germany

 The ORCID identification number(s) for the author(s) of this article can be found under <https://doi.org/10.1002/adma.202101323>.

© 2021 The Authors. Advanced Materials published by Wiley-VCH GmbH. This is an open access article under the terms of the Creative Commons Attribution License, which permits use, distribution and reproduction in any medium, provided the original work is properly cited.

DOI: 10.1002/adma.202101323

find, via Lorentz transmission electron microscopy (LTEM), in single crystals of the same material. Elliptical and round shaped isolated objects are formed with varying sizes that depend upon the field and temperature. Additionally, we also demonstrate the creation and annihilation of these objects with the help of local magnetic field gradients generated by an MFM tip.

2. Results and Discussion

The studies here were carried out on high-quality epitaxial thin films of Mn_2RhSn that were reported previously^[27] (see the Experimental Section). The films were prepared on MgO (001) substrates using DC magnetron sputtering. The observation of a topological Hall effect in these films suggests the presence of noncollinear spin textures.^[27,28] Here, we have carried out variable temperature magnetic force microscopy imaging of several Mn_2RhSn films. We focus on a 35 nm-thick film. The magnetic tip in the MFM is first magnetized in a direction perpendicular to the film surface. The sample is cooled down from 325 K, above the Curie temperature $T_c \approx 294$ K, to low temperatures in zero magnetic field. Typical MFM results taken at 100 K as a function of increasing magnetic field are summarized in **Figure 1**. The initial state after cooling in zero magnetic field is shown in **Figure 1a**. A labyrinth magnetic domain structure is observed in which blue and red colors correspond to regions with magnetization pointing up and down into the plane of the film, respectively. As the magnetic field is increased from zero, the extent of the blue regions increases and, correspondingly, the total extent of the red regions decreases. The labyrinth pattern is retained for small magnetic fields, as shown in **Figure 1b** at 120 mT, but then gradually transforms into an array of irregularly shaped isolated objects at higher fields, as shown in **Figure 1c,d**. These discrete nano-objects, as discussed later, appear to be elliptically shaped, but at even higher magnetic fields (**Figure 1e**) the objects become circularly shaped. A

saturated magnetic state is achieved at ≈ 200 mT. The size of the nano-objects varies from ≈ 190 – 225 nm depending on the temperature (see **Figure S1** in the Supporting Information).

Similar measurements were performed at various temperatures. The labyrinth domain phase was observed at all temperatures from 2 to 280 K, but the range of magnetic field over which this structure was found increased with decreasing temperature. The range of field for which isolated objects was found had a weaker temperature dependence, decreasing only as the Curie temperature is approached. These field regions are plotted in the field–temperature phase diagram in **Figure 1g**.

Results on the Mn_2RhSn thin films were compared with results on a thin ≈ 150 nm-thick [001] zone-axis oriented lamella that was formed from a single-crystalline grain of a bulk polycrystalline $\text{Mn}_2\text{Rh}_{0.95}\text{Ir}_{0.05}\text{Sn}$ sample. The lamella was formed using focused ion milling techniques, as discussed, for example, in ref. [14]. This specimen was examined using LTEM. The field dependent evolution of the spin texture at 150 K is shown in **Figure 2a–d**. LTEM is sensitive to the in-plane magnetization component, as distinct from MFM that is sensitive to the out-of-plane magnetization component. The initial image taken after zero field cooling is quite different from that seen in the thin-film sample discussed above. Rather than a labyrinth structure, an alternating series of black and white regions is observed that is consistent with a helical magnetic structure. This helix has a propagation direction that is oriented approximately along the in-plane [100] direction. As the field is increased the magnitude of the helical period increases significantly and the helical phase is gradually replaced by arrays of elliptically shaped objects. The shape of the nano-objects becomes more circular at higher magnetic fields, for example, at 184 mT (**Figure 2d**). From the LTEM studies these nano-objects can be identified as Bloch-like skyrmions since they can be observed at a zero-tilt angle, θ , of the lamella with respect to the direction of the transmitted electron beam. Note that Néel-like skyrmions display no contrast under these conditions. The nano-objects observed in **Figure 2c**

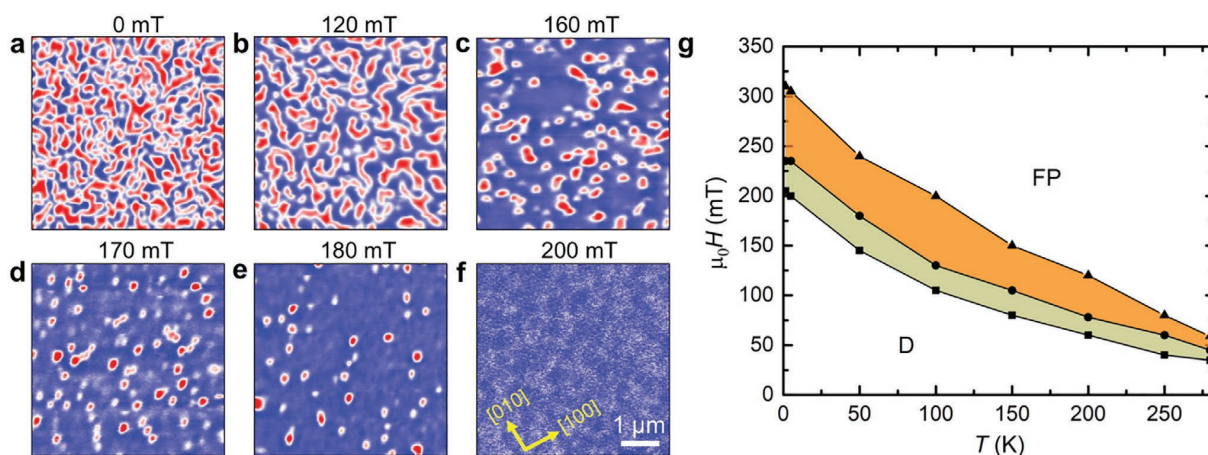


Figure 1. Evolution of nanoscale magnetic textures in a 35 nm-thick Mn_2RhSn film imaged by MFM. a) MFM image at 100 K and zero magnetic field. b–f) Evolution of the nanoscale objects as the magnetic field is increased from 120 to 180 mT and finally to the field polarized state at 200 mT. The blue and red colors correspond to up and down domains respectively. g) Magnetic field versus temperature phase diagram. The khaki-colored area shows a mixed phase of labyrinth and isolated nano-objects, and the orange area a single phase of nano-objects. D and FP correspond to labyrinth domains and field polarized state, respectively. All MFM images are at the same scale: a scale bar is given in (f).

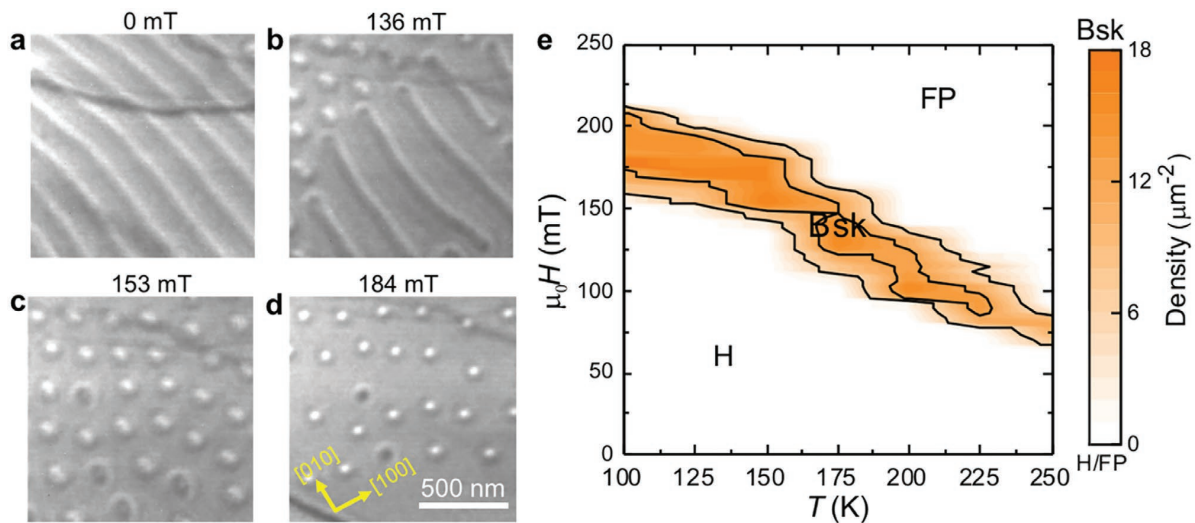


Figure 2. Observation of Bloch skyrmions in a 150 nm-thick $\text{Mn}_2\text{Rh}_{0.95}\text{Ir}_{0.05}\text{Sn}$ single-crystal lamella imaged by LTEM. a) Helical phase at zero field and 150 K. b–d) Magnetic field evolution of Bloch skyrmions. The circles with white and black interiors correspond to Bloch skyrmions with opposite chiralities. All images are at the same scale: a scale bar is given in (d). e) Magnetic field versus temperature phase diagram. Bloch skyrmions are nucleated by applying a temporary tilting angle of 32° along the [100] crystallographic direction. H, Bsk, and FP correspond to helical phase, Bloch skyrmions and field polarized state, respectively.

display an LTEM contrast with either white or black interiors. These correspond to Bloch skyrmions with opposite chiralities^[15] that were first observed in $\text{Mn}_{1.4}\text{Pt}_{0.9}\text{Pd}_{0.1}\text{Sn}$. In an inverse tetragonal Heusler compound the major axes of such elliptical objects are tied to the crystallographic directions [100] and [010]. However, here for $\text{Mn}_2\text{Rh}_{0.95}\text{Ir}_{0.05}\text{Sn}$, these objects are not strictly tied to a particular crystallographic direction. We speculate that this difference arises from the lower magnetization of $\text{Mn}_2\text{Rh}_{0.95}\text{Ir}_{0.05}\text{Sn}$ and the consequent lesser importance of dipole–dipole interactions that stabilize the Bloch skyrmions. We note that anti-skyrmions have previously been observed in Mn_2RhSn in a single-crystalline lamella but under different field–temperature history protocols.^[14] The LTEM results are summarized in the field–temperature phase diagram shown in Figure 2e.

In the single-crystalline, 150 nm-thick lamella, the size of the nano-objects is $\approx 130\text{--}200$ nm, depending on temperature (see Figure S1, Supporting Information). This is comparable to the size of the nano-objects in the film discussed above that was 35 nm thick. However, a very strong increase in size of the magnetic nano-objects in $\text{Mn}_{1.4}\text{PtSn}$ has been reported in single-crystalline lamella as the lamella thickness along [001] was increased. This was reported to be due to the influence of magnetic dipole–dipole coupling, that can be important in compounds with D_{2d} symmetry.^[16] To further explore the role of dipole coupling in thin films of Mn_2RhSn , we have carried out MFM imaging of spin textures in a [001]-oriented film that is 110 nm thick. As shown in Figure S2 (Supporting Information), the spin textures are similar to those we find in the thinner 35 nm-thick film, but the size of the nano-objects is only slightly larger, varying from ≈ 245 to 280 nm. Thus, we conclude that, just as in the single-crystal lamella mentioned above, with regard to the orientation of the Bloch skyrmions, dipole–dipole coupling plays a less important role in Mn_2RhSn than in $\text{Mn}_{1.4}\text{PtSn}$.

A comparison of the phase diagrams for the lamella and the 35 nm-thick thin film of Mn_2RhSn (Figures 1g and 2e) show that the field–temperature stability windows for the observation of discrete nano-objects is similar in both cases. Moreover, in neither case are well-ordered arrays of these objects found, in distinct contrast to $\text{Mn}_{1.4}\text{Pt}_{0.9}\text{Pd}_{0.1}\text{Sn}$, where hexagonal arrays of both antiskyrmions or Bloch skyrmions are typically observed.^[15] After the sample's magnetization is saturated in a large magnetic field, when the field is swept from saturation to small negative fields, no nano-objects are found either in the thin film or the lamella but, rather, the labyrinth state in the one case, and the helical phase in the other case is found. (Note that Bloch skyrmions can be stabilized in the lamella when the field is decreased before the helical phase is formed, by using an additional in-plane field component that is applied by tilting the sample in the transmission electron microscope, as shown in Figure S3 (Supporting Information). The field evolution of magnetic textures in the negative field direction also produces similar nano-objects in MFM (for thin-film) and LTEM (for single-crystalline lamella) following the same procedures used as in Figures 1 and 2, respectively (see Figures S4 and S5, Supporting Information). In none of these experiments was any evidence found for pinning of the magnetization textures to specific sites in the film or lamella (as shown in Figures S4 and S5, Supporting Information).

To further investigate the robustness of the nano-objects observed in thin films of Mn_2RhSn , we performed MFM measurements for the 35 nm-thick film in the presence of a vector magnetic field. First, following the aforementioned procedure of Figure 1, isolated nano-objects were stabilized at 120 mT and 200 K, as shown in Figure 3a. Then, the field is rotated from $\theta = 0^\circ$, the normal to the sample plane, toward the sample plane. The nano-objects are stable to this procedure, as shown in Figure 3c–e, as θ is increased from 0° to 45° and then to 90° .

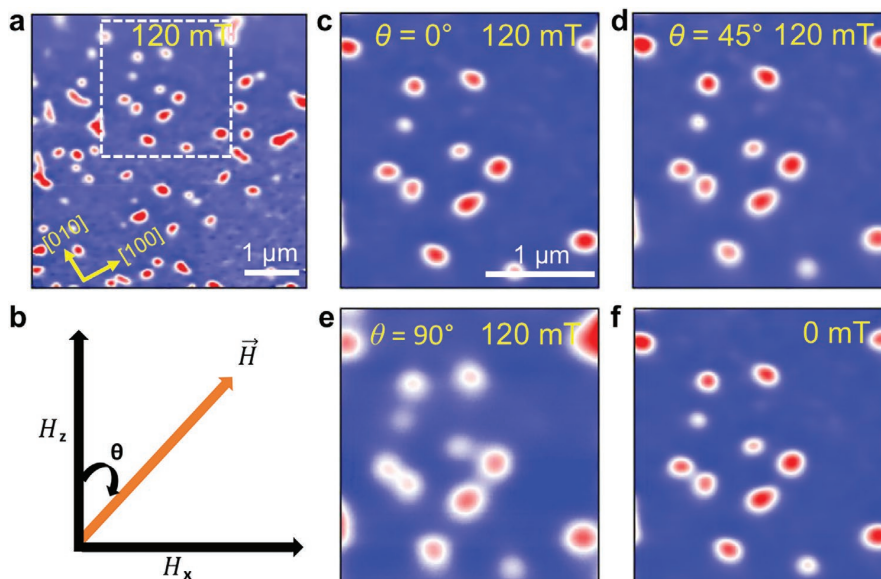


Figure 3. Robust stability of nano-objects in a 35 nm-thick Mn_2RhSn film in a vector magnetic field. a) Isolated nano-objects at 120 mT and 200 K. b) Illustration of field H applied at an angle θ , where H_z ($\theta = 0^\circ$) and H_x ($\theta = 90^\circ$) are out-of-plane and in-plane fields applied to the film. The area marked by the white dashed square is shown enlarged in (c)–(f). c) Portion of (a). d–f) MFM images in the presence of $H = 120$ mT, after the angle θ has been changed from 0° to 45° and 90° , in (d) and (e) respectively, and after the field has been reduced to zero in (f).

When the magnitude of the field is then reduced to zero, the nano-objects remain, as shown in Figure 3f. This contrasts with the case when the perpendicular field magnitude is reduced to zero without any tilt when, as discussed earlier, the labyrinth state is formed. These results emphasize the sensitivity of the magnetization texture in Mn_2RhSn films to the field history protocol.

To reinforce the sensitivity of the magnetization state of the 35 nm-thick thin-film sample to the temperature-field history, a field cooling procedure was carried out from above the Curie temperature to low temperatures in the presence of an out-of-plane magnetic field. Here a field of 10 mT was applied as the sample was cooled from 325 to 5 K. As shown in Figure 4a, a collection of nano-objects is now found at 5 K, in sharp contrast to the labyrinth state that is observed when cooling without any magnetic field (see Figure S6, Supporting Information). As the temperature is subsequently increased, the image remains qualitatively the same up to a temperature of ≈ 150 K. Above this temperature, however, the size of the nano-objects gradually increases. Individual nano-objects could be followed as a function of temperature, as shown in Figure 4. The average size of the objects is summarized in Figure 4g as a function of temperature. The line-profiles of a nano-object highlighted by the yellow circles in Figure 4a–f are plotted in the inset of Figure 4g. The size was calculated using the method described,^[17] which agrees well with the size determined from the line profiles of the nano-object. These low-field stabilized nano-objects are metastable and, therefore, have a larger size than the field-driven nano-objects as shown in Figure 1. The density of the nano-objects was found to decrease with increasing temperature. Similar experiments were carried out for the lamella, as shown in Figure S7 (Supporting Information).

Finally, we explore the writing and deleting of nano-objects in Mn_2RhSn thin films, using the stray magnetic field from an MFM tip, in the absence of any applied field. The field generated by the tip must be equal to or larger than the nucleation field for the nano-object. The MFM tip used for all the images discussed above was too small for this purpose and played little or no role in the MFM images presented so far. To accomplish writing of nano-objects, a different MFM tip was used which had a much larger stray field (see the Experimental Section). The following procedure for the 35 nm-thick film was used at 200 K. First, the magnetization of the sample and the MFM tip were set in the same direction by applying an external field of 200 mT at 250 K. Then, the sample magnetization alone was reversed by applying a field of -80 mT (the coercivity of the sample at this temperature is 70 mT, whereas the tip has a coercivity of ≈ 90 mT). The external field was then reduced to zero and the sample was cooled to 200 K in zero field. Finally, writing was carried out, as shown in the sequence of MFM images in Figure 5a–e. These images are taken in a noncontact mode, i.e., at a given fixed tip to sample distance, z . First, the scan was carried out at $z = 80$ nm, where no magnetic contrast is observed (see Figure 5b). At this height, the stray field of the tip is too small to influence the sample magnetization. When z is reduced to below 50 nm, the sample magnetization begins to reverse with the formation of a labyrinth pattern. When z is decreased below 30–20 nm, the labyrinth evolves into isolated nano-objects. (Note that nano-objects can also be written in contact mode, as shown in Figure S8 (Supporting Information)).

To delete the nano-objects, the magnetization of the MFM tip should be aligned in the same direction as the external field. The field from the tip adds to the external field, which, thereby, can lead to the annihilation of a nano-object. An example is

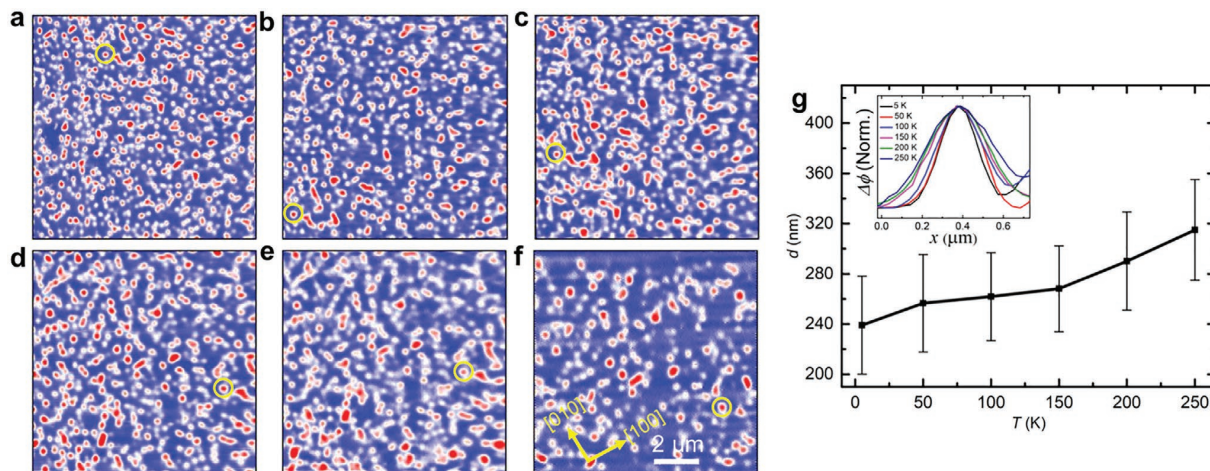


Figure 4. Temperature dependence of nanoscale objects in a 35 nm-thick Mn_2RhSn thin. a–f) MFM images in 10 mT at a temperature of 5, 50, 100, 150, 200, and 250 K, respectively. g) Size dependence of nano-objects with temperature. The error bars represent the standard deviation of the nano-object size. The inset shows the line profiles of the same nano-object that is highlighted by the yellow circles in (a)–(f). All images are at the same scale: a scale bar is given in (f).

shown in Figure 5g for the 35 nm-thick sample. From the zero-field magnetic state at 100 K, nano-objects are first created by applying an external field of 180 mT. Two isolated nano-objects are shown in Figure 5g. When $z = 70$ nm, the stray field from the tip is too weak to perturb the nano-objects. When z is reduced to 50 nm (Figure 5h), the first nano-object highlighted in the dashed circle is annihilated and the second nano-object is annihilated when z is further reduced to 30 nm.

We suggest that the variation in sizes of the isolated magnetic objects and the absence of helical order in our thin films can be attributed to chemical inhomogeneity on the atomic scale. Although high-resolution transmission electron microscopy on similar films shows no clear evidence for any such inhomogeneity,^[27,28] we have carried out X-ray diffraction experiments on the 35 nm-thick film using a high brilliance gallium-jet X-ray source. We find that the film structure is characterized

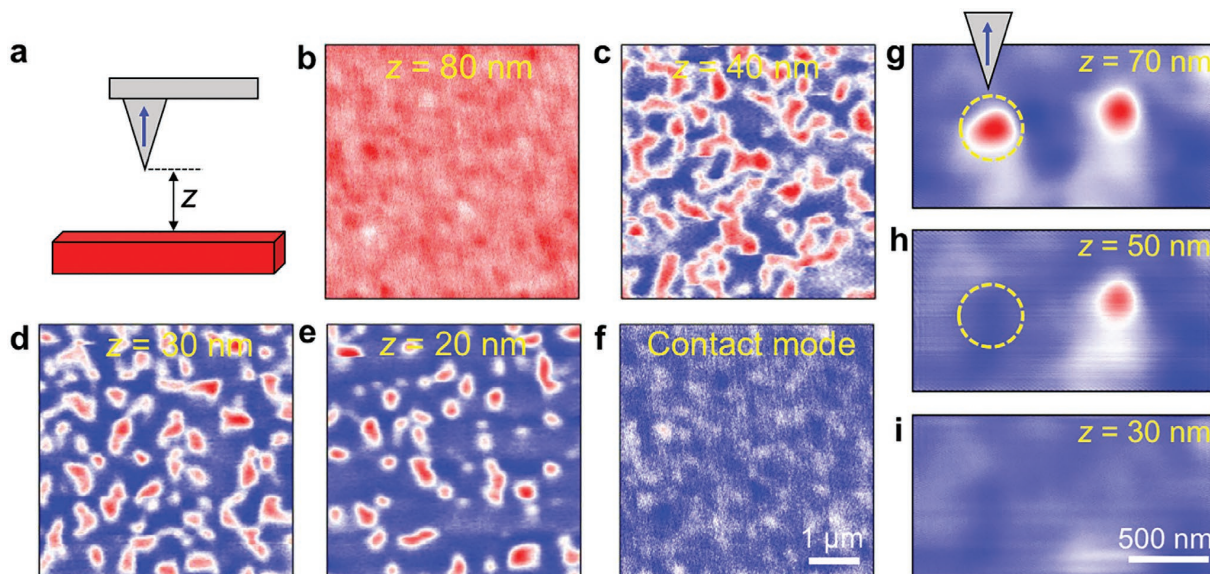


Figure 5. Controlled creation and annihilation of nano-objects in a 35 nm-thick Mn_2RhSn thin film. a) Schematic illustration of magnetization orientations of MFM tip and sample for writing. The distance between tip and the sample is the scan height z . b–e) MFM images in zero field and $z = 80, 40, 30,$ and 20 nm, respectively at 200 K. f) Contact-mode image in zero field and 200 K. The blue and red colors represent up and down magnetization, respectively. Images in (b)–(f) are at the same scale: a scale bar is given in (f). g–i) MFM images taken at $z = 70, 50,$ and 30 nm at 100 K under $H_z = 180$ mT. Images in (g)–(i) are at the same scale: a scale bar is given in (i).

by the presence of about 6 at% of vacancies at the Mn and Rh sites, while a few percent of Mn atoms occupy otherwise empty sites in the unit cell. From this analysis the film composition is derived to be $\text{Mn}_{2.02}\text{Rh}_{0.94}\text{Sn}_{1.00}$ (see Figures S9 and S10 (Supporting Information)). It is a challenge to realize high levels of chemical ordering in thin films of Heusler compounds because typically this requires high temperatures, as is used, for example, in the growth of high-quality single crystals of Heusler compounds.^[14] One method that has been shown to give rise to chemical ordering at temperatures as low as even room temperature for binary Heusler compounds is the chemical templating (CTL) method.^[29] It is of great interest to explore this method in the future and see whether it can be extended to ternary Heuslers. If one can prepare ultrathin D_{2d} Heusler films, the current driven motion of noncollinear nanoscale objects in such films driven by spin-orbit torques can be explored by combining these films with layers in which there is significant charge to spin conversion.^[22,30,31] To date, we have not seen any significant motion of these objects in lamellae or thin films from volume spin transfer torques generated by current passed directly through them.

3. Conclusion

Nanoscale spin textures are observed in thin films of [001]-oriented Mn_2RhSn using MFM and compared with those observed in a single-crystalline lamella using LTEM. We find that the stability region of nano-objects with respect to temperature and magnetic field is extensive and similar in both cases. In neither case are well ordered arrays of the magnetic nano-objects found. However, a labyrinth domain structure is observed in the thin film, in contrast to the bulk lamella where a helical structure is found under similar field-temperature conditions. We find evidence of a small increase in size of the magnetic nano-objects with increasing film thickness, but which is a much smaller variation than previously seen in a related Heusler compound with D_{2d} symmetry. This suggests that magnetostatic energy plays a less important role in Mn_2RhSn , which we attribute to its comparatively lower magnetization. Detailed X-ray structural studies of the thin films suggest that there is chemical inhomogeneity that may account for the absence of a helical phase and the large size variation of the magnetic nano-objects. In films that had even greater degrees of chemical inhomogeneity no magnetic nano-objects were seen nor was the labyrinth phase found, providing further evidence that the observation of well-defined spin textures in thin Heusler films requires highly chemically ordered films.

Our studies suggest that the nano-objects we have found in thin films of Mn_2RhSn are likely Bloch skyrmions or antiskyrmions, that we observe in single-crystalline lamella of the same material. Moreover, we have demonstrated that individual nano-objects can be deleted or created by local magnetic fields. Our work paves the way to the realization of skyrmionic devices based on Heusler thin films.

4. Experimental Section

Thin-Film Growth: Thin films of Mn_2RhSn were grown on MgO (001) substrates in a BESTEC UHV magnetron sputtering system using

three independent Mn, Rh, and Sn sources. The films were grown by cosputtering at 400 °C and then post annealed in situ for 30 min to improve chemical ordering. To prevent oxidation, the films were capped with 3 nm-thick TaN films that were deposited at room temperature. The film structure and stoichiometry were characterized using X-ray diffraction (XRD), X-ray photoelectron spectroscopy (XPS), and Rutherford backscattering spectrometry (RBS).

XRD: The crystal structure of the Mn_2RhSn thin films was investigated by XRD using a Ga-Jet X-ray source operated at 70 keV and 100 W power emitting Ga-K α radiation ($\lambda = 1.3414 \text{ \AA}$) and a six-circle diffractometer specially designed for the study of thin films. The primary beam is incident on the sample under a constant grazing incidence angle ($\mu = 1^\circ$) to the surface. Integrated reflection intensities were collected by rotating the sample around its surface normal while the 2D pixel detector is kept at a constant angle to accept the scattered beam. The structure analysis was carried out by least squares refinement of calculated structure factor magnitudes to the observed ones.

MFM: MFM measurements were carried out in a variable temperature system from Attocube (attoAFM 1) equipped with a vector superconducting magnet, so that magnetic fields can be applied both in-plane and out-of-plane to the sample (attoLIQUID2000). All measurements were carried out in vacuum with a large quality factor ($Q > 30\,000$) of the cantilever that allows for high force sensitivity. A magnetic probe from Nanosensors (SSS-QMFM) with a tip radius of $\approx 20 \text{ nm}$ was used for imaging the magnetic textures using a phase modulation technique in noncontact mode. MFM imaging was carried out in two steps. First, the tilt and misalignment of the sample was corrected and topography was acquired. Then, to measure magnetic forces, the cantilever was retracted from the sample surface and scanned at a fixed lift height (50–60 nm). For writing and deleting the nano-objects, magnetic probes from Nanoworld (Model: MFMR) were used that have a tip radius of $\approx 50 \text{ nm}$.

Lamellae Preparation and Lorentz TEM: The bulk polycrystalline Heusler compound $\text{Mn}_2\text{Rh}_{0.95}\text{Ir}_{0.05}\text{Sn}$ was prepared by an arc-melting method. Electron backscattering diffraction was performed in a TESCAN GAIA 3 (Quantax, Bruker) system to identify [001]-oriented grains. Single-crystalline lamellae were fabricated from single [001]-oriented grains by a Ga⁺ ion based dual beam focused ion beam (FIB) system [FEI Nova Nanolab 600 SEM/FIB], that was operated using an accelerating voltage of 30 kV. The details of the structural characterization and fabrication can be found elsewhere.^[14] An aberration-corrected high-resolution transmission electron microscope (FEI TITAN 800-300) was used to observe the magnetic contrast in the LTEM mode. The magnetic field was varied along the microscope axis by partially exciting the objective lens current. A double-tilt liquid nitrogen holder was used to vary the temperature of the specimen from 100 to 300 K. The in-plane field components were realized at the specimen surface by tilting the sample holder up to $\pm 32^\circ$. The defocus value for the LTEM imaging is $\approx 1.1 \text{ mm}$.

Supporting Information

Supporting Information is available from the Wiley Online Library or from the author.

Acknowledgements

A.K.S. and J.J. contributed equally to this work. The authors acknowledge funding from the European Research Council (ERC) under the European Union's Horizon 2020 research and innovation program (grant agreement SORBET No. 670166). They also acknowledge funding from the Deutsche Forschungsgemeinschaft (DFG, German Research Foundation) – Project No. 403505322 under SPP2137. C.F. acknowledges funding from the DFG under SPP 2137 (Project No. 403502666).

Open access funding enabled and organized by Projekt DEAL.

Conflict of Interest

The authors declare no conflict of interest.

Data Availability Statement

The data that support the findings of this study are available from the corresponding author upon reasonable request.

Keywords

Heusler thin films, Mn_2RhSn , noncollinear spin textures, skyrmions, spintronics

Received: February 16, 2021

Published online:

- [1] A. Bogdanov, U. Rößler, M. Wolf, K.-H. Müller, *Phys. Rev. B* **2002**, 66, 214410.
- [2] A. Bogdanov, A. Hubert, *J. Magn. Magn. Mater.* **1994**, 138, 255.
- [3] S. Mühlbauer, B. Binz, F. Jonietz, C. Pfleiderer, A. Rosch, A. Neubauer, R. Georgii, P. Böni, *Science* **2009**, 323, 915.
- [4] X. Yu, Y. Onose, N. Kanazawa, J. Park, J. Han, Y. Matsui, N. Nagaosa, Y. Tokura, *Nature* **2010**, 465, 901.
- [5] X. Yu, N. Kanazawa, Y. Onose, K. Kimoto, W. Zhang, S. Ishiwata, Y. Matsui, Y. Tokura, *Nat. Mater.* **2011**, 10, 106.
- [6] C. Moreau-Luchaire, C. Moutafis, N. Reyren, J. Sampaio, C. Vaz, N. Van Horne, K. Bouzehouane, K. Garcia, C. Deranlot, P. Warnicke, P. Wohlhüter, J.-M. George, M. Weigand, J. Raabe, V. Cros, A. Fert, *Nat. Nanotechnol.* **2016**, 11, 444.
- [7] A. Soumyanarayanan, M. Raju, A. L. Gonzalez Oyarce, A. K. C. Tan, M.-Y. Im, A. P. Petrović, P. Ho, K. H. Khoo, M. Tran, C. K. Gan, F. Ernult, C. Panagopoulos, *Nat. Mater.* **2017**, 16, 898.
- [8] I. Dzyaloshinsky, *J. Phys. Chem. Solids* **1958**, 4, 241.
- [9] T. Moriya, *Phys. Rev.* **1960**, 120, 91.
- [10] A. S. Ahmed, J. Rowland, B. D. Esser, S. R. Dunsiger, D. W. McComb, M. Randeria, R. K. Kawakami, *Phys. Rev. Mater.* **2018**, 2, 041401.
- [11] S. Heinze, K. Von Bergmann, M. Menzel, J. Brede, A. Kubetzka, R. Wiesendanger, G. Bihlmayer, S. Blügel, *Nat. Phys.* **2011**, 7, 713.
- [12] O. Meshcheriakova, S. Chadov, A. Nayak, U. Rößler, J. Kübler, G. André, A. Tsirlin, J. Kiss, S. Hausdorf, A. Kalache, W. Schnelle, M. Nicklas, C. Felser, *Phys. Rev. Lett.* **2014**, 113, 087203.
- [13] A. K. Nayak, V. Kumar, T. Ma, P. Werner, E. Pippel, R. Sahoo, F. Damay, U. K. Rößler, C. Felser, S. S. P. Parkin, *Nature* **2017**, 548, 561.
- [14] J. Jena, R. Stinshoff, R. Saha, A. K. Srivastava, T. Ma, H. Deniz, P. Werner, C. Felser, S. S. P. Parkin, *Nano Lett.* **2020**, 20, 59.
- [15] J. Jena, B. Göbel, T. Ma, V. Kumar, R. Saha, I. Mertig, C. Felser, S. S. P. Parkin, *Nat. Commun.* **2020**, 11, 1115.
- [16] T. Ma, A. K. Sharma, R. Saha, A. K. Srivastava, P. Werner, P. Vir, V. Kumar, C. Felser, S. S. P. Parkin, *Adv. Mater.* **2020**, 32, 2002043.
- [17] R. Saha, A. K. Srivastava, T. Ma, J. Jena, P. Werner, V. Kumar, C. Felser, S. S. P. Parkin, *Nat. Commun.* **2019**, 10, 5305.
- [18] L. Peng, R. Takagi, W. Koshibae, K. Shibata, K. Nakajima, T.-h. Arima, N. Nagaosa, S. Seki, X. Yu, Y. Tokura, *Nat. Nanotechnol.* **2020**, 15, 181.
- [19] J. Jena, B. Göbel, V. Kumar, I. Mertig, C. Felser, S. S. P. Parkin, *Sci. Adv.* **2020**, 6, eabc0723.
- [20] S. S. P. Parkin, M. Hayashi, L. Thomas, *Science* **2008**, 320, 190.
- [21] O. Boulle, J. Vogel, H. Yang, S. Pizzini, D. de Souza Chaves, A. Locatelli, T. O. Mentes, A. Sala, L. D. Buda-Prejbeanu, O. Klein, *Nat. Nanotechnol.* **2016**, 11, 449.
- [22] S. Woo, K. Litzius, B. Krüger, M.-Y. Im, L. Caretta, K. Richter, M. Mann, A. Krone, R. M. Reeve, M. Weigand, *Nat. Mater.* **2016**, 15, 501.
- [23] W. Jiang, P. Upadhyaya, W. Zhang, G. Yu, M. B. Jungfleisch, F. Y. Fradin, J. E. Pearson, Y. Tserkovnyak, K. L. Wang, O. Heinonen, *Science* **2015**, 349, 283.
- [24] P. Milde, D. Köhler, J. Seidel, L. Eng, A. Bauer, A. Chacon, J. Kindervater, S. Mühlbauer, C. Pfleiderer, S. Buhbrandt, *Science* **2013**, 340, 1076.
- [25] N. Romming, C. Hanneken, M. Menzel, J. E. Bickel, B. Wolter, K. von Bergmann, A. Kubetzka, R. Wiesendanger, *Science* **2013**, 341, 636.
- [26] Y. Dovzhenko, F. Casola, S. Schlotter, T. Zhou, F. Büttner, R. Walsworth, G. Beach, A. Yacoby, *Nat. Commun.* **2018**, 9, 2712.
- [27] K. Rana, O. Meshcheriakova, J. Kübler, B. Ernst, J. Karel, R. Hillebrand, E. Pippel, P. Werner, A. Nayak, C. Felser, *New J. Phys.* **2016**, 18, 085007.
- [28] P. K. Sivakumar, B. Göbel, E. Lesne, A. Markou, J. Gidugu, J. M. Taylor, H. Deniz, J. Jena, C. Felser, I. Mertig, S. S. P. Parkin, *ACS Nano* **2020**, 14, 13463.
- [29] P. C. Filippou, J. Jeong, Y. Ferrante, S.-H. Yang, T. Topuria, M. G. Samant, S. S. P. Parkin, *Nat. Commun.* **2018**, 9, 4653.
- [30] S. Huang, C. Zhou, G. Chen, H. Shen, A. K. Schmid, K. Liu, Y. Wu, *Phys. Rev. B* **2017**, 96, 144412.
- [31] K.-S. Ryu, L. Thomas, S.-H. Yang, S. S. P. Parkin, *Nat. Nanotechnol.* **2013**, 8, 527.

ADVANCED MATERIALS

Supporting Information

for *Adv. Mater.*, DOI: 10.1002/adma.202101323

Nanoscale Noncollinear Spin Textures in Thin Films of a D_{2d} Heusler Compound

*Ankit K. Sharma, Jagannath Jena, Kumari Gaurav Rana, Anastasios Markou, Holger L. Meyerheim, Katayoon Mohseni, Abhay K. Srivastava, Ilya Kostanoskiy, Claudia Felser, and Stuart S. P. Parkin**

Supplementary information

Nanoscale non-collinear spin textures in thin films of a D_{2d} Heusler compound

Ankit K. Sharma¹, Jagannath Jena¹, K. Gaurav Rana¹, Anastasios Markou², Holger L. Meyerheim¹, Katayoon Mohseni¹, Abhay K. Srivastava¹, Ilya Kostanoskiy¹, Claudia Felser², and Stuart S. P. Parkin^{1*}

¹ Max Planck Institute of Microstructure Physics, Weinberg 2, 06120 Halle, Germany

² Max Planck Institute for Chemical Physics of Solids, Nöthnitzer Str. 40, 01187 Dresden, Germany

Corresponding Author

Email: stuart.parkin@mpi-halle.mpg.de

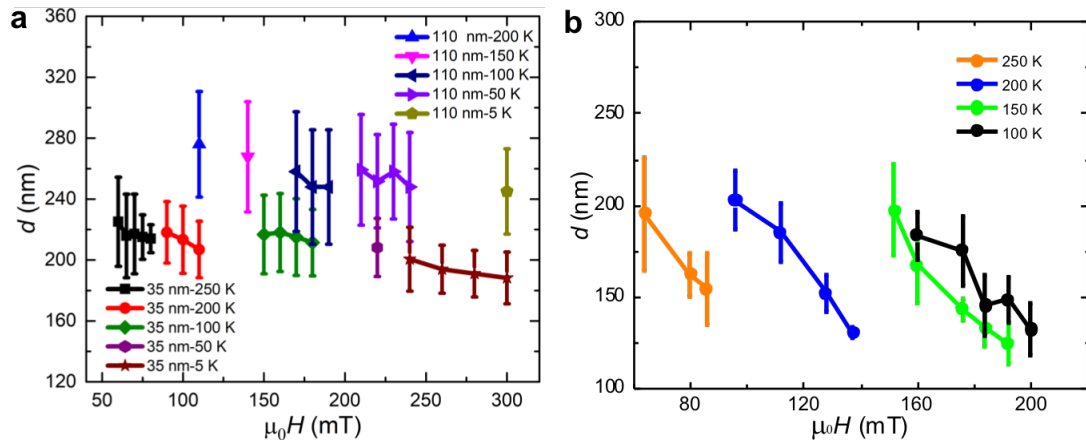


Fig. S1: Size dependence of nanoscale objects in Mn_2RhSn thin films and $\text{Mn}_2\text{Rh}_{0.95}\text{Ir}_{0.05}\text{Sn}$ single crystalline lamella. (a) Size dependence of nano-objects on magnetic field and temperature, for two films with thicknesses of 35 nm and 110 nm. The average size of the nano-objects varies from ~ 190 - 225 nm in the 35 nm thick film, and ~ 245 - 280 nm in the 110 nm thick film, depending on the temperature. (b) Size dependence of nano-objects on magnetic field and temperature in a 150 nm thick lamella. The size of the nano-objects varies from ~ 130 - 200 nm, depending on the temperature.

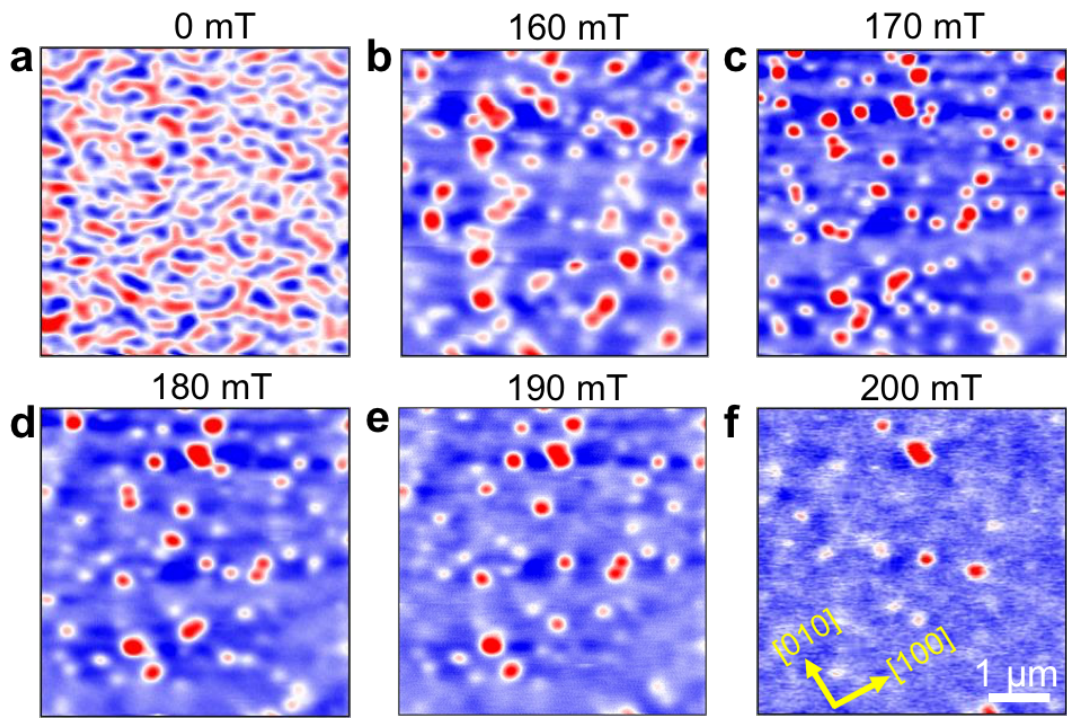


Fig. S2: Evolution of nanoscale objects with field in a 110 nm thick Mn_2RhSn film. (a) MFM image at 100 K and zero magnetic field. (b-f) Evolution of the MFM images as the magnetic field is increased from 160 to 200 mT. The blue and red colors correspond to up and down magnetization respectively. All images are at the same scale: a scale bar is given in (f).

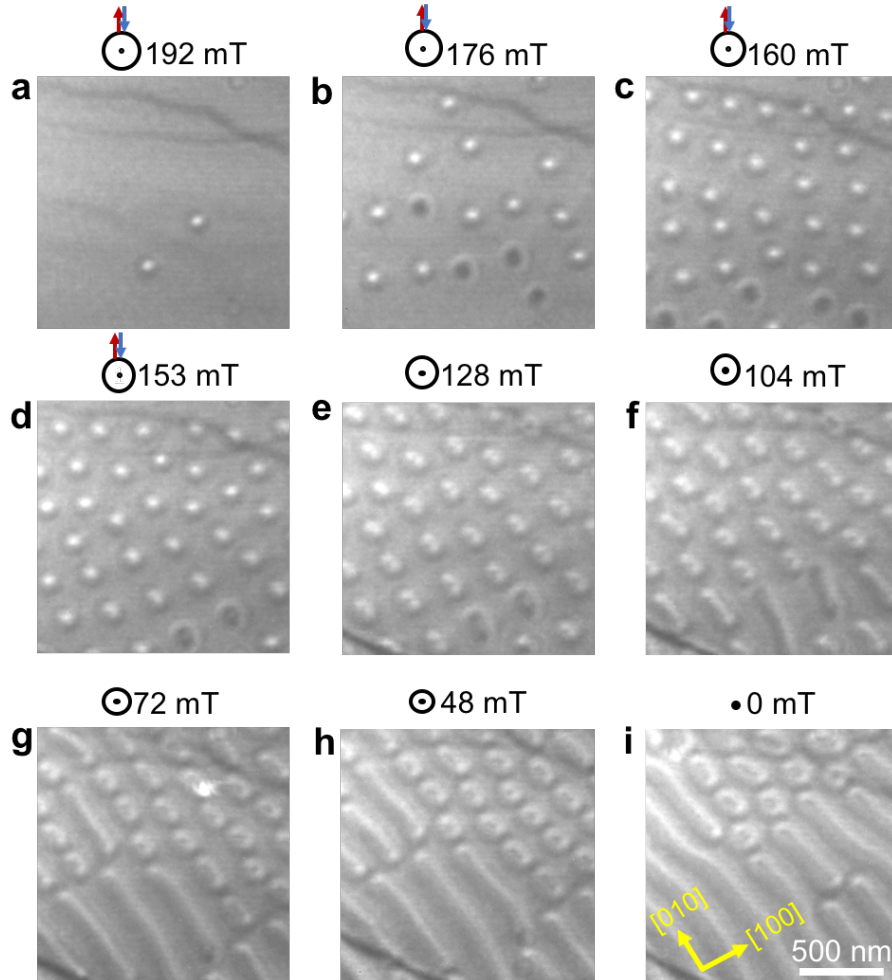


Fig. S3: Bloch skyrmions in a 150 nm thick $\text{Mn}_2\text{Rh}_{0.95}\text{Ir}_{0.05}\text{Sn}$ single crystalline lamella.

The starting configuration is a field polarized state: the images shown are collected as the field is reduced. (a, b) Isolated Bloch skyrmions found at 192 mT and 176 mT, respectively. (c, d) The number density of Bloch skyrmions increases as the magnetic field is decreased. In (a-d), the red and blue arrows represent a reversible temporary tilting of the specimen that is performed to realize an in-plane field component at the specimen. (e-i) The out-of-plane field is further decreased to zero without any sample tilting. In zero field only a few nano-objects are present in the specimen. All images are at the same scale: a scale bar is given in (i).

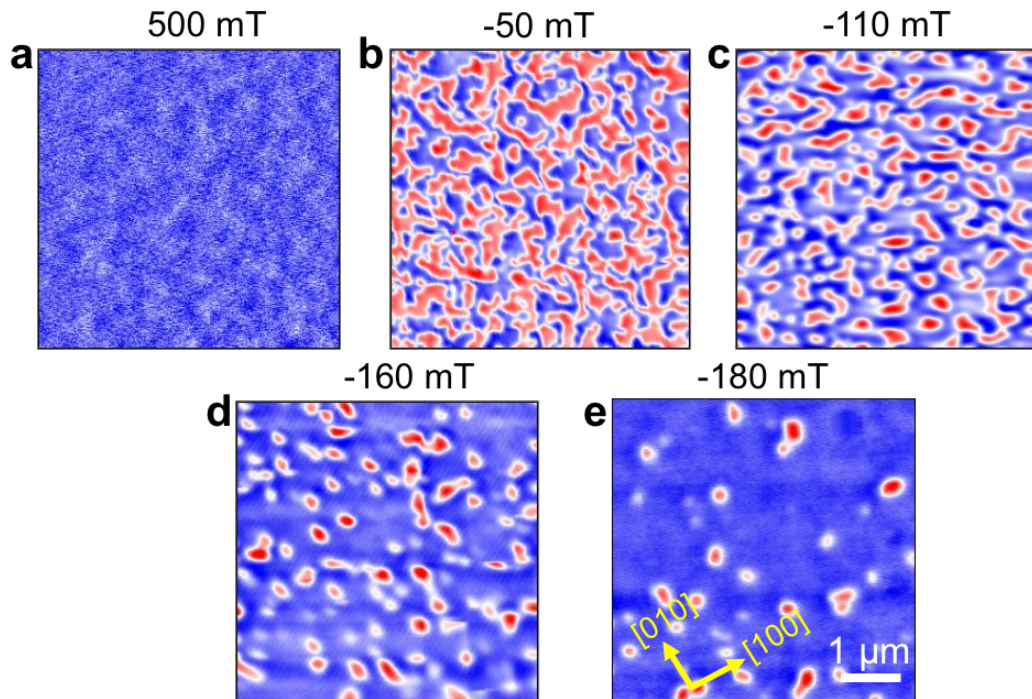


Fig. S4: Evolution of nanoscale objects with magnetic field in a 35 nm thick Mn_2RhSn thin film. (a-f) Magnetic field evolution of magnetic nano-objects starting from the saturated state in a large positive field, as the field is reduced through zero to negative fields. MFM images for positive field values are included in the main text in Fig. 1a-f. (a) After reaching saturation at 0.2 T the field was reduced to zero, where no contrast is observed, and the magnetization is directed along $+z$. When the field is reduced through zero and becomes negative, the magnetization starts switching from $+z$ to $-z$, and a magnetic labyrinth phase is found, as shown in (b). The labyrinth domains start breaking up into nano-objects with both circular and elliptical shapes (c-f), which eventually transform into a saturated magnetic state for a large enough negative field (not shown). All images are at the same scale: a scale bar is given in (e).

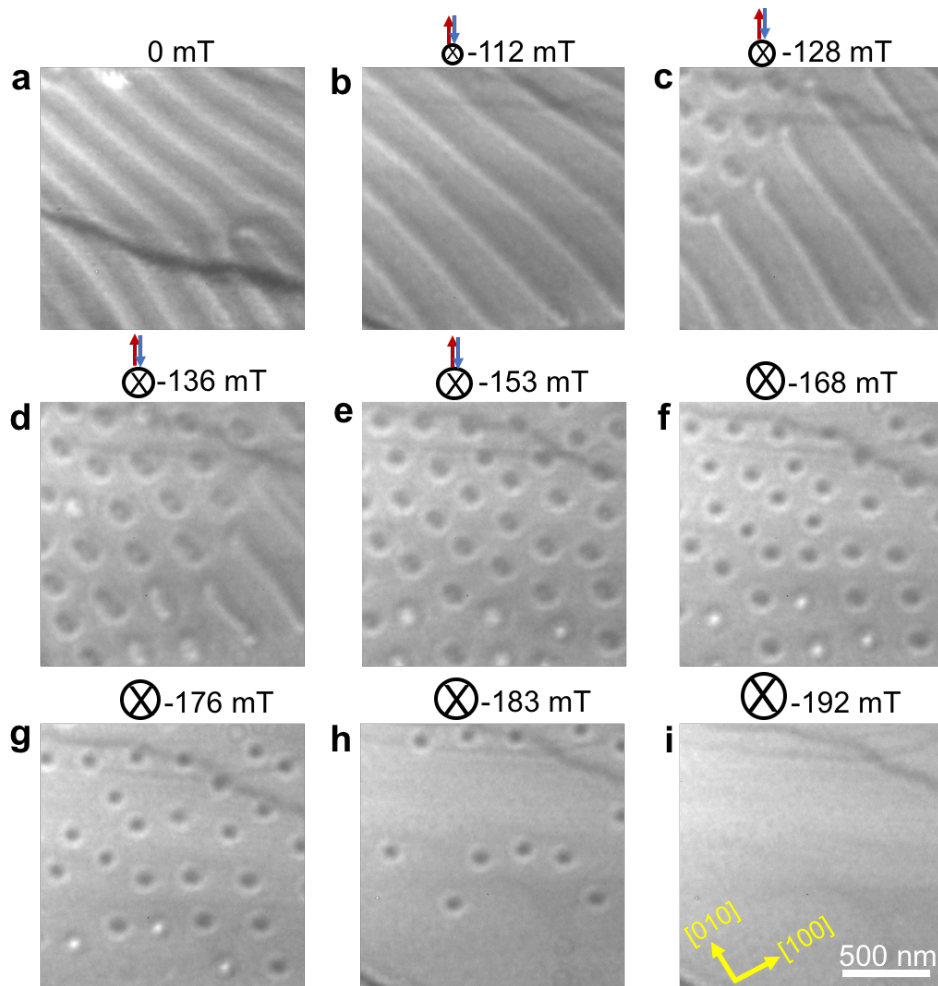


Fig. S5: Bloch skyrmions in a 150 nm thick $\text{Mn}_2\text{Rh}_{0.95}\text{Ir}_{0.05}\text{Sn}$ single crystalline lamella for negative fields. (a) The starting configuration is the helical state in zero magnetic field. (b) The helical period increases with increasing negative magnetic field. (c) Nano-objects, namely Bloch skyrmions, start to form at ~ 128 mT. (d-e) The Bloch skyrmion number density increases with increasing magnitude of the negative field. (f-i) Further increasing the field, the density of Bloch skyrmions starts to decrease and at ~ 192 mT a field polarized state is found. All images are at the same scale: a scale bar is given in (i).

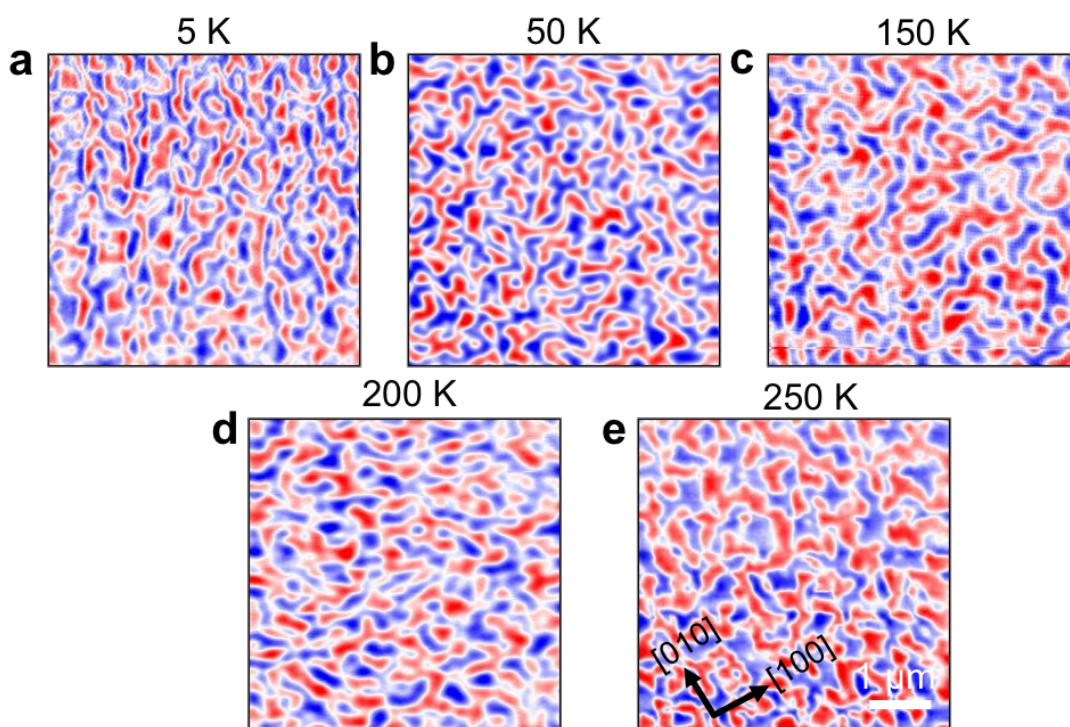


Fig. S6: Magnetic structures in a 35 nm thick Mn_2RhSn thin film after zero field cooling from above 325 K. MFM images of labyrinth domain phase in zero field at (a) 5 K, (b) 50 K, (c) 150 K, (d) 200 K and (e) 250 K. The film was cooled in zero field from above the Curie temperature in each case to the temperature indicated. All images are at the same scale: a scale bar is given in (e).

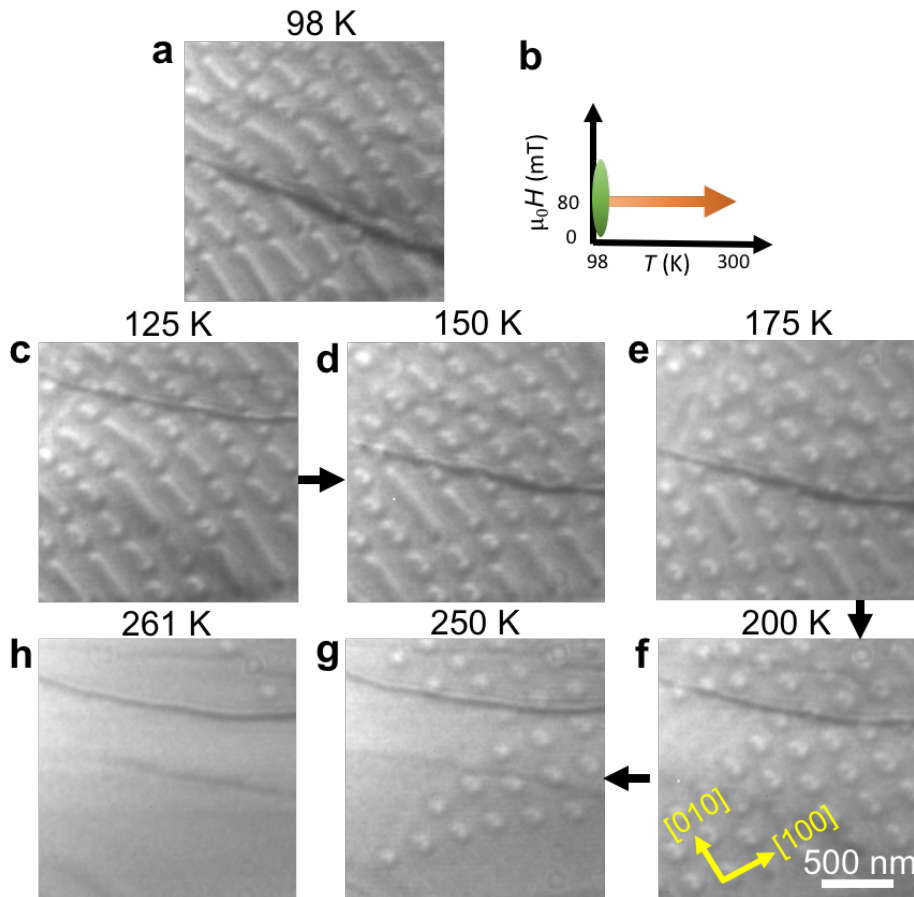


Fig. S7: Temperature dependence of Bloch skyrmions in a 150 nm thick $\text{Mn}_2\text{Rh}_{0.95}\text{Ir}_{0.05}\text{Sn}$ single crystalline lamella imaged using LTEM. (a) After stabilizing a Bloch skyrmion lattice state at a higher field and subsequently decreasing the out-of-plane field, Bloch skyrmions and short helices are found at 98 K and 80 mT. (c–h) Keeping the magnetic field constant (80 mT), the sample is heated to higher temperatures and LTEM images are taken at 125, 150, 175, 200, 250, and 261 K respectively. A schematic of the heating experiment is shown in (b). All images are at the same scale: a scale bar is given in (f).

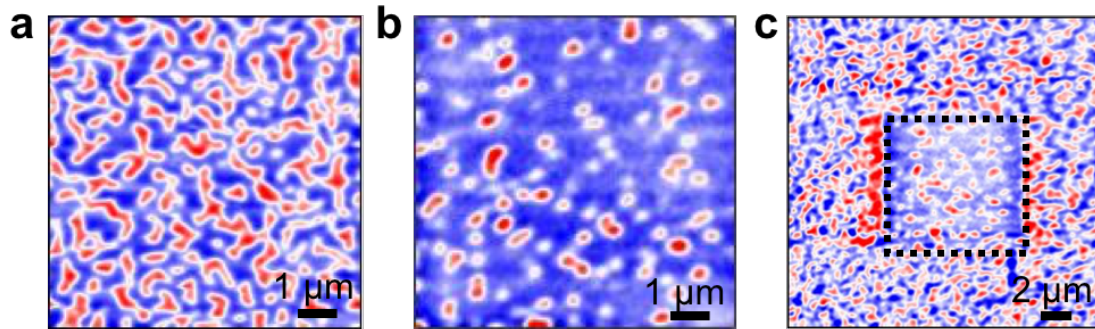


Fig. S8: Writing nano-objects in a 35 nm thick Mn₂RhSn thin film using an MFM tip in contact mode. (a) MFM image taken in non-contact mode at a height of 50 nm in zero field at 220 K. The blue and red colors correspond to up and down magnetization, respectively. The tip is magnetized along the +z direction. (b) MFM image taken in contact-mode of the same region as in (a). The magnetic field from the tip results in the elimination of the labyrinth domains and the formation of nano-objects. (c) MFM image, in non-contact mode at a height of 50 nm, of an extended area around the region shown in b. The nano-objects, which are written by the MFM tip, are marked by a dotted black square.

X-ray diffraction analysis of the 35 nm thick Mn₂RhSn film structure

A detailed investigation of the crystal structure of the 35 nm thick Mn₂RhSn film was carried out by X-ray diffraction (XRD) using an advanced Gallium-Jet X-ray source operated at 70 keV and 100 W power emitting Ga-K α radiation ($\lambda=1.3414$ Å). The monochromatized and focused X-ray beam (horizontal and vertical beam size: 2mm x 100 μ m) is incident onto the sample at a constant grazing incidence angle of $\mu=1^\circ$. Integrated reflection intensities were collected by using a six-circle x-ray diffractometer operated in the z-axis mode [2] by rotating the sample around its surface normal (ϕ -scan) while the position of the 2-dimensional (2D) pixel detector was kept fixed at the in-plane (δ) and out-of-plane (γ) angle associated to each reflection (HKL) [2].

In total 35 reflections were measured reducing to a data set consisting of 15 symmetry independent reflections after symmetry averaging based on the 4mm point group symmetry of the diffraction pattern (out of plane momentum transfer q_z limited to $q_z>0$). The average agreement between symmetry equivalent reflections is equal to 10%. Subsequently, the observed structure factor magnitudes, $|F(\text{HKL})_{\text{obs}}|$, were derived from the integrated intensities by multiplying with instrumental factors (Lorentz, polarization- and effective area) [3,4].

The structure refinement was carried out by least squares refinement of the calculated squared structure factor magnitudes, $(|F(\text{HKL})_{\text{calc}}|^2)$ to the observed ones $(|F(\text{HKL})_{\text{obs}}|^2)$ based on the space group (SGR) $\bar{I}4m2$ (SRG Nr. 119) by using the Program Shelx [5]. In this SGR the Mn atoms occupy the Wyckoff sites 2b at $(x y z) = (0 0 \frac{1}{2})$ and 2c $(0 \frac{1}{2} \frac{1}{4})$, while Sn and Rh atoms occupy Wyckoff sites 2a $(0 0 0)$ and 2d $(0 \frac{1}{2} \frac{3}{4})$, respectively [6]. Owing to the high symmetry of the structure with no free positional parameters $(x y z)$, only an overall scale factor and one common displacement parameter (ADP) [7] is allowed to vary. Based on the perfectly ordered structure we obtain a weighted (Rw) and unweighted (Ru) [8] residuum of $R_w=0.29$

and $R_u=0.059$, respectively. Although these values can be considered as not unsatisfactory, the difference Fourier synthesis exhibits a strong positive peak at the position $(\frac{1}{2} 0 \frac{1}{2})$ corresponding to the Wyckoff site 4f in SGR 119. Figure S9 shows the structure model.

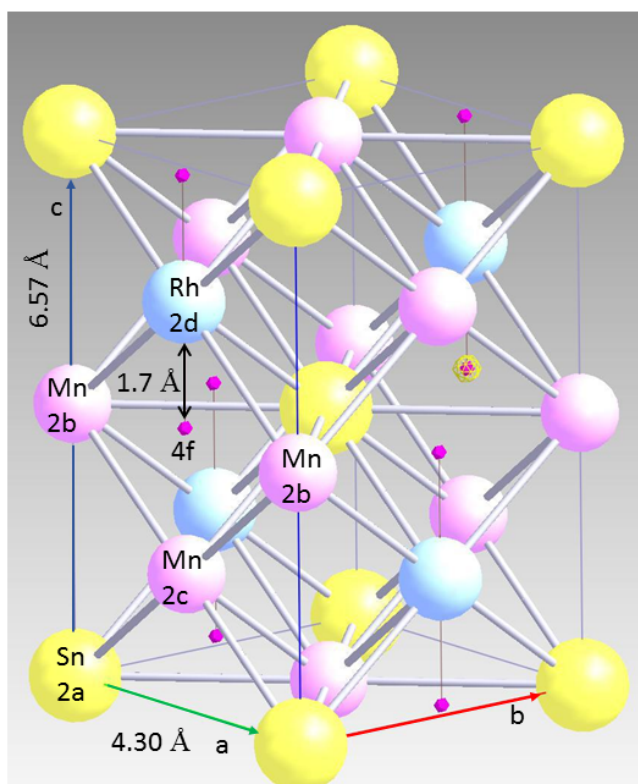


Fig. S9: XRD derived model of the 35 nm thick Mn_2RhSn film structure. Yellow, pink and blue balls represent Sn, Mn and Rh atoms, respectively. Atomic sites are labelled in accordance with their Wyckoff site in space group 119. The 4f site near $(\frac{1}{2} 0 \frac{1}{2})$ shown by small purple balls is derived from the difference Fourier synthesis of the charge density. The detailed analysis (see text) shows that this site is occupied by Mn by a concentration of about 4%, while about the same concentration of vacancies exist in the nearest neighboring sites (2c and 2d).

The strong positive difference density (see purple balls in Fig. S9) indicates that the site near $(\frac{1}{2} \ 0 \ \frac{1}{2})$ is at least partially occupied. As this site (4f in SGR119) is located by only about 1.7 Å ($=c_0/4$) away from neighboring Rh and Mn atoms in site 2d and 2c, the occupation of the 4f site necessarily requires the presence of vacancies in 2d and 2c to at least the same concentration. In order to quantitatively analyze the precise site occupancy of the sites involved as well as to derive the stoichiometry, systematic calculations were carried out.

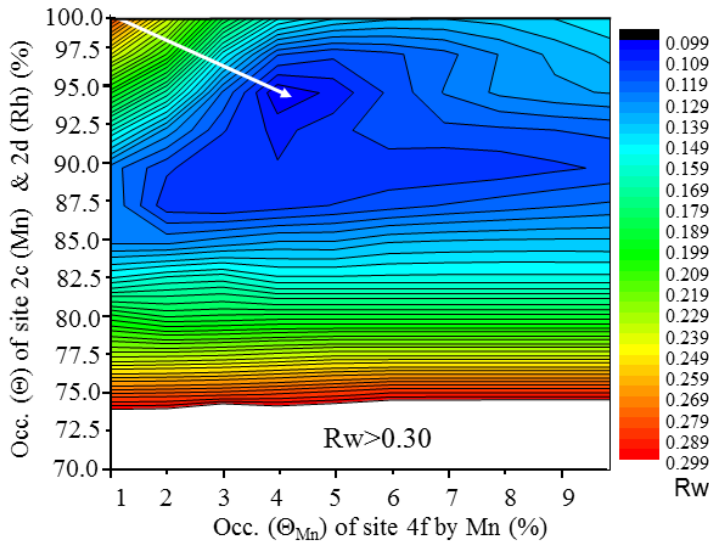


Fig. S10: Contour plot of R_w versus site occupancy (Θ) in Mn_2RhSn for site 4f versus 2d and 2c. The minimum of R_w at the end of the arrow corresponds to a concentration of $\Theta_{Mn}(4f) = 4\%$ and to $\Theta_{Mn}(2c) = \Theta_{Rh}(2d) \approx 94\%$, respectively.

Fig. S10 shows the contour plot or R_w versus occupancy (Θ_{Mn}) of site 4f with Mn versus occupancy of 2d (Θ_{Rh}) and 2c (Θ_{Mn}) which are the next neighbor sites to site 4f. In the non-disordered structure the 4f site is empty, whereas 2d and 2c are completely occupied. This corresponds to $R_w \approx 0.30$ at the upper left of the plot. The fit quality is *dramatically* improved (dropping to about 1/3 of the value obtained for the perfectly ordered structure) by allowing a fraction of about 4% of the 4f site to be populated by Mn while simultaneously a vacancy

density of 6% is introduced into the 2c and 2d site. This is represented by the arrow ending at the minimum of R_w . We have also studied the possibility of other atom exchanges at other sites, but these were found to be negligible within the experimental uncertainty which we estimate to lie in the 5 % range at most. Based on this analysis we derive an average film stoichiometry which can be written as: $Mn_{2.02} Rh_{0.94} Sn_{1.00}$, i.e. there is a slight abundance of Mn within the film structure in relation to Rh and Sn (the concentration of the latter being normalized to 1.00).

We also examined Mn_2RhSn films for which we found no evidence of magnetic nano-objects. The XRD analysis shows that in these films chemical disorder is present which is characterized by the simultaneous statistical occupancy of Wyckoff sites 2b, 2c and 2d by Mn and Rh (2b: 88% Mn and 12% Rh, 2c: 90% Mn and 4% Rh, 2d: 90% Mn and 5%Rh). This chemical disorder modifies the stoichiometry of the film to $Mn_{1.90} Rh_{1.064} Sn_{1.00}$, i.e., it contains less Mn and more Rh than those films where less chemical disorder is observed and which show magnetic nano-objects. Thus, we conclude that films which show no nano-objects are more chemically disordered than the films presented in this manuscript.

References:

- [1] T. Ma, A. K. Sharma, R. Saha, A. K. Srivastava, P. Werner, P. Vir, V. Kumar, C. Felser, S. S. P. Parkin, *Adv. Mater.* **2020**, 32, 2002043.
- [2] E. Vlieg, and M. Lohmeier, *J. Appl. Cryst.* **1993**, 26, 706.
- [3] C. Schamper, H. L. Meyerheim, and W. W. Moritz, *J. Appl. Cryst.* **1993**, 26, 687.
- [4] E. Vlieg, *J. Appl. Cryst.* **1997**, 30, 532.
- [5] G. M. Sheldrick, *Acta. Cryst* **2015**, C71, 3.

[6] International Tables for Crystallography. Volume A, Space-Group Symmetry. Dordrecht; London: Published for the International Union of Crystallography by Kluwer Academic Publishers, **2002**.

[7] W. F. Kuhs, *Acta Cryst.* **1992**, *A48*, 80.

[8] The unweighted (Ru) and the weighted residuum are given by:

$$Ru = \frac{\sum ||F_o| - |F_c||}{\sum |F_o|} \quad Rw = \sqrt{\frac{\sum [w(F_o^2 - F_c^2)^2]}{\sum [wF_o^2]}}$$

where for short F_o and F_c are the observed and calculated structure factor magnitudes and the summation runs over all reflections (HKL).

6. Observation of Néel skyrmions in metallic PtMnGa

In this chapter, the first observation of Néel skyrmions in a metallic compound PtMnGa is presented. LTEM and MFM measurements were performed on FIB lamellae, both uniform and wedge-shaped, prepared from single crystals of PtMnGa. XRD and HAADF-STEM analysis revealed that PtMnGa has a non-centrosymmetric structure rather than a centrosymmetric structure reported in the literature. This finding, thus, supports the LTEM observation of Néel skyrmions in PtMnGa. LTEM and MFM measurements were performed at various temperatures and magnetic fields. Néel skyrmions in this compound are found to be stable at lower temperatures, and high temperatures up to ~220 K. The skyrmions can also be stabilized in zero magnetic fields using a suitable field-cooling procedure over a broad temperature range as low as 5 K. A strong variation of the skyrmion size on the lamella thickness and magnetic field is reported. Moreover, these skyrmions are highly robust to in-plane magnetic fields of up to 1 T. These properties of Néel skyrmions, together with the possibility of manipulating them in metallic PtMnGa via current-induced spin-orbit torques, make them interesting for future spintronics applications.

The following chapter of this cumulative thesis has been reprinted from my publication (Reprinted from [26]. Link to the Creative Commons license: <https://creativecommons.org/licenses/by/4.0/>):

A. K. Srivastava, P. Devi, **A. K. Sharma***, T. Ma, H. Deniz, H. L. Meyerheim, C. Felser, S. S. P. Parkin. "Observation of robust Néel skyrmions in metallic PtMnGa". *Adv. Mater.* **2019**, 32, 1904327. (*co-first author)

Observation of Robust Néel Skyrmions in Metallic PtMnGa

Abhay K. Srivastava, Parul Devi, Ankit K. Sharma, Tianping Ma, Hakan Deniz, Holger L. Meyerheim, Claudia Felser, and Stuart S. P. Parkin*

Over the past decade the family of chiral noncollinear spin textures has continued to expand with the observation in metallic compounds of Bloch-like skyrmions in several B20 compounds, and antiskyrmions in a tetragonal inverse Heusler. Néel like skyrmions in bulk crystals with broken inversion symmetry have recently been seen in two distinct nonmetallic compounds, GaV_4S_8 and VOSe_2O_5 at low temperatures (below ≈ 13 K) only. Here, the first observation of bulk Néel skyrmions in a metallic compound PtMnGa and, moreover, at high temperatures up to ≈ 220 K is reported. Lorentz transmission electron microscopy reveals the chiral Néel character of the skyrmions. A strong variation is reported of the size of the skyrmions on the thickness of the lamella in which they are confined, varying by a factor of 7 as the thickness is varied from ≈ 90 nm to ≈ 4 μm . Moreover, the skyrmions are highly robust to in-plane magnetic fields and can be stabilized in a zero magnetic field using suitable field-cooling protocols over a very broad temperature range to as low as 5 K. These properties, together with the possibility of manipulating skyrmions in metallic PtMnGa via current induced spin-orbit torques, make them extremely exciting for future spintronic applications.

type Néel structure have been found in two nonmetallic oxides,^[4] although only at very low temperatures. Here we report the first observation of bulk type Néel skyrmions in a metallic compound PtMnGa. Moreover, we directly image the skyrmions in thin lamellae using Lorentz transmission electron microscopy (LTEM). Of especial interest we find that the skyrmions can be stabilized over a wide range of temperature (5–220 K) and magnetic field, as compared to Bloch-skyrmions in B20 compounds. Furthermore, another important difference is that the size of the Néel skyrmions depends on the thickness of the PtMnGa lamella and increases monotonically with the thickness of the lamella. Finally, we show that skyrmions in PtMnGa are robust against large in-plane magnetic fields.

Today there is tremendous interest in chiral noncollinear spin textures that are typically stabilized by vector exchange interactions in non-centrosymmetric structures. Of these spin textures skyrmions and, more recently, antiskyrmions have been the focus of much attention.^[1] Although the latter, to date, have only been observed in a tetragonal inverse Heusler,^[2] skyrmions with a Bloch like character have been found in several metallic cubic B20 compounds^[3] and skyrmions with a bulk

Information) with sizes ranging up to 4 nm. These crystals are metallic (see the Supporting Information). The resistivity versus temperature curve shows a change in slope near ≈ 230 K that corresponds to the Curie temperature where PtMnGa undergoes a transition to a ferromagnetic state that is also clearly seen in magnetization versus temperature data (not shown). Several previous studies have reported models of the crystal structure of PtMnGa.^[5] In these, the atomic structure of PtMnGa was first categorized with a cubic $C1_b$ structure with space group $F43m$ ^[5a,b] but later with a hexagonal Ni_2In -type structure.^[5c,d] In the latter case,^[5d] it was suggested that the Pt, Mn, and Ga atoms are located at Wyckoff sites 2c, 2a, and 2d in the space group $P6_3/mmc$ (Nr.194). Both these structural types are centrosymmetric which is not consistent with our observation of skyrmions. Thus, we have carried out detailed studies to precisely determine the crystal structure of PtMnGa as we now discuss.

From both single-crystal X-ray diffraction (XRD) and high-angle annular dark-field scanning transmission electron microscopy (HAADF-STEM) we find that, although the PtMnGa structure bears a resemblance with the model discussed,^[5d] the actual structure clearly lacks inversion symmetry due to small but significant vertical relaxations of the Pt and Ga atoms along the [0001] direction. This lowers the space group symmetry from $P6_3/mmc$ (Nr. 194) to the polar group $P3m1$ (Nr.156) and, thereby, fulfils the requirement of hosting Néel skyrmions in a non-centrosymmetric crystal structure with point group C_{3v} .^[6]

XRD experiments were carried out on bulk single crystals using $\text{Cu-K}\alpha_1$ radiation. Based on least squares refinement of

A. K. Srivastava, A. K. Sharma, T. Ma, Dr. H. Deniz, Dr. H. L. Meyerheim, Prof. S. S. P. Parkin

Max Planck Institute of Microstructure Physics
Weinberg 2, Halle (Saale) D-06120, Germany
E-mail: stuart.parkin@mpi-halle.mpg.de

A. K. Srivastava, A. K. Sharma, T. Ma, Prof. S. S. P. Parkin
Institute of Physics

Martin Luther University
Halle-Wittenberg, Halle (Saale) D-06120, Germany

Dr. P. Devi,^[†] Prof. C. Felser
Max Planck Institute for Chemical Physics of Solids
Nöthnitzer Straße 40, 01187 Dresden, Germany

 The ORCID identification number(s) for the author(s) of this article can be found under <https://doi.org/10.1002/adma.201904327>.

© 2019 The Authors. Published by WILEY-VCH Verlag GmbH & Co. KGaA, Weinheim. This is an open access article under the terms of the Creative Commons Attribution License, which permits use, distribution and reproduction in any medium, provided the original work is properly cited.

^[†]Present address: Ames Laboratory, Ames, IA, USA

DOI: 10.1002/adma.201904327

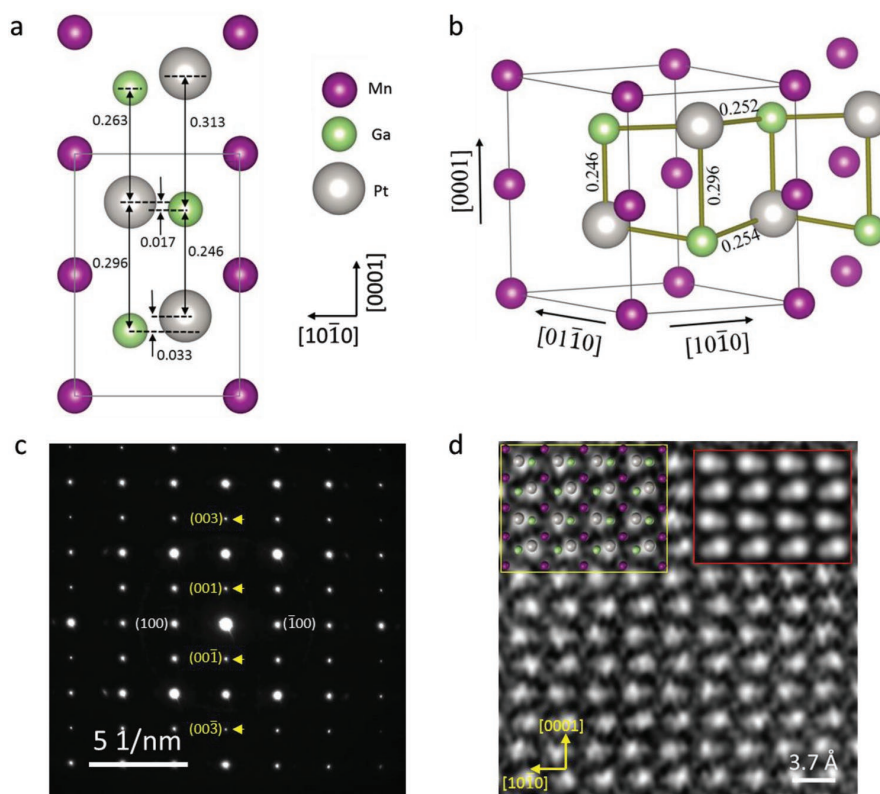


Figure 1. Structure of PtMnGa. a) XRD derived structure model. The unit cell is indicated by the solid lines. Distances along the [0001] directions are given in nanometers. b) Perspective view of the PtMnGa structure c) Selected-area electron diffraction pattern along [0110] orientation of a PtMnGa lamella. The arrows indicate diffraction spots of the type (000L) with $L = 2n + 1$ ($n \in \mathbb{Z}$). d) Experimental HAADF-STEM image showing the atomic arrangements along [0110]. Simulated STEM image (red rectangle) and approximate fitting of atoms (yellow rectangle) is shown for comparison. These measurements were performed at room temperature.

17 symmetry independent reflections, the atomic structure was analyzed to high accuracy. **Figure 1a** shows the atomic arrangement viewed along the [0110] direction. The most important characteristic of the structure is the vertical rumpling within the two Pt–Ga–Pt chains of magnitude 0.017 and 0.033 nm, respectively. A perspective view of the structure is shown in **Figure 1b**. The two Pt (color grey) and two Ga (color green) atoms per unit cell are no longer symmetrically related to each other (*c*-glide plane, 6_3 screw axis), due to a symmetry lowering from $P6_3/mmc$ to $P3m1$, i.e., the structure lacks inversion symmetry. Unambiguous and direct evidence for this conclusion comes from the appearance of reflections, which are forbidden in $P6_3/mmc$, but which are observed in our experiments, albeit with very weak intensity (see the Supporting Information).

Thin lamellae of PtMnGa were prepared from bulk single crystals using focused ion beam techniques (see the Supporting Information). Lamellae that were oriented with the [0110] direction perpendicular to the plane of the lamella were used to determine atomic arrangements using electron diffraction patterns and HAADF-STEM. An experimental electron diffraction pattern obtained from such a lamella is shown in **Figure 1c**. Diffraction spots of the type (000L) (with $L = 2n + 1$, $n \in \mathbb{Z}$),

that are forbidden for group $P6_3/mmc$, can be seen (denoted by arrows). **Figure 1d** shows a magnified experimental HAADF-STEM image along the [0110] crystal direction. Because of its higher atomic number, Pt atoms are more prominent than Mn and Ga atoms. Detailed analysis of this image shows that the spacing between two consecutive atomic rows is not equal. This means that the Pt and Ga atoms are not fixed to the Wyckoff sites 2c and 2d of a Ni_2In -type structure, but instead they are relaxed along the [0001] direction. This relaxation results in lowering the symmetry and making the structure non-centrosymmetric. A simulation of the STEM image based on the structure proposed by XRD is shown (red rectangle) for comparison. It can be seen that the proposed structure fits well with the experimental observations. The yellow rectangle shows an approximate fitting of the atoms onto the STEM image. A detailed analysis of the experimental and simulated STEM images are given in the Supporting Information text and **Figures S1 and S2** in the Supporting Information. A simulation of the electron diffraction patterns and STEM image for group $P6_3/mmc$ is also shown for comparison. These experimental observations confirm that the structure is non-centrosymmetric C_{3v} rather than centrosymmetric Ni_2In -type structure reported in previous studies.

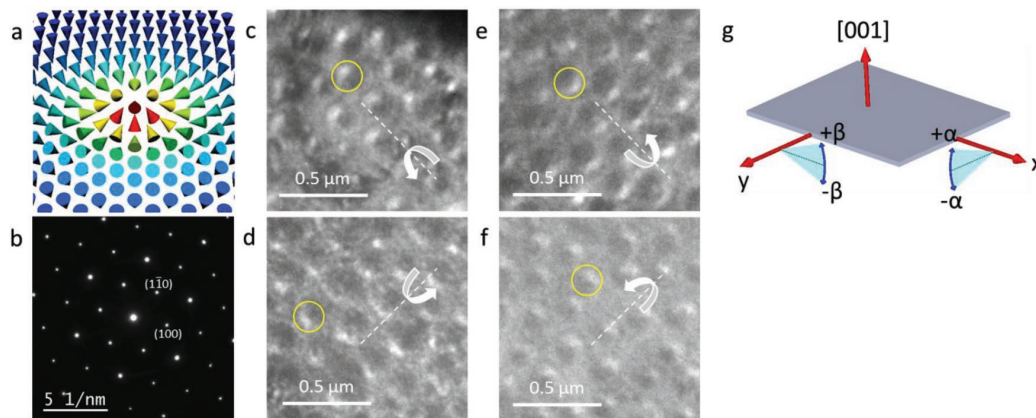


Figure 2. Observation of Néel skyrmions by LTEM. a) Spin texture of a Néel skyrmion. b) Selected-area electron diffraction pattern obtained at room temperature from a [0001] oriented lamella. c–f) Under-focused (1.5 mm) LTEM images recorded at 100 K with tilt angle as follows: c) $\alpha = -9^\circ$, d) $\beta = -19^\circ$, e) $\alpha = +9^\circ$, and f) $\beta = +16^\circ$. These images were recorded under a perpendicular applied field of 0.28 T. The dashed white lines in (c), (d), (e), and (f) represent the tilt axis, curved arrows represent the tilting direction and yellow circles identify a single skyrmion. g) Schematic representation of sample tilting along the x- and y-axes defining positive and negative α and β tilt angles.

LTEM has widely been used in skyrmion related studies due to its high spatial resolution and ability to distinguish various kinds of magnetic topological structures.^[2,3c,7] For a Néel-type skyrmion shown in Figure 2a, where the in-plane component of magnetization is either radially pointing out or pointing in, the total deflection of electrons is always compensated when the electron beam is perpendicular to the sample and hence results in no Lorentz contrast. However, when the sample is tilted, the projection of magnetization around the tilt axis causes an asymmetric deflection of electrons and thereby generates Lorentz contrast.^[7,8] This contrast is composed of half bright and half dark regions and depends on the sign and degree of tilting.^[7,9] Reversing the sign of the sample tilt reverses the contrast. Simulated LTEM images of a Néel skyrmion under different tilting condition are shown in Figure S3 in the Supporting Information.

Thin lamellae, oriented along [0001], were prepared from bulk single crystals using focused ion beam milling (see the Supporting Information), whose thickness was varied from ≈ 90 nm to ≈ 4 μm . Both uniform thickness lamella and wedges were prepared. Figure 2b shows the electron diffraction pattern obtained from a lamella of uniform thickness ≈ 265 nm showing that it is [0001] oriented. The sample was tilted away from the easy axis to generate Lorentz contrast. Tilting the sample along different directions results in changes in the contrast of Néel skyrmions, as mentioned previously. Figure 2c–f shows an alternation from bright to dark contrast of the skyrmions while tilting the sample from $-\alpha$ to $+\alpha$ (along x) or from $-\beta$ to $+\beta$ (along y). A schematic explanation of this sample tilting is shown in Figure 2g. A similar LTEM contrast has been previously observed for a “biskyrmion”^[10] and type-II bubbles.^[11] However, contrast for these spin-textures is found even without any tilt. Thus our observed spin structure is not consistent with a bubble or a Bloch skyrmion.

Detailed temperature and field-dependent LTEM measurements were carried out. We observe both thermodynamically stable Néel skyrmions over a limited temperature region and

metastable Néel skyrmions over a much wider temperature region. The observation of thermodynamically stable Néel skyrmions using LTEM is difficult for the following two main reasons: (i) the magnetic contrast of the sample decreases when approaching magnetic transition temperature ($T_c \approx 225$ K) and in increasing magnetic field, and (ii) the Néel skyrmion generates no contrast without tilting, as mentioned before. Although the sample can be tilted, small tilting does not provide observable contrast and large tilting in zero field with the subsequent application of field will result in an increased in-plane component of the magnetic field which increases the stability of the skyrmions.^[9] Therefore, to observe thermodynamically stable skyrmions, the field was applied along the [0001] direction and then the sample was tilted $\approx 24^\circ$ (high tilting value of 24° was used to obtain better contrast at 220 K). This procedure was done for several different temperatures from 200 to 225 K. At 200 K, no skyrmions were observed and above 220 K we could not observe any LTEM contrast. This means that thermodynamically stable skyrmions exist from ≈ 210 to ≈ 220 K. Figure S5 in the Supporting Information shows such skyrmions at 220 K with poor contrast. This shows that Néel skyrmions in this material are stable in a temperature–magnetic field (T – B) window close to T_c regardless of the field–temperature history. In this T – B window, we find that skyrmions are thermodynamically stable wherein a cycloidal state that is thermodynamically stable in zero magnetic field transforms into Néel skyrmions and then to the field polarized state by applying an increasing magnetic field. Images of the cycloidal phase are shown in Figure S5 in the Supporting Information.

At and below 200 K, a cycloidal state is observed throughout the sample when tilted 10° from the [0001] pole (lower tilting values were used at temperatures below 210 K for all other measurements to avoid stabilization caused by tilting). The absence of contrast in zero tilt establishes their Néel-like cycloidal nature wherein the spins rotate in a plane parallel to the cycloid propagation direction. Video S1 in the Supporting Information shows the contrast generation of such a cycloid

state when the sample is tilted away from the pole. With increasing field the cycloidal state simply transforms to a field polarized state and no skyrmions are observed during this process.

To stabilize Néel skyrmions in a broader temperature and field window, the sample was field cooled from above T_c (from 300 K) with an applied field of 0.096 T along [0001]. A similar field cooling mechanism has previously been used to obtain metastable Bloch-like skyrmions with field cooling.^[12] Néel skyrmions in our system are found to be stable even at zero field after the field cooling process. A small increase in size is observed after field removal. **Figure 3a** shows closely packed skyrmions at 150 K after removal of the external field. As compared to **Figure 2c–f**, an additional contrast can be seen within the skyrmion interior. This is clearly seen in the intensity line profile across one of the skyrmions, as shown in the inset to **Figure 3a**. This additional contrast shows

that there is a uniformly magnetized core (pointing in $-z$) of the skyrmion that is well separated from the outside (pointing in $+z$) by the domain wall boundary. The core is increased in size compared to **Figure 2c–f** due to the lower magnetic field (here zero) so that it is big enough to be resolved by LTEM. **Figure S4** in the Supporting Information shows a simulated LTEM contrast and intensity profile of two skyrmions with different diameters. With an increase in the out of plane field, the core region shrinks and the skyrmion size decreases which is evident from **Figure 3b** and the line profile shown in the inset. For small sized skyrmions it was not possible to resolve the core from the domain wall and therefore these may be considered as skyrmions in which the magnetization direction changes continuously from the centre to the periphery of the skyrmion. A further increase in field results in a field polarized state.

The field and temperature dependence of the skyrmion size was studied in detail. **Figure 3c** shows the measured variation in skyrmion size with magnetic field at different temperatures for a lamella of uniform thickness (≈ 265 nm). For these measurements, the sample was tilted 10° from the pole. Some variation in the skyrmion size is found well above our LTEM resolution, as can be seen from **Figure 3a**, where the average value of the skyrmion diameter and the standard deviation in the size distribution is shown. As the magnetic field is increased the skyrmion sizes become more uniform. A large variation in skyrmion diameter occurs due to quenching of the spin structures after the field cooling process and local interactions between the skyrmions.^[10a,13] The average skyrmion size is found to decrease with increasing temperature and magnetic field. Above 210 K, the decreased magnetic contrast makes it impossible to obtain good LTEM contrast under the same tilting conditions.

Experiments were also performed on wedged samples to study the thickness dependence of the skyrmion phase stability. The dependence of Néel skyrmion size was studied as a function of lamella thickness, using two wedged lamellae W1 and W2 with thicknesses ranging from ≈ 90 to ≈ 260 nm and

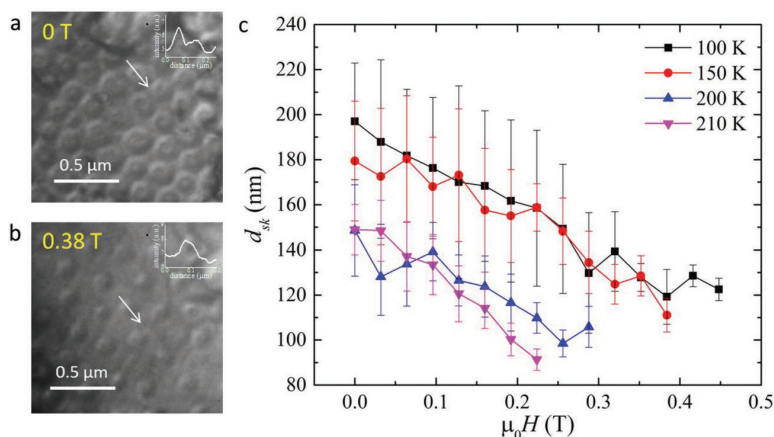


Figure 3. Skyrmion size as a function of magnetic field. a,b) Under-focused (1.2 mm) LTEM images recorded at 0 T (a) and 0.38 T (b) after field cooling in a perpendicular field of 0.096 T. Insets of (a) and (b) show intensity profiles along the direction of the white arrows shown in the figures. These images were taken at 150 K. c) Variation of skyrmion diameter as a function of magnetic field at different temperatures for a sample of uniform thickness (≈ 265 nm).

≈ 200 to ≈ 4000 nm, respectively. Lamella W1 was investigated using LTEM. **Figure S6** in the Supporting Information shows an overview image of the lamella W1 and its thickness profile as determined from electron energy loss spectroscopy (EELS). Without field cooling, cycloid spin spirals are observed and their thickness dependence can be seen in **Figure S7a** in the Supporting Information. The diameter of these spin spirals increases with thickness. The dependence of the cycloid on external magnetic field at 100 K is shown in **Figure S7** in the Supporting Information.

Skyrmions in the wedge lamella W1 were stabilized using the same field cooling process as mentioned before. The average skyrmion size is found to increase with lamella thickness. Three different regions of the wedge lamella A, B, and C (see **Figure S6a** in the Supporting Information) were chosen to measure the skyrmion size. The variation of average skyrmion size with thickness for these three regions are plotted and shown in **Figure S6b** in the Supporting Information. It is important to note that for low thickness, where the size of skyrmion is very small, it was not possible to distinguish the core region. However, as the lamella thickness increases, the skyrmion size also increases showing the core. With increasing field, the skyrmion core becomes smaller and smaller until it is difficult to resolve. This behavior is similar to that we discussed previously for uniform thickness lamellae.

In order to study the magnetic structure at thicknesses beyond those measurable by LTEM, we performed magnetic force microscopy (MFM) measurements on W2. In contrast to LTEM, the out-of-plane component of the magnetization is directly imaged and therefore the chirality of any nano-objects cannot be determined. However, we find that the MFM images obtained using the same protocols as used for LTEM are consistent with chiral Néel skyrmions which have the same size for the same thickness lamella. Thus, in the following we describe these objects observed in the MFM images as Néel skyrmions.

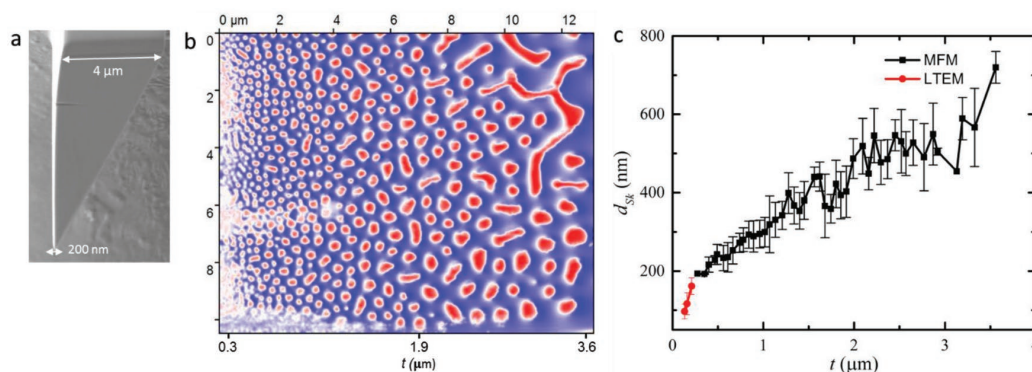


Figure 4. MFM images of Néel skyrmions. a) SEM side view of the wedge-shaped lamella. b) MFM image of Néel skyrmions in wedge W2 in 0.096 T at 100 K. c) Skyrmion diameter as a function of thickness (t) including both MFM and LTEM data.

A scanning electron microscopy image of the lamella W2 is shown in **Figure 4a**. Typical MFM data are summarized in **Figure 4b** after cooling W2 from 300 to 100 K in the presence of a magnetic field $H_{\perp} = 0.096$ T applied perpendicular to the wedge. A skyrmion phase is stabilized over the entire lamella. At large thicknesses the skyrmion phase is mixed with a few cycloids. Note that the direction of the cycloid is not tied to the underlying crystal structure (see **Figure S8d** in the Supporting Information) unlike for example, antiskyrmions.^[2] It is to be noted that the skyrmion size is not homogenous throughout the lamella thickness because of the field cooling process, which is discussed above in **Figure 3** description. However, the average skyrmion size is found to increase with increasing thickness. The average skyrmion size is estimated to be ≈ 190 nm for a thickness of ≈ 250 nm and ≈ 720 nm for a thickness of ≈ 3600 nm. The dependence of skyrmion size on the lamella thickness is summarized in **Figure 4c** and compared with the LTEM data for wedge W1. These data are in good agreement with each other and both sets of data show that there is a very strong dependence of the skyrmion size on lamella thickness. Effect of magnetic field on lamella W2 is shown in **Figure S8** in the Supporting Information.

Reports on Bloch skyrmions in chiral B20 systems, where the skyrmion size is determined by a competition between Heisenberg exchange and Dzyaloshinskii–Moriya Interaction (DMI), show that the skyrmion size is independent of sample

thickness.^[3c,14] However, biskyrmions and type-II bubbles, found in centrosymmetric systems, show a strong dependence on thickness.^[13] In these cases dipole–dipole interactions (DDI) play a very important role which, in general, can be ignored for B20 systems. Here the lower symmetry, that reflects the layered structure of PtMnGa, allows for strong contributions to the energy of the system in the case where the width of the boundary wall of the Néel skyrmion is small compared to the size of the magnetic object. In this case the Néel skyrmions have some “magnetic bubble” like character.^[16]

Since the Néel skyrmions in LTEM can only be observed when the sample is tilted and, consequently, there will always be an in-plane component of the applied field, we carried out studies to explore the stability of the Néel skyrmions in the presence of an in-plane magnetic field using MFM. A uniform lamella with ≈ 900 nm thickness was fabricated for this purpose. First, skyrmions were stabilized at 100 K after the same field cooling process as before and then the out-of-plane field was reduced to zero. Then a pure in-plane field was applied. Observations are shown in **Figure 5a–d**. Skyrmions are found to be stable even up to in-plane fields with large strengths of 1 T. There is a small decrease in contrast at these high in-plane fields.

In conclusion, we have found that PtMnGa has a non-centrosymmetric structure rather than the centrosymmetric structure reported in the literature. Although the structural

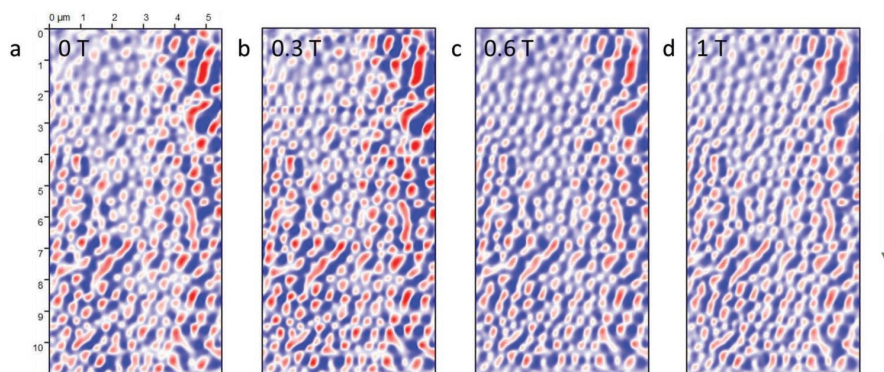


Figure 5. Effect of in-plane magnetic field. a–d) MFM images of metastable Néel skyrmions in a uniform lamella of thickness 900 nm in the presence of an in-plane magnetic field of strength: a) 0 T, b) 0.3 T, c) 0.6 T, and d) 1 T at 100 K. The arrow shows the direction of applied in-plane field.

differences are small, nevertheless, these are very important because they account for the observations that we make of robust Néel skyrmions in this system over a very wide range of temperature. These are the first observation of Néel skyrmions in a metallic system which make them highly interesting for applications in, for example, racetrack memories,^[17] in which Néel type noncollinear spin textures have been shown to be efficiently manipulated using chiral spin torques. Although we have not yet been able to manipulate the Néel skyrmions in these thick layer systems with current in the thick lamella we have used, we anticipate that for ultrathin layers this will be possible in the future. An important finding of our work is the very first observation of a significant dependence of Néel skyrmion size on thickness. Finally, we note that PtMnGa belongs to a large class of highly tunable magnetic metals whose properties can be readily tailored to optimize the skyrmionic properties to enable them to reach their full potential.

(Further details of the crystal structure investigation(s) may be obtained from the Fachinformationszentrum Karlsruhe, 76344 Eggenstein-Leopoldshafen (Germany), on quoting the depository number CSD-1938199)

Supporting Information

Supporting Information is available from the Wiley Online Library or from the author.

Acknowledgements

A.K.S., P.D., A.K.S., and T.M. contributed equally to this work. This project has received funding from the European Research Council (ERC) under the European Union's Horizon 2020 research and innovation program (Grant agreement No 670166) and the Deutsche Forschungsgemeinschaft (DFG, German Research Foundation)—Project number 403505322.

Conflict of Interest

The authors declare no conflict of interest.

Keywords

Lorentz transmission electron microscopy, non-centrosymmetric, skyrmions, spintronics

Received: July 7, 2019

Revised: November 3, 2019

Published online: December 26, 2019

- [1] a) M. Hoffmann, B. Zimmermann, G. P. Müller, D. Schürhoff, N. S. Kiselev, C. Melcher, S. Blügel, *Nat. Commun.* **2017**, *8*, 308; b) S. Huang, C. Zhou, G. Chen, H. Shen, A. K. Schmid, K. Liu, Y. Wu, *Phys. Rev. B* **2017**, *96*, 144412; c) W. Koshibae, N. Nagaosa, *Nat. Commun.* **2016**, *7*, 10542.
- [2] A. K. Nayak, V. Kumar, T. Ma, P. Werner, E. Pippel, R. Sahoo, F. Damay, U. K. Rossler, C. Felser, S. S. P. Parkin, *Nature* **2017**, *548*, 561.

- [3] a) S. Muhlbauer, B. Binz, F. Jonietz, C. Pfleiderer, A. Rosch, A. Neubauer, R. Georgii, P. Boni, *Science* **2009**, *323*, 915; b) N. Kanazawa, Y. Onose, T. Arima, D. Okuyama, K. Ohoyama, S. Wakimoto, K. Kakurai, S. Ishiwata, Y. Tokura, *Phys. Rev. Lett.* **2011**, *106*, 156603; c) X. Z. Yu, N. Kanazawa, Y. Onose, K. Kimoto, W. Z. Zhang, S. Ishiwata, Y. Matsui, Y. Tokura, *Nat. Mater.* **2010**, *10*, 106.
- [4] a) I. Kezsmarki, S. Bordacs, P. Milde, E. Neuber, L. M. Eng, J. S. White, H. M. Ronnow, C. D. Dewhurst, M. Mochizuki, K. Yanai, H. Nakamura, D. Ehlers, V. Tsurkan, A. Loidl, *Nat. Mater.* **2015**, *14*, 1116; b) T. Kurumaji, T. Nakajima, V. Ukleev, A. Feoktystov, T. H. Arima, K. Kakurai, Y. Tokura, *Phys. Rev. Lett.* **2017**, *119*, 237201.
- [5] a) R. A. Dunlap, S. Jha, H. H. Seyoum, G. M. Julian, R. A. Pappas, J. W. Blue, *Hyperfine Interact.* **1983**, *16*, 689; b) F. A. Hames, J. Crangle, *J. Appl. Phys.* **1971**, *42*, 1336; c) K. H. J. Buschow, P. G. van Engen, *Phys. Status Solidi A* **1983**, *76*, 615; d) K. H. J. Buschow, D. B. De Mooij, *J. Less-Common Met.* **1984**, *99*, 125.
- [6] a) A. Bogdanov, D. A. Yablonski, *J. Exp. Theor. Phys.* **1989**, *68*, 101; b) A. Bogdanov, A. Hubert, *J. Magn. Magn. Mater.* **1994**, *138*, 255.
- [7] S. D. Pollard, J. A. Garlow, J. Yu, Z. Wang, Y. Zhu, H. Yang, *Nat. Commun.* **2017**, *8*, 14761.
- [8] J. Cui, Y. Yao, X. Shen, Y. G. Wang, R. C. Yu, *J. Magn. Magn. Mater.* **2018**, *454*, 304.
- [9] S. Zhang, J. Zhang, Y. Wen, E. M. Chudnovsky, X. Zhang, *Commun. Phys.* **2018**, *1*, 36.
- [10] a) L. Peng, Y. Zhang, W. Wang, M. He, L. Li, B. Ding, J. Li, Y. Sun, X. G. Zhang, J. Cai, S. Wang, G. Wu, B. Shen, *Nano Lett.* **2017**, *17*, 7075; b) W. Wang, Y. Zhang, G. Xu, L. Peng, B. Ding, Y. Wang, Z. Hou, X. Zhang, X. Li, E. Liu, S. Wang, J. Cai, F. Wang, J. Li, F. Hu, G. Wu, B. Shen, X. X. Zhang, *Adv. Mater.* **2016**, *28*, 6887; c) X. Z. Yu, Y. Tokunaga, Y. Kaneko, W. Z. Zhang, K. Kimoto, Y. Matsui, Y. Taguchi, Y. Tokura, *Nat. Commun.* **2014**, *5*, 3198.
- [11] a) J. C. Loudon, A. C. Twitchett-Harrison, D. Cortes-Ortuno, M. T. Birch, L. A. Turnbull, A. Stefancic, F. Y. Ogrin, E. O. Burgos-Parra, N. Bukin, A. Laurenson, H. Popescu, M. Beg, O. Hovorka, H. Fangohr, P. A. Midgley, G. Balakrishnan, P. D. Hatton, *Adv. Mater.* **2019**, *31*, e1806598; b) Y. Yao, B. Ding, J. Cui, X. Shen, Y. Wang, W. Wang, R. Yu, *Appl. Phys. Lett.* **2019**, *114*, 102404.
- [12] a) K. Karube, J. S. White, N. Reynolds, J. L. Gavilano, H. Oike, A. Kikkawa, F. Kagawa, Y. Tokunaga, H. M. Ronnow, Y. Tokura, Y. Taguchi, *Nat. Mater.* **2016**, *15*, 1237; b) P. Milde, D. Köhler, J. Seidel, L. M. Eng, A. Bauer, A. Chacon, J. Kindervater, S. Mühlbauer, C. Pfleiderer, S. Buhandt, C. Schütte, A. Rosch, *Science* **2013**, *340*, 1076; c) H. Oike, A. Kikkawa, N. Kanazawa, Y. Taguchi, M. Kawasaki, Y. Tokura, F. Kagawa, *Nat. Phys.* **2015**, *12*, 62.
- [13] a) S. Woo, K. Litzius, B. Krüger, M.-Y. Im, L. Caretta, K. Richter, M. Mann, A. Krone, R. M. Reeve, M. Weigand, P. Agrawal, I. Lemesch, M.-A. Mawass, P. Fischer, M. Kläui, G. S. D. Beach, *Nat. Mater.* **2016**, *15*, 501; b) K. Karube, J. S. White, D. Morikawa, M. Bartkowiak, A. Kikkawa, Y. Tokunaga, T. Arima, H. M. Ronnow, Y. Tokura, Y. Taguchi, *Phys. Rev. Mater.* **2017**, *1*, 074405.
- [14] H. S. Park, X. Yu, S. Aizawa, T. Tanigaki, T. Akashi, Y. Takahashi, T. Matsuda, N. Kanazawa, Y. Onose, D. Shindo, A. Tonomura, Y. Tokura, *Nat. Nanotechnol.* **2014**, *9*, 337.
- [15] a) H. Nakajima, H. Kawase, K. Kurushima, A. Kotani, T. Kimura, S. Mori, *Phys. Rev. B* **2017**, *96*, 024431; b) X. Z. Yu, Y. Tokunaga, Y. Kaneko, W. Z. Zhang, K. Kimoto, Y. Matsui, Y. Taguchi, Y. Tokura, *Nat. Commun.* **2014**, *5*, 3198.
- [16] W. Jiang, P. Upadhyaya, W. Zhang, G. Yu, M. B. Jungfleisch, F. Y. Fradin, J. E. Pearson, Y. Tserkovnyak, K. L. Wang, O. Heinonen, S. G. te Velthuis, A. Hoffmann, *Science* **2015**, *349*, 283.
- [17] S. S. P. Parkin, M. Hayashi, L. Thomas, *Science* **2008**, *320*, 190.

Copyright WILEY-VCH Verlag GmbH & Co. KGaA, 69469 Weinheim, Germany, 2019.

ADVANCED MATERIALS

Supporting Information

for *Adv. Mater.*, DOI: 10.1002/adma.201904327

Observation of Robust Néel Skyrmions in Metallic PtMnGa

*Abhay K. Srivastava, Parul Devi, Ankit K. Sharma, Tianping Ma, Hakan Deniz, Holger L. Meyerheim, Claudia Felser, and Stuart S. P. Parkin**

Supporting Information

Observation of Robust Néel Skyrmions in Metallic PtMnGa

*Abhay K. Srivastava, Parul Devi, Ankit K. Sharma, Tianping Ma, Hakan Deniz, Holger L. Meyerheim, Claudia Felser & Stuart S.P. Parkin**

Synthesis of single crystal

Single crystals of MnPtGa were grown from a melt using the vertical Bridgman crystal growth technique. First, polycrystalline ingots of PtMnGa were prepared using induction melting technique with the stoichiometric mixture of Mn, Pt and Ga pieces of 99.99% purity which was annealed for three days at 900°C, followed by quenching in an ice-water mixture. Then the crushed precursor pieces were placed in a custom-designed sharp-edged alumina tube and finally sealed inside a tantalum tube with argon atmosphere. The temperature profile for crystal growth was controlled using the thermocouple attached at the bottom of the tantalum ampoule containing the sample. The sample was heated to 1150 °C hold there for 12 hours and then slowly pulled to the temperature 900 °C with a rate of 0.8 mm/h. Single crystallinity was confirmed by white-beam backscattering Laue X-ray diffraction technique at room temperature. The sample shows very sharp spots that can be indexed by a single pattern, which reveals excellent quality of the grown crystals without any twinning or domain.

Lamella preparation by focused ion beam (FIB)

For LTEM, MFM, electron diffraction and STEM measurements, several uniform and wedge shaped lamellas were prepared from two different single crystals of PtMnGa after detailed XRD measurements on one of these crystal. Lamellas were prepared using Ga⁺ focused ion

beam (FIB) system TESCAN GAIA 3 operating in the range of 0.5-30 keV ion beam energy. Standard lift-out procedure was used to extract lamellas from bulk single crystals. Lamella was transferred to TEM copper grids using nano-manipulator needle in the FIB and then polished to desired shape, size and thickness. Finally, a low energy ion beam (3-5 keV) polishing procedure was applied to reduce the surface damage layer caused by Ga⁺ implantation.

To make sure the observed properties are not caused by Ga⁺ ion implantation, two different lamellas in [0001] and [01 $\bar{1}$ 0] orientation were prepared using Xe plasma FIB system TESCAN FERA 3 operating in the range of 3-30 keV ion beam energy. Lamella oriented along [0001] was used for LTEM investigations and [01 $\bar{1}$ 0] was used for electron diffraction and STEM. A similar polishing procedure was used in the end to reduce damage layer.

For MFM measurements, lamella was transferred from the copper grid to a pre-patterned substrate to be easily accessible by the MFM tip.

Transmission electron microscopy (TEM)

FEI TITAN 80-300 electron microscope operating at accelerating voltage of 300 keV equipped with probe corrector and mono-chromator was used for TEM, HAADF-STEM and LTEM measurements. For HAADF-STEM measurements, condenser aperture of 15 mrad was used. Thickness profile of wedge TEM lamella was obtained using EELS which uses log-ratio method to determine local thickness (t) using the formula $t/\lambda = \ln(I_t/I_0)$, where λ is inelastic mean free path for the material, I_t is total area of spectrum and I_0 is area under zero loss peak. For LTEM, current of the objective lens was changed to apply perpendicular magnetic field on the sample. A double tilt holder with liquid nitrogen cooling option was used for measurements at different temperatures.

Magnetic force microscopy (MFM)

All MFM experiments were carried out in an attocube liquid cryostat system equipped with a 2D vector superconducting magnet. A magnetic tip from Nanosensors (SSS-MFMR) was used for all measurements. The soft coating on the magnetic tip ensures the low disturbance of magnetic samples (low moment tip for non-perturbative imaging with high spatial resolution). The high mechanical quality factor ($Q > 30000$) accounts for high force sensitivity under UHV conditions. The tip was magnetized in negative z direction by a permanent magnet.

Dual scanning comprise of topographic and magnetic scan is used to separate atomic and magnetic forces. The tip first interacts with the sample in tapping mode and acquire surface topography. Then the tip is lifted up (60-80 nm) above the sample surface during the second scan to allow the imaging of magnetic interactions. A great care was taken to eliminate tip-induced artefacts and perturbations. The cantilever is oscillated at its resonant frequency. The magnetic tip interacts with the stray field of the sample and experiences a magnetic force gradient, which causes the change in the resonance frequency of the cantilever. The frequency shift (Δf) can be detected in one of the following ways: phase modulation and frequency modulation. We use phase detection owing to its large signal-to-noise ratio and ease of use.

X-Ray Diffraction Analysis

The atomic structure of the PtMnGa crystal was analyzed by x-ray diffraction (XRD) using a Bruker D8 four-circle diffractometer operated with Cu- $K_{\alpha 1}$ radiation. In total the integrated intensity of 17 symmetry independent reflections were collected by performing φ -scans around the sample normal of the $(11\bar{2}0)$ oriented single crystal. Uncertainties (1σ) were estimated based on the quadrature sum of the statistical uncertainty and the reproducibility of symmetry equivalent reflections, which was found to lie in the 15% range.

Integrated intensities were corrected for instrumental factors (Lorentz-, polarization, effective area, absorption) to derive the observed structure factor intensities ($|F_{\text{obs}}(\text{HKL})|^2$).^[1] The

crystal structure was found to be trigonal [space group P3m1 (Nr. 156)] with lattice parameters $a_0=b_0=0.435$ nm and $c_0=0.559$ nm. The assignment of the crystal structure to the non-centrosymmetric space group P3m1 rather than to the centrosymmetric space group P6₃/mmc (Nr. 194) in Ref ^[2] is *primarily* based on the observation of different types of reflections, which are systematically absent in P6₃/mmc but which are not forbidden in space group P3m1. These are: (i) type (000L) with $L=2n+1$, (ii) type (HH $\bar{2}\bar{H}$ L) with $L=(2n+1)$ and (iii) HKIL with $H-K=3n+1$ and $H-K=3n+2$ (n =integer in all cases). The intensity of these "forbidden" reflections is typically in the (sub) percent range as compared to those, which are allowed in both space groups. A summary of the observed and calculated structure factor intensities based on the structure model is given in Table S1. We emphasize that even when using the "P6₃/mmc allowed" reflections only, the fit for the P3m1 symmetry structure model (see below) is significantly better than that for PtMnGa in the Ni₂In structure.

The structure refinement was carried out by least squares refinement of the z-positions of the atoms located at the Wyckoff positions 1a (Mn), 1b (Pt, Ga) and 1c (Ga, Pt) using the programs "Prometheus" and "SHELX".^[3,4] The fit quality is quantified by the goodness of fit (GOF) and the un-weighted residuum (Ru) which was found to be 1.2 (GOF) and 0.11 (Ru),^[5,6] values which are very satisfactory.

Figure 1 b of main text shows the structure in a perspective view emphasizing the Pt-Ga zig-zag chains. As compared to the ideal Ni₂In structure (P6₃/mmc), the Pt and Ga atoms are relaxed along the [0001] direction out of the positions $z=1/4$ and $z=3/4$. Thus, the height difference between Pt and the Ga atoms located at $(x, y) = (1/3, 2/3)$ and $(2/3, 1/3)$ is equal to 0.51 for Ga and 0.47 lattice units in c_0 (LU, 1 LU=0.559 nm) for Pt, i.e. it is different from $1/2$. This is decisive structural detail which lifts the inversion symmetry. In space group P3m1 the two Pt and Ga atoms within the unit cell are no longer symmetry related to each other by a c-glide plane and the 6₃ screw axis as in space group P6₃/mmc.

The structure is characterized by a vertical rumpling of 0.033 nm and 0.017 nm between the Pt- and Ga atoms in the two chains along the $[11\bar{2}0]$ direction. This involves an alternating vertical Pt-Ga distance of 0.296 nm and 0.263 nm in one of the two Pt-Ga-Mn vertical rows and of 0.246 and 0.313 nm in the other (we estimate the uncertainty of the distance determination to lie in the 0.05 to 0.1 Å range). Other Pt-Ga distances are equal to 0.254 and 0.252 nm, which compared to the sum of the atomic radii 2.70 Å ^[7] is reduced by 7% which can be attributed to the lower coordination number (here four instead of 12 and 6 in metallic Pt and Ga, respectively) and to some ionicity of the bond. Owing to its relatively low scattering power, Mn was kept fixed at $(x,y,z) = (0,0,0)$ and $(0,0,1/2)$ throughout the analysis. Interatomic distances between Mn and Pt, Ga lie in the range between 2.68 Å and 2.91 Å. In addition, an overall atomic displacement factor (ADP) was refined to $\langle u \rangle^2 = 0.04 \pm 0.01$ Å² while extinction was found not to be important.

Table S1. Experimental $|F_{\text{obs}}(\text{HKL})|^2$ and calculated $|F_{\text{calc}}(\text{HKL})|^2$ squared structure factor magnitudes based on the structure model shown in Figure 1. Bold letters indicate observed reflections, which are forbidden in space group $P6_3/\text{mmc}$.

H K L	$ F_{\text{obs}}(\text{HKL}) ^2$	$ F_{\text{calc}}(\text{HKL}) ^2$
0 0 1	196.59	180.80
0 1 1	6840.50	5999.50
0 2 1	2750.74	2577.01
-1 1 0	2646.92	2518.25
-1 1 1	3647.66	4349.99
-1 1 2	16313.61	11653.70
-1 2 0	29582.05	28119.56
-1 2 1	124.15	85.47
0 0 3	518.51	654.83

-1 3 0	649.65	614.80
-2 2 1	2081.43	3479.31
-2 2 2	3779.58	2752.53
0 2 2	4448.76	5720.66
-1 2 2	6201.97	8002.20
-2 2 0	1419.61	1180.43
-2 3 1	2616.53	1623.58
-1 2 4	2441.26	2914.10

HAADF-STEM analysis

A cif (crystal information file) was created based on the XRD measurement results. We used this cif to simulate electron diffraction pattern and HAADF-STEM images using the programs CrystalMaker[®] [8] and STEM-WinHREM[™] [9, 10] respectively. Figure S1 shows simulated electron diffraction pattern of a (01 $\bar{1}$ 0) oriented crystal of PtMnGa on the basis of the space group P3m1 (a) and for the Ni₂In-type structure with space group P6₃/mmc (b), respectively. Reflections of the type (000L) with L=2n+1 (n integer) that are forbidden for P6₃/mmc are observed in Figure S1 a. Simulated STEM images for both space groups along (01 $\bar{1}$ 0) are shown in Figure S1 c and d. Red and yellow rectangles are used to emphasize the spacing between two consecutive atomic rows along the [0001] direction. In close agreement with the x-ray diffraction analysis the width of these two rectangles are different, here related to a vertical distance of 0.2667 and 0.2917 nm between a column of Pt and Ga atoms. This proves the relaxation of Pt and Ga atoms along [0001], breaking the inversion symmetry. In space group P6₃/mmc related to the Ni₂In-type structure the distance between Ga and Pt would be

equal. Structural image shown in Figure S1 e and f were generated from cif using the program VESTA.^[11]

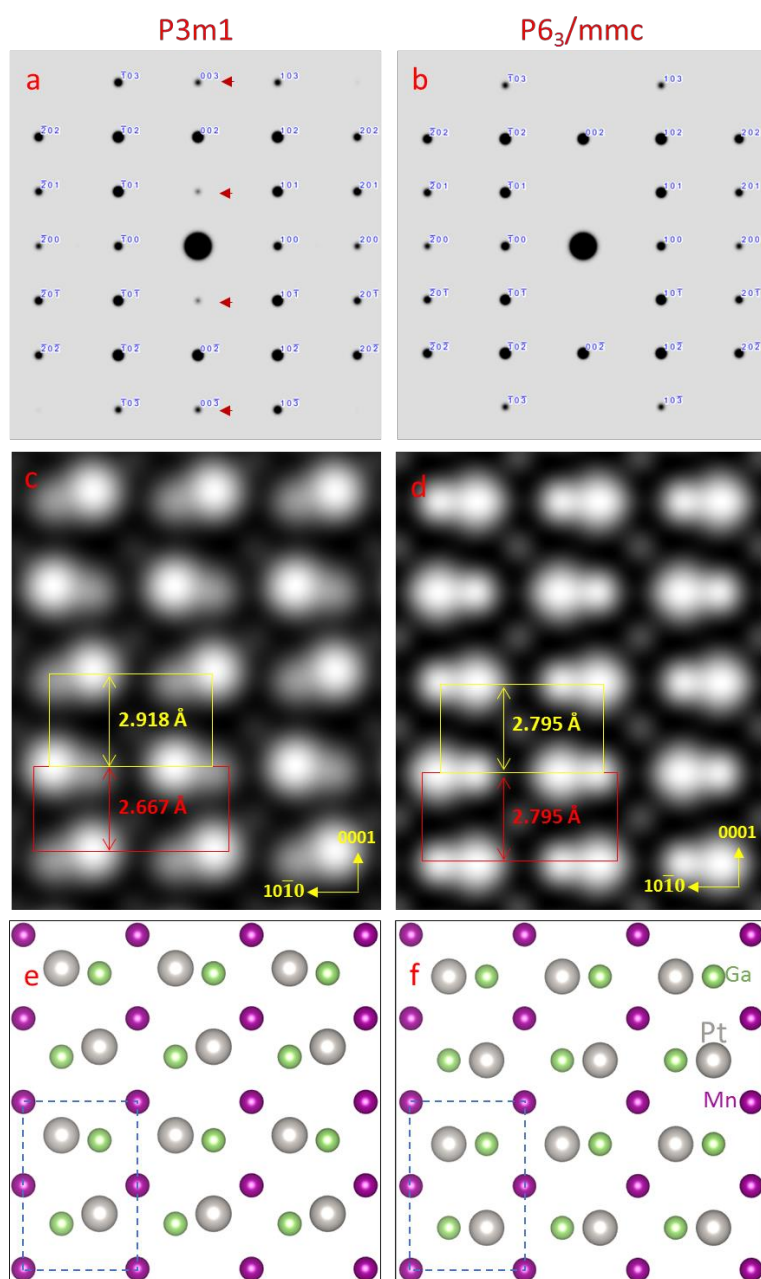


Figure S1. (a) and (b) Simulated electron diffraction patterns and (c) and (d) simulated STEM images for PtMnGa on the basis of space group $P3m1$ and $P6_3/mmc$, respectively. Red arrows in (a) indicate the reflections of type $(000L)$ with $L=2n+1$ (n integer) which are

forbidden in $P6_3/mmc$. Red and yellow rectangles in (c) and (d) are used to emphasize the vertical distance between Pt and Ga atoms along $[0001]$. Atomic arrangement for the two structures are outlined in (e) and (f). Dashed rectangle defines the unit cell.

A magnified experimental high-resolution HAADF-STEM image of a $(01\bar{1}0)$ oriented crystal is shown in Figure S2 a. In order to filter the instrumentally related noise induced by the scanning, the image was filtered with a low pass Fourier filter with a cut off at 0.083 nm^{-1} (12 nm^{-1}) to reduce this noise and the result is shown in Figure S2 b. Magnified view of a small portion from Figure S2 b is shown in Figure S2 c. It can be seen that spacing between consecutive atomic rows are different which results from the relaxation of Pt and Ga atoms along $[0001]$. Distance between two atoms was measured by counting the number of pixels. Numbers are approximate as it is not possible to identify the exact center of Pt atoms but it is clear that spacing between consecutive Pt atoms are different. We find remarkable agreement with the x-ray diffraction result for one type of Pt-Ga-Pt row.

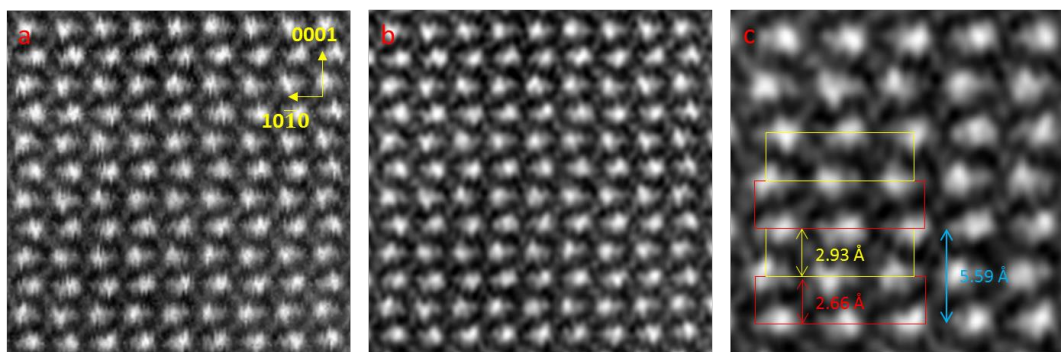


Figure S2. Experimental HAADF-STEM image of $(01\bar{1}0)$ oriented sample (a) unfiltered, (b) filtered. (c) Magnified view from (b). Red and yellow rectangles are used to emphasize that spacing between consecutive rows are different.

LTEM image simulations

Micromagnetic simulation software OOMMF^[12] with included DMI extension^[13] was used to generate magnetization configurations for Néel skyrmion. This configuration was used with MALTS^[14] to generate simulated LTEM contrast. Figure S3 shows simulated over-focused LTEM contrast for two Néel Skyrmions of different diameters versus tilt angle. It is important to note that there is no contrast without tilting and that the contrast increases with tilt angle. For the first case, where skyrmion size is small, LTEM contrast appears as a combination of half bright and half dark spots. However, when the uniformly magnetized core of skyrmion is large enough to be resolved, its LTEM contrast changes. A separate contrast emerges inside its center as shown.

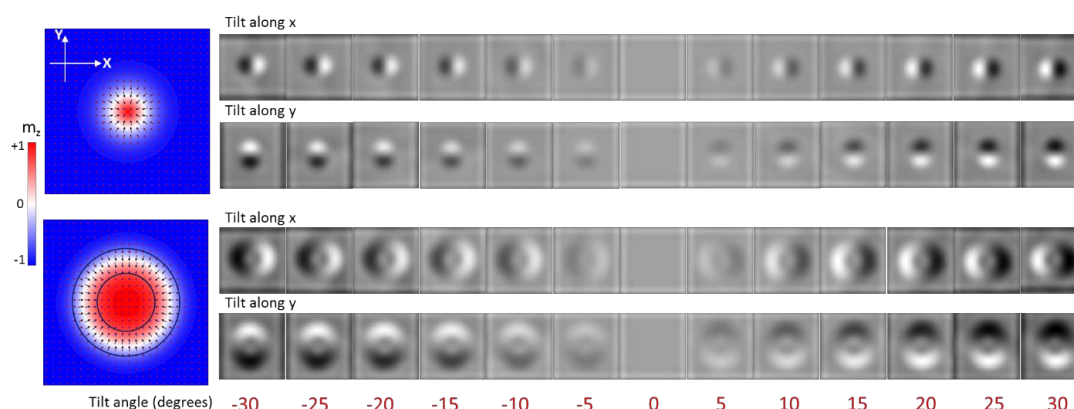


Figure S3. Simulated LTEM contrast for skyrmions of different diameters versus tilt angle in degrees along the x- and y-axis. The colors code represents the out of plane component of magnetization and black arrows shows in-plane components.

Figure S4 shows intensity line profile of LTEM contrast for differently sized skyrmions. The tiny bump between maximum and minimum intensity represents the core of skyrmion.

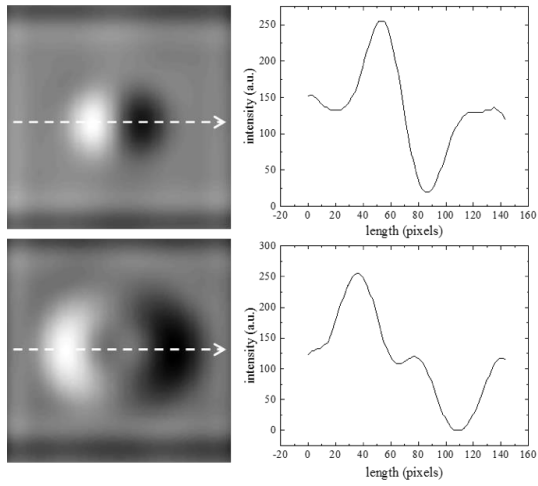


Figure S4. Intensity line profile of the LTEM contrast along the direction of arrow.

Thermodynamically stable Néel Skyrmions with LTEM

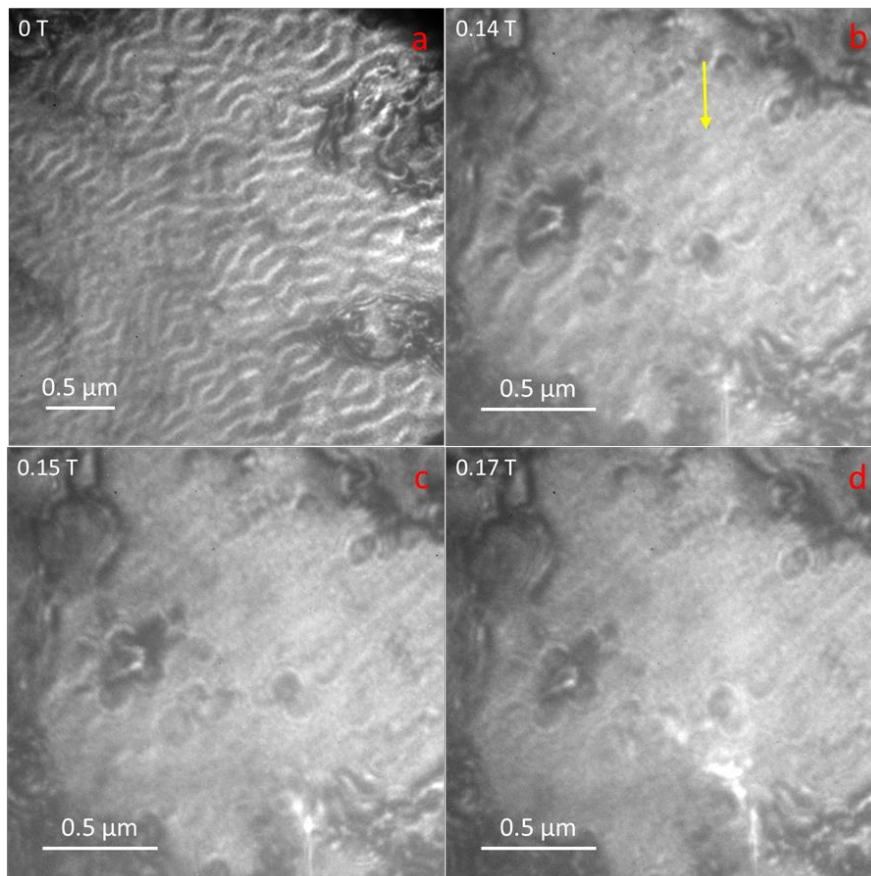


Figure S5. (a) Cycloidal state under zero field and (b) Thermodynamically stable Neel skyrmions at 0.14 T observed after sample tilting by 24°. Field was applied along [0001] direction followed by tilting. Arrow is used to show skyrmions with poor contrast. (c, d) field increased to transform skyrmion to field polarized state. These images were taken at 220 K.

Measurement of skyrmion size

An image processing software was programmed in MATLAB to measure the size of skyrmions in uniform and wedge lamellae. For the uniform lamella a region of area $2 \times 2 \mu\text{m}$ was carefully chosen to measure the skyrmion size. Approximately 15 to 20 skyrmions were measured at lower fields and 5-6 skyrmions at higher fields. For a particular field the average value of the skyrmion diameter and the standard distribution in the size is used. A similar procedure was used for the wedge lamellae.

Thickness map

Thickness mapping of the (0001) oriented wedge lamella was obtained from Electron Energy Loss Spectroscopy (EELS) measurements shown in Figure S6. Three rectangular regions of size $0.5 \times 1.0 \mu\text{m}$ and different thickness were chosen for calculation of skyrmion diameters. Regions are named as A, B and C as shown in the figure.

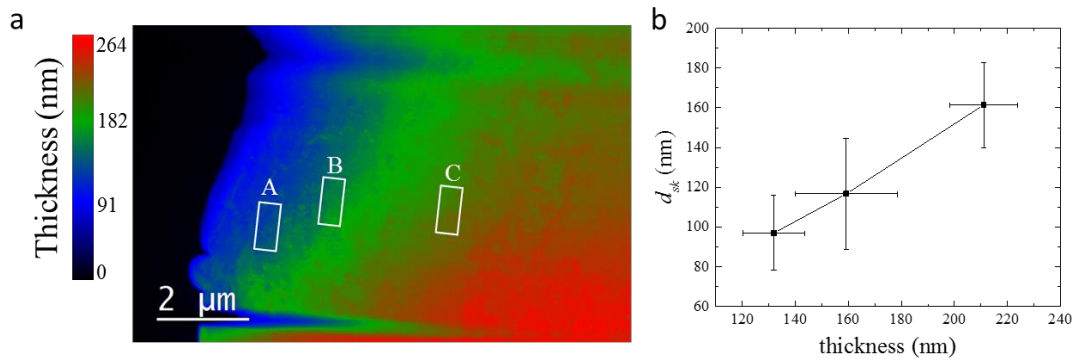


Figure S6. (a) Thickness mapping of wedge-shaped lamella obtained from EELS measurements. White rectangles marked as A, B and C show the chosen region of different thickness, (b) skyrmion diameter as a function of thickness for the three regions shown in (a).

LTEM experiments

Effect of externally applied magnetic field on stripe domains in a wedge-shaped lamella is shown in Figure S7. Without field cooling, no skyrmions were observed with increasing magnetic field. Stripes simply expand and transform to a field polarized state.

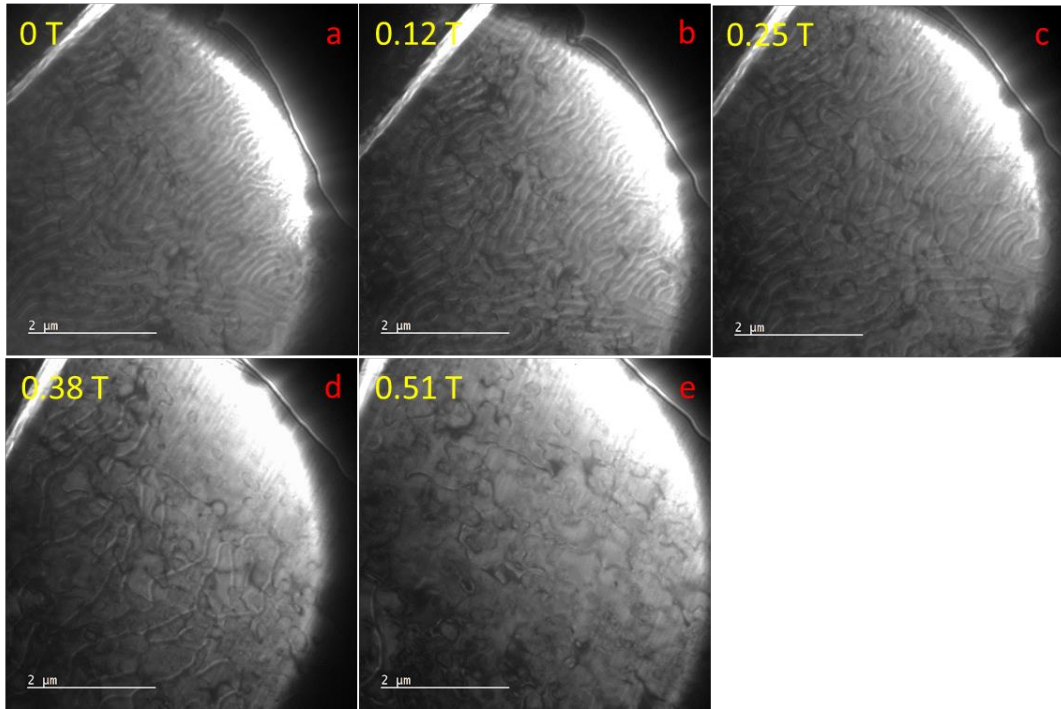


Figure S7. Effect of increasing magnetic field on cycloids. All the images were recorded after 10° tilt at 100 K without any field cooling process.

MFM experiments

Magnetic field dependence of Néel skyrmions in a wedge-shaped lamella is shown in Figure S8. All images are recorded at 100 K. In the case of field cooling, skyrmions of varying size are stabilized over the large thickness in the whole lamella. Figure S8 a shows an MFM image in 0.15 T. As the field is increased, the skyrmions start saturating in large thickness region first and eventually field polarized state is achieved, as shown in Figure S8 b-c. However, in zero field cooling, skyrmions are not stabilized but a stripe domain phase is observed, which is shown in Figure S8 d.

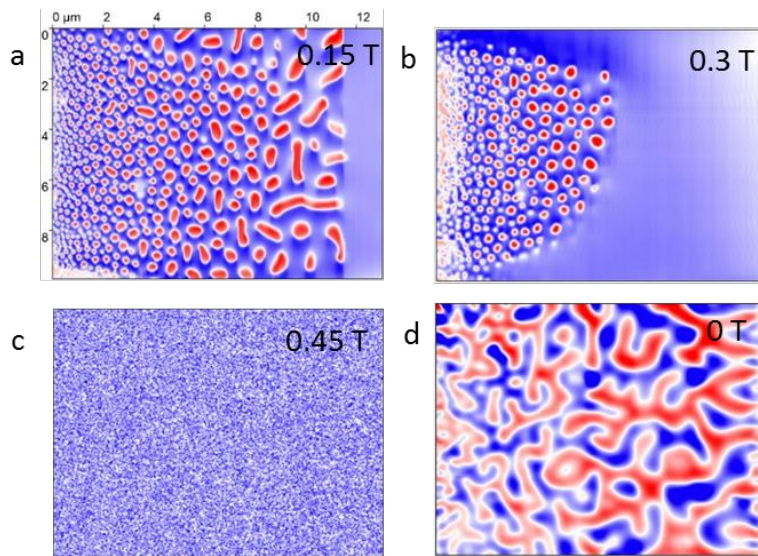


Figure S8. Magnetic field dependence of skyrmions. (a)-(d) MFM images in 0.15 T, 0.3 T, 0.45 T and zero field in lamella W2. Scale bar is same for all images and is shown in (a).

The skyrmions are stable even at low temperature. Figure S9 shows metastable skyrmions phase in a uniform lamella at 5 K in the presence of 0.096 T.

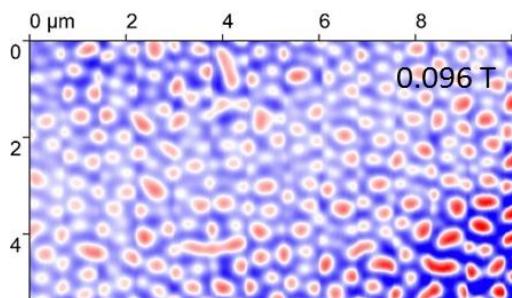


Figure S9. Skyrmion phase in a uniform lamella at 5 K in 0.096 T.

Resistivity measurements

A rectangular bar of the single crystal was used for transport measurements to measure its resistivity. A standard four-probe-in-line method (current and voltage leads placed along a

line) was employed where current was applied in the basal plane (perpendicular to the 0001 axis). A clear anomaly can be seen at ~ 235 K that is consistent with a magnetic transition into a ferromagnetic state. This transition was clearly observed in magnetization data at the same temperature.

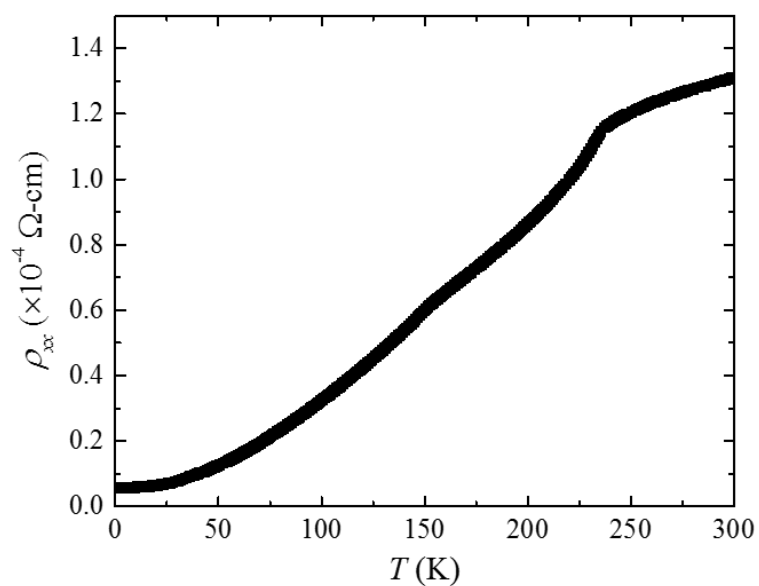


Figure S10. Longitudinal resistivity ρ_{xx} versus temperature.

References:

- [1] W.H Zachariasen. Theory of X-Ray Diffraction in Crystals, Dover Publications, New York (1994)
- [2] K.H.J. Buschow and D.B. de Mooij. Crystal structure and magnetic properties of PtMnGa and PtMnAl. Journal of the Less Common Metals, **99**, 125-130 (1984)

- [3] Zucker, U. H., Perenthaler, E., Kuhs, W. F., Bachmann, R. & Schulz, H. (1983). PROMETHEUS. A program system for investigation of anharmonic thermal vibrations in crystals. *J. Appl. Cryst.* **16**, 358.
- [4] G.M. Sheldrick (2015) Crystal structure refinement with SHELXL, *Acta Cryst.*, **C71**, 3-8
- [5] R_u is defined as $R_u = \frac{\sum ||F_{obs}| - |F_{calc}||}{\sum |F_{obs}|}$, where the sum runs over all reflections. R_u represents the average relative deviation between the calculated (calc) and the experimental (obs) structure factor magnitudes.
- [6] $GOF = \{1/(N-P)\sum[(|F_{obs}|^2 - |F_{calc}|^2)/\sigma^2]\}^{1/2}$, where N and P are the number of reflections and free parameters, respectively and σ is the standard deviation of $|F_{obs}|^2$. The summation runs over all reflections. See also: Abrahams, S. Indicators of accuracy in structure factor measurement. *Acta Crystallographica Section A* **25**, 165-173 (1969).
- [7] J. C. Slater, Atomic Radii in Crystals. *J. Chem. Phys.* **41**, 3199 (1964).
- [8] CrystalMaker Software, <http://www.crystallmaker.com/>.
- [9] <http://www.hremresearch.com/Eng/simulation.html>.
- [10] Ishizuka, K. A practical approach for STEM image simulation based on the FFT multislice method. *Ultramicroscopy* **90**, 71 (2002).
- [11] Momma, K. and Izumi, F. VESTA 3 for three-dimensional visualization of crystal, volumetric and morphology data. *J. Appl. Crystallogr.*, **44**, 1272-1276 (2011).
- [12] Donahue, M. J. & Porter, D. G. OOMMF User's Guide, version 1.0, Interagency Report NISTIR 6376 (National Institute of Standards and Technology, Gaithersburg, 1999); available at <http://math.nist.gov/oommf>.
- [13] Rohart, S. & Thiaville, A. Skyrmion confinement in ultrathin film nanostructures in the presence of Dzyaloshinskii–Moriya interaction. *Phys. Rev. B* **88**, 184422 (2013).

[14] Walton, S. K. *et al.* MALTS: A tool to simulate Lorentz Transmission Electron Microscopy from micromagnetic simulations. *IEEE Trans. Magn.* **49**, 4795–4800 (2013).

7. Conclusion and outlook

7.1 Conclusion

In this thesis, non-collinear spin textures have been investigated in bulk and thin films of compounds with non-centrosymmetric crystal structures using variable temperature magnetic force microscopy. The main findings of this thesis are summarized below.

1. Tunable antiskyrmion in $\text{Mn}_{1.4}\text{PtSn}$ crystal

The wide range of tunability of the helical period and the size of antiskyrmions in thin lamellae of $\text{Mn}_{1.4}\text{PtSn}$ single crystals with D_{2d} symmetry is observed. In this compound, the magneto-dipolar interaction plays an important role in influencing the size scale of the non-collinear spin textures within this compound. The wide range of tunability of the size of the antiskyrmion and the corresponding helical period in the D_{2d} system makes these materials particularly interesting for applications. For example, in racetrack memory devices [10, 11], the size of anti-skyrmions could be locally adjusted to make them easier to read and to create by adjusting the thickness of the racetrack spatially. This result also clearly shows how the size of anti-skyrmions can be tuned by manipulating their magnetization rather than the DMI. For example, by chemical doping, by using materials with the strong temperature dependence of magnetization, or by the use of ferrimagnets or synthetic antiferromagnets, thereby opening up a new direction in the field of chiraltronics.

2. Non-collinear spin textures in Mn_2RhSn thin films

Nano-scale spin textures are observed in thin films of [001] oriented Mn_2RhSn using MFM and compared with those observed in a single crystalline lamella using LTEM. We find that the stability region of nano-objects with respect to temperature and the magnetic field is extensive and similar in both cases. In neither case are well-ordered arrays of the magnetic nano-objects found. However, a labyrinth domain structure is observed in the thin film, in contrast to the bulk lamella where a helical structure is found under similar field-temperature conditions. We find evidence of a small increase in the size of the magnetic nano-objects with increasing film thickness, but which is a much smaller variation than previously seen in a related Heusler compound with D_{2d} symmetry [21]. This suggests that magnetostatic energy plays a less important role in Mn_2RhSn , which we attribute to its comparatively lower magnetization. Detailed X-ray structural studies of the thin films suggest that there is chemical inhomogeneity that may account for the absence of a helical phase and the large size variation of the magnetic nano-objects. In films that had even greater degrees of chemical inhomogeneity no magnetic nano-objects were seen nor was the labyrinth phase found, providing further evidence that the observation of well-defined spin textures in thin Heusler films requires highly chemically ordered films.

Our studies suggest that the nano-objects we have found in thin films of Mn_2RhSn are likely Bloch skyrmions or antiskyrmions, that we observe in the single-crystalline lamella of the same material. Moreover, we have demonstrated that individual nano-objects can be deleted or created by local magnetic fields. Our work paves the way to the realization of skyrmionic devices based on Heusler thin films.

3. Observation of Néel skyrmion in PtMnGa crystal

The first observation of Néel skyrmions in a metallic compound PtMnGa is reported. It is found that PtMnGa has a non-centrosymmetric structure rather than the centrosymmetric

structure reported in the literature. In comparison with the previously reported structure, although the structural differences are small, nevertheless, these are very crucial because they account for the observations of Néel skyrmions in this compound. Néel skyrmions are found to be stable over a very wide range of temperatures and can be stabilized even at zero fields following a proper field cooling method. The skyrmion size shows a strong dependence on temperature and magnetic field. Moreover, MFM studies reveal that there is a strong variation of the skyrmion size with thicknesses up to ~ 3600 nm. In addition, the highly robust nature of skyrmions to in-plane magnetic fields is another important highlight of this work.

7.2 Outlook

The results presented in this thesis will play an important role in realizing the following:

- **To realize high levels of chemical ordering in thin films of Heusler compounds:** It typically requires high temperatures, as is used, for example, in the growth of high-quality single crystals of Heusler compounds. One method that has been shown to give rise to chemical ordering at temperatures as low as even room temperature for binary Heusler compounds is the chemical templating (CTL) method [93]. It is of great interest to explore this method in the future and see whether it can be extended to ternary Heuslers.
- **To grow ultra-thin D_{2d} Heusler films for the current-driven motion of antiskyrmions:** To date, we have not seen any significant motion of antiskyrmionic objects in lamellae from volume spin-transfer torques generated by a current passed directly through them. Therefore, the current-driven motion of non-collinear

nanoscale objects in ultra-thin films driven by spin-orbit torques can be explored by combining these films with layers in which there is a significant charge to spin conversion [22, 41, 94].

List of publications

Thesis related publications:

1. **A. K. Sharma**, J. Jena, K. G. Rana, A. Markou, H. L. Meyerheim, K. Mohseni, A. K. Srivastava, I. Kostanoskiy, C. Felser, S. S. P. Parkin. “Nanoscale non-collinear spin textures in thin films of a D_{2d} Heusler compound”. *Adv. Mater.* **2021**, 2101323.
2. T. Ma, **A. K. Sharma***, R. Saha, A. K. Srivastava, P. Werner, P. Vir, V. Kumar, C. Felser, S. S. P. Parkin. “Tunable Magnetic Antiskyrmion Size and Helical Period from Nanometers to Micrometers in a D_{2d} Heusler Compound”. *Adv. Mater.* **2020**, 32, 2002043. (*co-first author)
3. A. K. Srivastava, P. Devi, **A. K. Sharma***, T. Ma, H. Deniz, H. L. Meyerheim, C. Felser, S. S. P. Parkin. “Observation of robust Néel skyrmions in metallic PtMnGa”. *Adv. Mater.* **2019**, 32, 1904327. (*co-first author)

Other publications during Ph.D.:

4. A. Chakraborty, A. K. Srivastava, A. K. Sharma*, A. K. Gopi, K. Mohseni, A. Ernst, H. Deniz, B. K. Hazra, S. Das, P. Sessi, I. Kostanovskiy, T. Ma, H. L. Meyerheim, S. S. P. Parkin. “Magnetic Skyrmions in a Thickness Tunable 2D Ferromagnet from a Defect Driven Dzyaloshinskii–Moriya Interaction”. *Adv. Mater.* **2022**, 2108637. (*co-first author)
5. Y. He, T. Helm, I. Soldatov, S. Schneider, A. K. Srivastava, A. K. Sharma, J. Kroder, W. Schnelle, R. Schaefer, B. Rellinghaus, G. H. Fecher, S. S. P. Parkin, C. Felser. “Nanoscale magnetic bubbles in Nd₂Fe₁₄B at room temperature”, *Phys. Rev. B* **2022**.
6. H. Han, A. Sharma, H. L. Meyerheim, J. Yoon, H. Deniz, K. Jeon, A. K. Sharma, K. Mohseni, C. Guillemard, M. Valvidares, P. Gargiani, S. S. P. Parkin. “Control of Oxygen Vacancy Ordering in Brownmillerite Thin Films via Ionic Liquid Gating”. *ACS Nano* **2022**.
7. S. Galeski, T. Ehmcke, R. Wawrzyńczak, P. M. Lozano, K. Cho, A. K. Sharma, S. Das, F. Küster, P. Sessi, M. Brando, R. Küchler, A. Markou, M. König, P. Swekis, C. Felser, Y. Sassa, Q. Li, G. Gu, M. V. Zimmermann, O. Ivashko, D.I. Gorbunov, S. Zherlitsyn, T. Förster, S. S. P. Parkin, J. Wosnitza, T. Meng, J. Gooth. “Origin of the quasi-quantized Hall effect in ZrTe₅”. *Nat. Commun.* **2021**, 12, 3197.

8. H. Han, A. Sharma, J. Yoon, Z. Wang, **A. K. Sharma**, Y. Zhuang, H. Deniz, S. H. Yang, C. Körner, G. Woltersdorf, S. S. P. Parkin. “Meta-surfaces formed from continuous oxide layers via local electrolyte gating” (submitted).

Author contributions

Chapter 4: T. Ma, **A. K. Sharma**, R. Saha, and A. K. Srivastava contributed equally to this work [21]. FIB lamellae were prepared by A. K. Srivastava. MFM measurements and data analysis was done by A. K. Sharma. T. Ma contributed to the theory part of the work and programmed LTEM-MFM image analysis software. LTEM measurements were performed by R. Saha. P. Vir and V. Kumar prepared the bulk crystals under the supervision of C. Felser at the Max Planck Institute for Chemical Physics of Solids, Dresden. All measurements were performed at the Max Planck Institute of Microstructure Physics, Halle, Germany. S. S. P. Parkin supervised the project.

Chapter 5: **A. K. Sharma** and J. Jena contributed equally to this work [27]. MFM measurements and data analysis was done by A. K. Sharma. LTEM measurements were performed by J. Jena. K. G. Rana and A. Markou prepared the thin films at the Max Planck Institute for Chemical Physics of Solids, Dresden. H. L. Meyerheim and K. Mohseni performed XRD measurements. I. Kostanoskiy performed RBS measurements. All measurements were performed at the Max Planck Institute of Microstructure Physics, Halle, Germany. A. K. Sharma and J. Jena wrote the manuscript under the supervision of S. S. P. Parkin.

Chapter 6: A. K. Srivastava, P. Devi, and **A. K. Sharma** contributed equally to this work [26]. A. K. Srivastava performed LTEM measurements and prepared FIB lamellae. MFM measurements were done by A. K. Sharma. Bulk crystals were prepared by P. Devi at the Max Planck Institute for Chemical Physics of Solids, Dresden. H. L. Meyerheim performed XRD measurements. All measurements were performed at the Max Planck Institute of Microstructure Physics, Halle, Germany. S. S. P. Parkin supervised the project.

References

1. Coughlin, T.M., *Fundamentals of Hard Disk Drives*, in *Digital Storage in Consumer Electronics*. 2018, Springer. p. 25-44.
2. Parkin, S.S.P., R. Bhadra, and K.P. Roche, *Oscillatory magnetic exchange coupling through thin copper layers*. *Physical Review Letters*, 1991. **66**(16): p. 2152-2155.
3. Parkin, S.S., N. More, and K.P. Roche, *Oscillations in exchange coupling and magnetoresistance in metallic superlattice structures: Co/Ru, Co/Cr, and Fe/Cr*. *Phys Rev Lett*, 1990. **64**(19): p. 2304-2307.
4. Parkin, S.S., *Systematic variation of the strength and oscillation period of indirect magnetic exchange coupling through the 3d, 4d, and 5d transition metals*. *Phys Rev Lett*, 1991. **67**(25): p. 3598-3601.
5. Parkin, S., et al., *Magnetically engineered spintronic sensors and memory*. *Proceedings of the IEEE*, 2003. **91**(5): p. 661-680.
6. Parkin, S., *Giant magnetoresistance in magnetic nanostructures*. *Annual Review of Materials Science*, 1995. **25**(1): p. 357-388.
7. Parkin, S., et al., *Exchange-biased magnetic tunnel junctions and application to nonvolatile magnetic random access memory*. *Journal of Applied Physics*, 1999. **85**(8): p. 5828-5833.
8. Parkin, S.S., et al., *Giant tunnelling magnetoresistance at room temperature with MgO (100) tunnel barriers*. *Nature materials*, 2004. **3**(12): p. 862-867.
9. Weller, D. and A. Moser, *Thermal effect limits in ultrahigh-density magnetic recording*. *IEEE Transactions on magnetics*, 1999. **35**(6): p. 4423-4439.
10. Parkin, S.S., M. Hayashi, and L. Thomas, *Magnetic domain-wall racetrack memory*. *Science*, 2008. **320**(5873): p. 190-194.
11. Parkin, S. and S.-H. Yang, *Memory on the racetrack*. *Nature nanotechnology*, 2015. **10**(3): p. 195-198.
12. Fert, A., V. Cros, and J. Sampaio, *Skyrmions on the track*. *Nature nanotechnology*, 2013. **8**(3): p. 152.
13. Sampaio, J., et al., *Nucleation, stability and current-induced motion of isolated magnetic skyrmions in nanostructures*. *Nature nanotechnology*, 2013. **8**(11): p. 839.

14. Mühlbauer, S., et al., *Skyrmion lattice in a chiral magnet*. Science, 2009. **323**(5916): p. 915.
15. Jonietz, F., et al., *Spin Transfer Torques in MnSi at Ultralow Current Densities*. Science, 2010. **330**(6011): p. 1648.
16. Yu, X., et al., *Skyrmion flow near room temperature in an ultralow current density*. Nature communications, 2012. **3**: p. 988.
17. Jiang, W., et al., *Direct observation of the skyrmion Hall effect*. Nature Physics, 2017. **13**(2): p. 162.
18. Litzius, K., et al., *Skyrmion Hall effect revealed by direct time-resolved X-ray microscopy*. Nature Physics, 2017. **13**(2): p. 170.
19. Zhang, S., et al., *Topological computation based on direct magnetic logic communication*. Sci Rep, 2015. **5**: p. 15773.
20. Nayak, A.K., et al., *Magnetic antiskyrmions above room temperature in tetragonal Heusler materials*. Nature, 2017. **548**(7669): p. 561.
21. Ma, T., et al., *Tunable Magnetic Antiskyrmion Size and Helical Period from Nanometers to Micrometers in a D_{2d} Heusler Compound*. Advanced Materials, 2020: p. 2002043.
22. Huang, S., et al., *Stabilization and current-induced motion of antiskyrmion in the presence of anisotropic Dzyaloshinskii-Moriya interaction*. Physical Review B, 2017. **96**(14): p. 144412.
23. Jena, J., et al., *Evolution and competition between chiral spin textures in nanostripes with D_{2d} symmetry*. Sci. Adv., 2020. **6**: p. abc0723.
24. Jena, J., et al., *Elliptical Bloch skyrmion chiral twins in an antiskyrmion system*. Nature Communications, 2020. **11**(1): p. 1115.
25. Peng, L., et al., *Controlled transformation of skyrmions and antiskyrmions in a non-centrosymmetric magnet*. Nature Nanotechnology, 2020. **15**: p. 181.
26. Srivastava, A.K., et al., *Observation of Robust Néel Skyrmions in Metallic PtMnGa*. Advanced Materials, 2020. **32**(7): p. 1904327.
27. Sharma, A.K., et al., *Nanoscale Noncollinear Spin Textures in Thin Films of a D_{2d} Heusler Compound*. Adv Mater, 2021: p. e2101323.
28. Moriya, T., *Anisotropic superexchange interaction and weak ferromagnetism*. Physical Review, 1960. **120**(1): p. 91.
29. Dzyaloshinsky, I., *A thermodynamic theory of “weak” ferromagnetism of antiferromagnetics*. Journal of Physics and Chemistry of Solids, 1958. **4**(4): p. 241.

30. Hubert, A. and R. Schäfer, *Magnetic domains: the analysis of magnetic microstructures*. 2008: Springer Science & Business Media.
31. Malozemoff, A. and J. Slonczewski, *Magnetic domain walls in bubble materials: advances in materials and device research*. Vol. 1. 2016: Academic press.
32. Thiaville, A., et al., *Dynamics of Dzyaloshinskii domain walls in ultrathin magnetic films*. EPL (Europhysics Letters), 2012. **100**(5): p. 57002.
33. Emori, S., et al., *Current-driven dynamics of chiral ferromagnetic domain walls*. Nat Mater, 2013. **12**(7): p. 611-6.
34. Benitez, M.J., et al., *Magnetic microscopy and topological stability of homochiral Néel domain walls in a Pt/Co/AlOx trilayer*. Nature Communications, 2015. **6**: p. 8957.
35. Neubauer, A., et al., *Topological Hall effect in the A phase of MnSi*. Physical review letters, 2009. **102**(18): p. 186602.
36. Yu, X., et al., *Real-space observation of a two-dimensional skyrmion crystal*. Nature, 2010. **465**(7300): p. 901.
37. Yu, X.Z., et al., *Near room-temperature formation of a skyrmion crystal in thin-films of the helimagnet FeGe*. Nature Materials, 2010. **10**: p. 106.
38. Romming, N., et al., *Writing and deleting single magnetic skyrmions*. Science, 2013. **341**(6146): p. 636.
39. Boulle, O., et al., *Room-temperature chiral magnetic skyrmions in ultrathin magnetic nanostructures*. Nat Nanotechnol, 2016. **11**(5): p. 449-54.
40. Moreau-Luchaire, C., et al., *Additive interfacial chiral interaction in multilayers for stabilization of small individual skyrmions at room temperature*. Nature nanotechnology, 2016. **11**(5): p. 444.
41. Woo, S., et al., *Observation of room-temperature magnetic skyrmions and their current-driven dynamics in ultrathin metallic ferromagnets*. Nature materials, 2016. **15**(5): p. 501.
42. Soumyanarayanan, A., et al., *Tunable room-temperature magnetic skyrmions in Ir/Fe/Co/Pt multilayers*. Nature Materials, 2017. **16**: p. 898.
43. Kezsmarki, I., et al., *Neel-type skyrmion lattice with confined orientation in the polar magnetic semiconductor GaV₄S₈*. Nature Materials, 2015. **14**(11): p. 1116-22.
44. Kurumaji, T., et al., *Neel-Type Skyrmion Lattice in the Tetragonal Polar Magnet VOSe₂O₅*. Phys Rev Lett, 2017. **119**(23): p. 237201.

45. Jena, J., et al., *Observation of Magnetic Antiskyrmions in the Low Magnetization Ferrimagnet $Mn_2Rh_{0.95}Ir_{0.05}Sn$* . Nano Letters, 2019. **20**(1): p. 59.
46. Saha, R., et al., *Intrinsic stability of magnetic anti-skyrmions in the tetragonal inverse Heusler compound $Mn_{1.4}Pt_{0.9}Pd_{0.1}Sn$* . Nature communications, 2019. **10**(1): p. 5305.
47. Karube, K., et al., *Room-temperature antiskyrmions and sawtooth surface textures in a non-centrosymmetric magnet with $S4$ symmetry*. Nat Mater, 2021. **20**(3): p. 335-340.
48. Bogdanov, A.N. and D. Yablonskii, *Thermodynamically stable “vortices” in magnetically ordered crystals. The mixed state of magnets*. Zh. Eksp. Teor. Fiz, 1989. **95**(1): p. 178.
49. Bogdanov, A. and A. Hubert, *Thermodynamically stable magnetic vortex states in magnetic crystals*. Journal of Magnetism and Magnetic Materials, 1994. **138**(3): p. 255-269.
50. Rössler, U.K., A.N. Bogdanov, and C. Pfleiderer, *Spontaneous skyrmion ground states in magnetic metals*. Nature, 2006. **442**(7104): p. 797-801.
51. Lin, Y., P. Grundy, and E. Giess, *Bubble domains in magnetostatically coupled garnet films*. Applied Physics Letters, 1973. **23**(8): p. 485.
52. Garel, T. and S. Doniach, *Phase transitions with spontaneous modulation—the dipolar Ising ferromagnet*. Physical Review B, 1982. **26**(1): p. 325.
53. Takao, S., *A study of magnetization distribution of submicron bubbles in sputtered Ho-Co thin films*. Journal of magnetism and magnetic materials, 1983. **31**: p. 1009.
54. Heinze, S., et al., *Spontaneous atomic-scale magnetic skyrmion lattice in two dimensions*. Nature Physics, 2011. **7**(9): p. 713.
55. Okubo, T., S. Chung, and H. Kawamura, *Multiple- q states and the skyrmion lattice of the triangular-lattice Heisenberg antiferromagnet under magnetic fields*. Physical review letters, 2012. **108**(1): p. 017206.
56. Yu, X., et al., *Magnetic stripes and skyrmions with helicity reversals*. Proceedings of the National Academy of Sciences, 2012. **109**(23): p. 8856-8860.
57. Yu, X., et al., *Biskyrmion states and their current-driven motion in a layered manganite*. Nature communications, 2014. **5**: p. 3198.
58. Loudon, J.C., et al., *Do Images of Biskyrmions Show Type-II Bubbles?* Adv Mater, 2019. **31**(16): p. e1806598.

59. Khanh, N.D., et al., *Nanometric square skyrmion lattice in a centrosymmetric tetragonal magnet*. Nature Nanotechnology, 2020: p. 444.
60. Correspondent, A., *Solid State: Hard and Soft Bubbles*. Nature, 1972. **240**(5378): p. 184.
61. Milde, P., et al., *Unwinding of a skyrmion lattice by magnetic monopoles*. Science, 2013. **340**(6136): p. 1076-80.
62. Jiang, W., et al., *Blowing magnetic skyrmion bubbles*. Science, 2015. **349**(6245): p. 283-286.
63. Chen, G., et al., *Room temperature skyrmion ground state stabilized through interlayer exchange coupling*. Applied Physics Letters, 2015. **106**(24): p. 242404.
64. Dovzhenko, Y., et al., *Magnetostatic twists in room-temperature skyrmions explored by nitrogen-vacancy center spin texture reconstruction*. Nat Commun, 2018. **9**(1): p. 2712.
65. Nagaosa, N. and Y. Tokura, *Topological properties and dynamics of magnetic skyrmions*. Nature nanotechnology, 2013. **8**(12): p. 899.
66. Bruno, P., V. Dugaev, and M. Taillefumier, *Topological Hall effect and Berry phase in magnetic nanostructures*. Physical review letters, 2004. **93**(9): p. 096806.
67. Li, Y., et al., *Robust formation of Skyrmions and topological Hall effect anomaly in epitaxial thin films of MnSi*. Phys Rev Lett, 2013. **110**(11): p. 117202.
68. Rana, K., et al., *Observation of topological Hall effect in Mn₂RhSn films*. New J. Phys., 2016. **18**(8): p. 085007.
69. Sivakumar, P.K., et al., *Topological Hall Signatures of Two Chiral Spin Textures Hosted in a Single Tetragonal Inverse Heusler Thin Film*. ACS Nano, 2020. **14**(10): p. 13463-13469.
70. Maccariello, D., et al., *Electrical detection of single magnetic skyrmions in metallic multilayers at room temperature*. Nature nanotechnology, 2018. **13**(3): p. 233.
71. Pfleiderer, C. and A. Rosch, *Single skyrmions spotted*. Nature, 2010. **465**(7300): p. 880-881.
72. Huang, S. and C. Chien, *Extended skyrmion phase in epitaxial FeGe (111) thin films*. Physical review letters, 2012. **108**(26): p. 267201.
73. Seki, S., et al., *Observation of skyrmions in a multiferroic material*. Science, 2012. **336**(6078): p. 198-201.

74. Shibata, K., et al., *Towards control of the size and helicity of skyrmions in helimagnetic alloys by spin-orbit coupling*. Nature nanotechnology, 2013. **8**(10): p. 723.
75. Yu, X., et al., *Variation of skyrmion forms and their stability in MnSi thin plates*. Physical Review B, 2015. **91**(5): p. 054411.
76. Iwasaki, J., M. Mochizuki, and N. Nagaosa, *Current-induced skyrmion dynamics in constricted geometries*. Nature nanotechnology, 2013. **8**(10): p. 742.
77. Bogdanov, A., et al., *Magnetic structures and reorientation transitions in noncentrosymmetric uniaxial antiferromagnets*. Physical Review B, 2002. **66**(21): p. 214410.
78. Vasyukov, D., et al., *A scanning superconducting quantum interference device with single electron spin sensitivity*. Nature nanotechnology, 2013. **8**(9): p. 639-644.
79. Göddenhenrich, T., et al., *Magnetic force microscopy of domain wall stray fields on single-crystal iron whiskers*. Applied physics letters, 1990. **56**(25): p. 2578-2580.
80. Moser, A., et al., *Observation of single vortices condensed into a vortex-glass phase by magnetic force microscopy*. Physical review letters, 1995. **74**(10): p. 1847.
81. Giessibl, F.J., *Advances in atomic force microscopy*. Reviews of modern physics, 2003. **75**(3): p. 949.
82. Binnig, G., C.F. Quate, and C. Gerber, *Atomic Force Microscope*. Physical Review Letters, 1986. **56**(9): p. 930-933.
83. Giessibl, F.J., *Forces and frequency shifts in atomic-resolution dynamic-force microscopy*. Physical Review B, 1997. **56**(24): p. 16010-16015.
84. Park, H.S., et al., *Observation of the magnetic flux and three-dimensional structure of skyrmion lattices by electron holography*. Nat Nanotechnol, 2014. **9**(5): p. 337-42.
85. Zheng, F., et al., *Experimental observation of chiral magnetic bobbars in B20-type FeGe*. Nature Nanotechnology, 2018. **13**(6): p. 451.
86. Málek, Z. and V. Kamborský, *On the theory of the domain structure of thin films of magnetically uni-axial materials*. Czechoslovakij fiziceskij zurnal, 1958. **8**(4): p. 416-421.
87. Cape, J.A. and G.W. Lehman, *Magnetic Domain Structures in Thin Uniaxial Plates with Perpendicular Easy Axis*. Journal of Applied Physics, 1971. **42**(13): p. 5732-5756.

88. Grundy, P. and S. Herd, *Lorentz microscopy of bubble domains and changes in domain wall state in hexaferrites*. *physica status solidi (a)*, 1973. **20**(1): p. 295-307.
89. Chen, G., et al., *Tailoring the chirality of magnetic domain walls by interface engineering*. *Nat Commun*, 2013. **4**: p. 2671.
90. Chen, G., et al., *Novel chiral magnetic domain wall structure in Fe/Ni/Cu(001) films*. *Phys Rev Lett*, 2013. **110**(17): p. 177204.
91. Lemesh, I., F. Büttner, and G.S.D. Beach, *Accurate model of the stripe domain phase of perpendicularly magnetized multilayers*. *Physical Review B*, 2017. **95**(17): p. 174423.
92. Buttner, F., I. Lemesh, and G.S.D. Beach, *Theory of isolated magnetic skyrmions: From fundamentals to room temperature applications*. *Sci Rep*, 2018. **8**(1): p. 4464.
93. Filippou, P.C., et al., *Chiral domain wall motion in unit-cell thick perpendicularly magnetized Heusler films prepared by chemical templating*. *Nat Commun*, 2018. **9**(1): p. 4653.
94. Ryu, K.-S., et al., *Chiral spin torque at magnetic domain walls*. *Nature nanotechnology*, 2013. **8**(7): p. 527-533.

List of figures

Fig. 1.1: Magnetic domain-wall and skyrmion racetrack memory.....	3
Fig. 1.2: Outline figure of the experimental results.....	7
Fig. 2.1: Heisenberg interaction.....	10
Fig. 2.2: Sketch of domain walls in perpendicularly magnetized film.....	12
Fig. 2.3: Spin configuration of magnetic skyrmion.....	14
Fig. 2.4: Sketch of DMI.....	17
Fig. 2.5: Electrical detection of skyrmions utilizing the topological Hall effect (THE).....	20
Fig. 2.6: Experimental observation of Bloch skyrmion in B20 alloys.....	23
Fig. 2.7: Experimental observation of Néel skyrmion at the interface of Fe and Ir (111).....	24
Fig. 2.8: Experimental observation of antiskyrmion in $Mn_{1.4}Pt_{0.9}Pd_{0.1}Sn$	26
Fig. 3.1: Schematic of the MFM tip and sample interaction.....	29
Fig. 3.2: Typical MFM image.....	31
Fig. 3.3: Images of the MFM system.....	33
Fig. 3.4: FIB systems.....	36
Fig. 3.5: FIB prepared wedge lamella.....	37
Fig. 3.6: Lamellae for MFM measurements.....	38
Fig. 3.7: LTEM system (TITAN 80-300 from FEI).....	40

Abbreviations

AFM	Atomic force microscopy
DMI	Dzyaloshinskii-Moriya interaction
DW	Domain wall
FIB	Focused ion beam
GMR	Giant magnetoresistance
HDD	Hard disk drives
LTEM	Lorentz transmission electron microscopy
MFM	Magnetic force microscopy
MOKE	Magneto-optical Kerr effect
MRAM	Magnetic random-access memory
MTJ	Magnetic tunnel junctions
MTXM	Magnetic transmission soft X-ray microscopy
NV	Nitrogen-vacancy
PMA	Perpendicular magnetic anisotropy
RBS	Rutherford backscattering spectrometry
RM	Racetrack memory
SANS	Small angle neutron scattering
SHE	Skymion Hall effect
SOC	Spin-orbit coupling
SPLEEM	Spin-polarized low-energy electron microscopy
SP-STM	Spin-polarized scanning tunneling microscopy
SQUID	Scanning superconducting quantum interference device
TEM	Transmission electron microscopy
THE	Topological Hall effect
VTI	Variable temperature insert
XMCD-PEEM	Photoemission electron microscopy combined with X-ray magnetic circular dichroism
XPS	X-ray photoelectron spectroscopy
XRD	X-ray diffraction

Acknowledgments

First of all, I would like to thank my supervisor Prof. Dr. Stuart S.P. Parkin for his guidance, motivation, and constant support throughout my Ph.D. He was always available for discussing new ideas with positive energy. His kind behavior made him easily approachable for any kind of scientific discussion or meeting. He gave me enough freedom to plan a new experiment or involve in other research projects at the institute, which helped me immensely to carry out my research work smoothly. I have been very fortunate to have him as a supervisor.

I would also like to thank my colleagues Abhay Kant Srivastava, Jagannath Jena, Kumari Gaurav Rana, Ajaya Kumar Nayak, Tianping Ma, Rana Saha, Holger Meyerheim, Katayoon Mohseni, Ilya Kostanovski, and Hakan Deniz from Max Planck Institute for Microstructure Physics, Halle who have been involved in the research projects presented in this thesis.

I would like to extend my gratitude to other scientists and colleagues at the institute with whom I always enjoyed fruitful discussions and got important feedback: Dirk Sander, Peter Werner, Prasad Joglekar, Neeraj Kumar, Edouard Lesne, Fasil Kidane Dejene, Kai Chang, James Taylor, Bharat Grover, Robin Bläsing, Pranava Keerthi Sivakumar, Elena Derunova, Mazhar Ali, Amir Capua, Hao Yang, Elisa Yang, Avanindra Kumar Pandeya, Alessandro Fumarola, Amilcar Bedoya Pinto, Amine Wahada, Malleswara Rao Tangi, Binoy Krishna Hazra, Souvik Das, Paolo Sessi, Banabir Pal, Anirban Chakraborty, Felix Küster, Kyungjune Cho, Hyeon Han, Ajesh Kollakuzhiyil Gopi, Samiran Choudhury, Kajal Tiwari, and See-Hun Yang.

I also want to thank my collaborators Vivek Kumar, Praveen Vir, Parul Devi, Anastasios Markou, Kaustuv Manna, and Chandra Shekhar from Max Planck Institute for Chemical Physics of Solids, Dresden. They provided high-quality single crystals which made it possible to obtain the nice results presented in this thesis.

I want to especially thank Dirk Sander who helped me to set up the Attocube lab at the beginning of my doctoral period. I am also grateful to Simone Jäger and Antje Paetzold for providing all administrative assistance during my Ph.D. journey. I am especially thankful to Simone who not only helped me at work but also extended her hand to tackle other non-professional matters. I also heartily acknowledge Mike Borrmann, Rene Kunze, Daniel Wagner, Winfried Heichler, Peter Haberland, Andreas Gerstenberger, Pierre-Jean Zermattan, Frank Helbig, Kai-Uwe Aßmann, Claudia Münx, and Norbet Schammelt for technical assistance.

I gratefully acknowledge the financial support provided by Alexander von Humboldt Foundation and Max Planck Society. I especially want to thank my parents and my brother Arpit for their love and continuous support. Last but not least, I would like to thank my Master's supervisor Prof. Dilip G. Kanhere who motivated and guided me to pursue my career in research.

Curriculum Vitae

Name Ankit Kumar Sharma
Birth 28.02.1991 in Sawai Madhopur, India
Gender Male
Nationality Indian

Education

2016-2021 Doctoral Candidate at Martin Luther University of Halle-Wittenberg and
 Max Planck Institute of Microstructure Physics, Halle (Saale), Germany
2013-2014 Post Graduate Diploma in Material Science at Jawaharlal Nehru Center for
 Advanced Scientific Research, India
2011-2013 Master of Science in Physics at Central University of Rajasthan, India.
2008-2011 Bachelor of Science in Physics, Chemistry, and Mathematics at University
 of Kota, India

Academic Experience

2016-2021 Research Assistant, Max Planck Institute of Microstructure Physics,
 Germany
2014-2016 Scientific Assistant in Atomic Physics, Bhabha Atomic Research Center,
 India

Eidesstattliche Erklärung

Ich, Ankit Kumar Sharma, erkläre an Eides statt, dass ich die vorliegende Arbeit “**Probing non-collinear spin textures using variable temperature magnetic force microscopy**” selbstständig und ohne fremde Hilfe verfasst, keine anderen als die von mir angegebenen Quellen und Hilfsmittel benutzt und die den benutzten Werken wörtlich oder inhaltlich entnommenen Stellen als solche kenntlich gemacht habe.

Halle (Saale), den 19.04.2022

Ankit Kumar Sharma